A Conceptual Multilevel Approach to Polyolefin Reaction Engineering

João B. P. Soares, Timothy Mckenna

The Canadian Journal of Chemical Engineering

A Conceptual Multilevel Approach to Polyolefin Reaction Engineering

Journal:	*The Canadian Journal of Chemical Engineering*
Manuscript ID	Draft
Wiley - Manuscript type:	Article
Date Submitted by the Author:	n/a
Complete List of Authors:	Soares, Joao; University of Alberta, Department of Chemical and Materials Engineering McKenna, Timothy; University of Lyon, C2P2-Equipe LCPP
Keywords:	polymer reaction engineering, polyolefins, polypropylene, polyethylene, Mathematical modelling

A Conceptual Multilevel Approach to Polyolefin Reaction Engineering

João B.P. Soares,[1] Timothy F. L. McKenna[2]

[1]Department of Chemical and Materials Engineering, University of Alberta, Edmonton, Alberta, Canada
[2] CP2M UMR 5128, University of Lyon, Villeurbanne, France

Abstract

This article gives a wide overview of different types of mathematical models that can be used to describe the polymerization of linear olefins with coordination catalysts. We expanded the conventional classification of mathematical models into micro-, meso-, and mesoscale, to include seven modeling levels: catalysis, polymerization kinetics, thermodynamic equilibrium, particle transport phenomena, particle interactions, reactor fluid dynamics, and reactor residence time distribution. Some of these levels may coexist at the same scale, but they are better treated separately because they make use of distinct modeling approaches. How complex the models in each level need to be, as well as how many modeling levels should be *implicitly* included, depends on the type of application intended for the simulations. In this paper we will argue that the proposed levels of mathematical modeling not only bring to our attention the complexity behind the simulation of laboratory and industrial scale olefin polymerization reactors, but are also useful conceptual tools to assist us decide which levels to include and which ones to exclude when we develop simulation packages to describe olefin polymerization processes.

1 Introduction

Polyolefins dominate the polymer commodity market in the 21st century. Indeed, you would be hard-pressed to find a sector of modern life that does not use polyolefins. They owe their enormous success to their low cost, wide range of properties, easy recyclability and reusability. They are also made from abundant monomers that have a low environmental footprint. Because only carbon and hydrogen make up the building blocks of polyolefins—ethylene, propylene, a few higher α-olefins, and dienes—they can be burnt cleanly at the end of their useful lives to generate energy with only carbon dioxide and water as by-products. Even though we have been working with polyolefins for over thirty years, we are still impressed by the wide range of products that can be made from these simplest of monomers. Figure 1 illustrates the astonishing range of products that the properly engineered combination of carbon and hydrogen atoms can make.

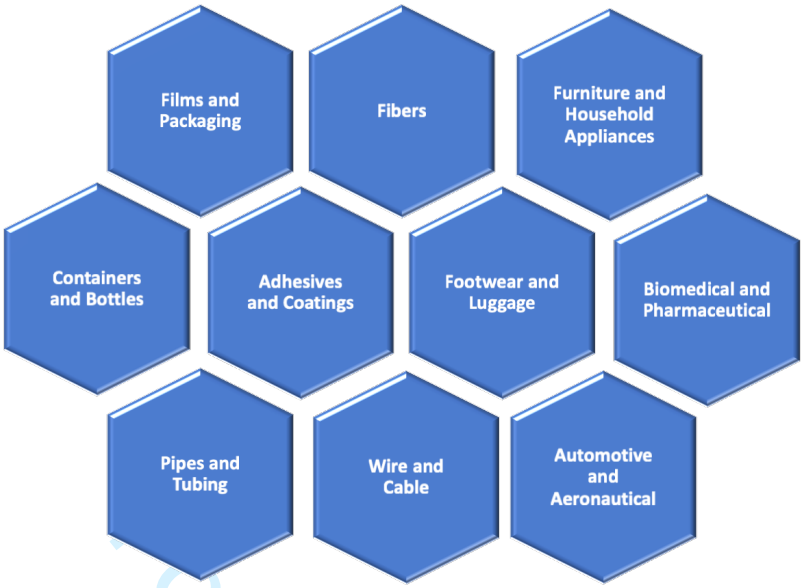

Figure 1 The multiple applications of polyolefins.

The key to their versatility lies on how we can drastically modify the properties of polyolefins by tuning their microstructures. The microstructure of ethylene homopolymers and ethylene/α-olefin copolymers is characterized by the distributions of molecular weight (MWD), chemical composition (CCD), comonomer sequence length (CSLD), and long chain branching (LCB). The CCD can also be called the short chain branching distribution (SCBD), but the latter distribution has a wider scope. The incorporation of an α-olefin in polyolefin chains generates a SCB, but this is not the only way SCBs can be made. They can also be formed by backbiting during the free radical polymerization of ethylene to make low density polyethylene (LDPE), but in this article we will only discuss polyolefins made with coordination catalysts. In this case, CCD and SCBD have identical definitions. The distributions of stereoregularity (SRD) and regioregularity (RRD) must also be considered when analyzing propylene homopolymers, its copolymers with ethylene and, more rarely, higher α-olefins. The complete set of these distributions constitutes what we call the *microstructure* of a polyolefin. Together they define the property space inhabited by the polyolefin. Polyolefin properties may also be affected by processing conditions, aging, use of additives and fillers, etc., but it is the microstructure that determines the boundaries of the properties space. Therefore, the microstructure is the fundamental concern of anyone making a polyolefin.

The mechanical and rheological properties of polyolefins are strongly influenced by their MWD and are often correlated with their average molecular weights: M_n, M_w, M_z and, more rarely, M_{z+1}. Depending on the type of catalyst and process used to make it, the polydispersity index ($PDI = M_w/M_n$) of a polyolefin may vary from 2.0 to values higher than 10. (We are aware that IUPAC recommends the term *dispersity* instead of *polydispersity index*. However, the use of PDI has become so entrenched in polyolefin reaction engineering that we prefer to keep using it. We hope our choice does not upset the most rule-oriented of our readers.)

The LCB frequency and topology also change the rheology of polyolefins, even if they are present in as little as a few LCBs per 10,000 C atoms. More remarkably, the crystallinity and melting points of polyolefins can span from the high values of polyethylene and isotactic

polypropylene to amorphous materials that do not have a melting point at all, simply by copolymerizing ethylene and propylene with each other or with α-olefins. In the case of EPDM terpolymers, copolymerization with dienes adds pendant double bonds to the backbones that can be crosslinked to make rubbers in post-reactor processes.

Therefore, when we make a polyolefin with coordination catalysts or free radical initiators, what we are actually doing is building a microstructure that fits the specifications of our application—whether we realize it or not!—by setting target values for M_w and PDI (or their surrogate values, melt index and melt index ratio), and average copolymer composition (or densities). Since average values alone are not enough to uniquely determine the properties of a polyolefin, a more refined approach is to control the microstructural distributions described above. The difficulty is that several factors, at many scales, interact to determine the averages and shapes of these distributions. Moreover, it is often not possible to control these distributions independently, forcing us to settle for a compromise that fits our product design objectives as close as possible.

Polyolefin manufacturing is best understood if we subdivide it into the interconnected modeling levels depicted in Figure 2. Each of the levels describes specific physical and/or chemical phenomena that require their own unique mathematical models. In this picture, we assumed that the polymerization was promoted by a heterogeneous coordination catalyst. The layers corresponding to Particle Transport Phenomena and Particle Interactions must be excluded for the solution polymerization of olefins with a homogeneous catalyst or a free radical initiator.

The innermost *Catalysis* level defines the type of microstructures that a catalyst can produce. The other levels influence the conditions surrounding the catalyst active sites— local temperature and concentrations of many chemical species—but do not directly define the polyolefin microstructure. If we are allowed to make an analogy, as imperfect as analogies may be, the Catalyst level is equivalent to the genetic code of an organism, while the other levels are akin to the environmental conditions in which the genetic code is expressed. Changing the environment affects how the organism develops, but the range of possibilities for what the organism can become is indelibly fixed in its genetic code.

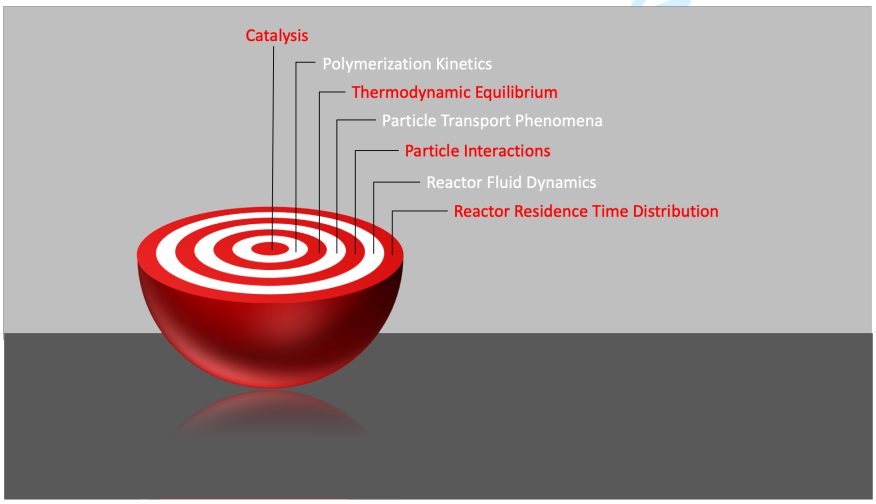

Figure 2 Multiple phenomena taking place at different levels during polymerization affect the yield and properties of polyolefins. A comprehensive polymerization reaction model should account for all of these levels.

The *Polymerization Kinetics* level is nested immediately outside the Catalysis level. Phenomena taking place here defines how fast the catalyst sites activate and deactivate, how quickly the polymer chains grow by the addition of ethylene, propylene, or α-olefins, and how frequently these chains stop growing via transfer reactions. This level is closely linked to the previous one, but time plays a decisive role here, while its absent in the Catalysis level. We will show later that this crucial difference, and its implications on the type of mathematical models it requires, justifies the distinction between these two levels, even though they take place at the same length scale.

The third innermost layer in Figure 2 is the *Thermodynamic Equilibrium* level. In a solution polymerization process with a homogeneous catalyst, it describes the equilibrium between the chemical species in the gas and liquid phases. In a gas-phase process, the equilibrium involves the species in the gas phase in contact with the amorphous polymer phase surrounding the catalyst sites. Finally, in a three-phase slurry polymerization process, these are the equilibria among gas, liquid diluent/monomer, and amorphous polymer phases. Since the thermodynamic equilibria among these phases determines the concentrations at the active sites, they strongly affect the properties of the polymer made by the catalyst.

Moving outward to the next layer, we reach the *Particle Transport Phenomena* level, which applies only to heterogeneous catalysts. Models at this level quantify mass and heat transport phenomena occurring inside the growing polyolefin particles and within the boundary layer surrounding them. This is a classic moving-boundary catalytic reaction and diffusion problem: under appreciable mass transfer limitations, the rate of monomer diffusion from the polymer particle surface to its center cannot compensate for the rate of monomer consumption by polymerization, leading to radial concentration profiles. Therefore, active centers located closer to the particle surface are exposed to higher monomer concentrations than those placed near the particle center. Likewise, if the rate of heat generated by the exothermic polymerization is higher than the rate of heat transfer through the particle, a radial temperature profile will develop, with the highest temperature at the core of the polymer particle. Further resistances in the boundary layer can lead to significant gradients between the particle surface and the bulk phase of the reactor; these gradients may, in fact, be quite significant in gas phase polymerizations. The consequence of these concentration and temperature profiles is that active sites located at different radii in the particle are exposed to varying conditions and make polyolefin chains with distinct microstructures.

Leaving the polymer particles and stepping into the reactor realm, we reach the *Particle Interactions* level—which is also absent in solution polymerizations. At this level, we need to describe how the polymer particles interact among themselves and with the reactor surfaces under the flow fields in the polymerization reactor. Collisions among the particles may cause them to agglomerate with each other or to break apart; collisions with reactor surfaces may lead to adhesion and fouling.

The penultimate layer quantifies the *Reactor Fluid Dynamics* level. We are now placed farther from the polymer particles, describing how macroscopic flow patterns may form concentration and temperature gradients in the continuous phase of the reactor. If the concentrations and temperature throughout the reactor are not uniform, the polymer particles—or isolated active sites in the case of solution polymerization—traveling through different regions in the reactor are exposed to varying conditions and, therefore, make polyolefins with different microstructures.

Finally, the outermost ring is the *Reactor Residence Time Distribution* level. This concept is closely related to the previous level, but its mathematical treatment is different enough (and infinitely simpler) to warrant its classification as a separate level. It accounts for the time each polymer particle (for slurry or gas-phase reactors) or individual active site (for solution reactors) spend in the reactor. When coupled with models at the other scales, it allows us to predict how the microstructure of polyolefins may vary from particle to particle.

In this overview article, we will outline how these seven conceptual mathematical modeling levels can be combined to predict the microstructure and yield of polyolefins made with coordination catalysts. Even though some of these principles apply to free-radical processes for LDPE manufacturing, the differences from coordination polymerization processes are too large to allow for a unified treatment. The scientific literature is awash with publications that examine in depth one or more of these levels, but never in the way we are proposing in this article; we will cite these contributions in the sections below to provide a list of additional readings. However, our intention is to follow the KISS—Keep It Simple Stupid—principle herein. We will start from the most basic models that define the Catalysis level in Figure 2, then gradually navigate to the outer levels, showing how the phenomena in the subsequent levels affect the predictions of the previous ones. We hope this approach will give the reader an appreciation for how these mathematical modeling levels come together to describe a polyolefin without introducing undue complexities in our description. In the process, we will purposedly overlook many minutiae, following the advice of William James: "*The art of being wise is the art of knowing what to overlook*." We hope we have succeeded in our objectives.

2 The Conceptual Multilevel Approach

We will now start navigating through the multilevel approach outlined in Figure 2, starting from the Catalysis level and gradually moving up to the Reactor Residence Time Distribution level. We will keep the details as simple as possible, but we will cite references in which the readers can find in-depth mathematical modeling and simulation studies related to each one of those levels. We will not attempt to perform an extensive literature review in this enormous area of research. Rather will focus on work previously published by our own groups, even though many other groups have outstanding contributions in this area. Our intention herein is to focus on our own personal view on polyolefin reaction engineering.

The case studies you will see below are not the result of detailed simulations: they are illustrations of how to combine different modeling levels to simulate the type of polyolefin that could be made under a set of conditions. To keep things even simpler, we will narrow our examples to homopolymerizations or to binary copolymerizations of ethylene and an α-olefin.

2.1 Catalysis

The instantaneous microstructural distributions of linear polyolefins made with a single-site-type (SS) coordination catalyst can be described with powerful analytical expressions. *Instantaneous* means that these distributions describe polymer populations made within a short time interval, during which the polymerization conditions around the active sites can be considered constant. As the polymerization conditions change, so will the instantaneous distributions. *Cumulative* microstructural distributions, describing the polymer made over a longer period of time, can be

calculated as the sum of several instantaneous distributions weighted by the mass fractions of the polymer populations made in each time interval. This approach works because the lifetime of a polymer chain is much shorter than the time scales associated with the dynamics of industrial polymerization reactors.[1]-[4] However, at the Catalysis level, we are not worried about time. Time does not even appear as a variable in any of the equations we discuss in this section.

The instantaneous MWD can be derived from fundamental polymerization principles by noticing that only two events can occur when a polyolefin chain is made: the *living* chain either grows by the addition of a monomer or comonomer molecule, or stops growing through a chain transfer reaction. This mechanism inexorably produces a polymer population with an instantaneous chain length distribution (CLD) that obeys Flory most probable distribution (MPD).[5],[6] Flory MPD may be expressed as a molar or weight distribution, in linear or log scale. The weight distribution in log scale is the most useful form because it is easier to relate to the MWD measured by gel permeation chromatography (GPC),[7]

$$w_{\log r} = \lambda r^2 \tau^2 \exp(-r\tau) \tag{1}$$

where r is the number of monomer units in a polymer chain, $\lambda = 1/\log e = 2.3026$ is a normalization constant resulting from the $\log_{10}$ transformation, and τ is the ratio between the sum of the frequencies of all chain transfer reactions and the frequency of propagation,

$$\tau = \frac{\sum f_{t_i}}{f_p} \tag{2}$$

The frequencies in Eq. (2) depend on the polymerization mechanism. For most coordination catalysts, the propagation frequency is a linear function of the monomer concentration at the active site, $[M]_s$,

$$f_p = k_p [M]_s \tag{3}$$

where k_p is the propagation rate constant. For copolymers, a similar equation applies, but k_p must be replaced with the *pseudo-kinetic constant*[8]-[10] $\hat{k}_p$ and $[M]_s$ with the total concentration of monomer *and* comonomer at the active site, $[M_T]_s = [M_1]_s + [M_2]_s$. For the present discussion, it suffices to say that the functions that quantify f_p for homopolymerization and copolymerization have the same form, as we will show later in Section 2.2. Kinetic rate constants are used more commonly than frequencies in polyolefin reaction engineering models. We will use frequencies in this article because they allow a more general treatment and are easier to compare among reactions of different orders. Besides, the magnitude of a frequency has an intuitive feel (1 s^{-1} versus 100 s^{-1}), which is lacking in the magnitude of a kinetic rate constant (2 $L \cdot mol^{-1} \cdot s^{-1}$ versus 200 $L \cdot mol^{-1} \cdot s^{-1}$).

The most common chain transfer steps in olefin polymerization are transfer to monomer, transfer to a small molecule (H_2, alkyl cocatalysts, impurities), and β-hydride elimination (sometimes called spontaneous transfer). For most catalysts, these frequencies are given by the equations,

$$f_{t_M} = k_{t_M}[M]_s \tag{4}$$

$$f_{t_X} = k_{t_X}[X]_s \tag{5}$$

$$f_{t_\beta} = k_{t_\beta} \tag{6}$$

where f_{t_M}, f_{t_X} and f_{t_β} are the frequencies of transfer to monomer, transfer to a small molecule, and β-hydride elimination, respectively. Pseudo-kinetic constants must be used for copolymerizations, but the forms of the functions in Eq. (4) to (6) remain the same.[7]

After substituting Eq. (4) to (6) in Eq. (2), we arrive at a more detailed definition for τ,

$$\tau = \frac{k_{t_M}}{k_p} + \frac{k_{t_X}[X]_s + k_{t_\beta}}{k_p[M]_s} \tag{7}$$

Eq. (7) shows that the parameter τ depends on three chain transfer-to-propagation rate constant ratios,

$$\tau = \mathrm{K}_M + \mathrm{K}_X \frac{[X]_s}{[M]_s} + \mathrm{K}_\beta \frac{1}{[M]_s} \tag{8}$$

where $\mathrm{K}_M = k_{t_M}/k_p$, $\mathrm{K}_X = k_{t_X}/k_p$, and $\mathrm{K}_\beta = k_{t_\beta}/k_p$.

Before we illustrate the use of Eq. (1), let's transform the CLD into its equivalent MWD,[7]

$$w_{\log M_r} = \lambda {M_r}^2 \hat{\tau}^2 \exp(-M_r\hat{\tau}) \tag{9}$$

where M_r is the molecular weight of a chain having r monomeric units. The parameter $\hat{\tau}$ is related to τ by the equation,

$$\hat{\tau} = \frac{\tau}{\bar{M}} \tag{10}$$

In Eq. (10), $\bar{M}$ is the average molar mass of the repeating unit in the polymer chains. For a binary copolymer,

$$\bar{M} = \bar{F}_1 M_1 + (1 - \bar{F}_1) M_2 \tag{11}$$

where $\bar{F}_1$ is the average molar fraction of monomer 1 (typically ethylene) in the copolymer, and M_1 and M_2 are the molar masses of monomer 1 and 2, respectively. For an ethylene homopolymer ($\bar{F}_1 = 1$), $\bar{M} = M_1 = 28$ g·mol^{-1}.

It is easy to demonstrate that the molecular weight averages of polymers described by Flory MPD are given by,[7]

$$M_n = \frac{1}{\hat{\tau}} \tag{12}$$

$$M_w = \frac{2}{\hat{\tau}} \tag{13}$$

Consequently, the instantaneous polydispersity of polyolefins made with an SS catalyst (such as a homogeneous metallocene) is $PDI = M_w/M_n = 2$. This is a common criterion used to test whether or not a catalyst displays bona fide SS behavior.

We are now ready to start using Eq. (9) to understand how different polymerization conditions affect the MWD of polyolefins made with an SS catalyst. First, we must know the concentrations of all reagents and temperature surrounding the active sites, which is the realm of the Catalysis level at the core of Figure 2.

The values of the parameters K_M, K_X, and K_β depend only on the temperature for a given catalyst/cocatalyst system. Therefore, at a fixed temperature, the MWD can only be controlled by changing $[M]_s$ or $[X]_s$. Moreover, since the catalyst makes polymer chains that obey Flory MPD, M_n can change, but PDI remains equal to 2. Figure 3 shows how the MWD shifts towards lower averages but retains the same shape as $[X]_s$ increases. Figure 4 shows how M_n for polyethylene made with the same catalyst depends on $[M]_s$ and $[X]_s$. Since the shapes of the MWD are always the same, we only need to know M_n to reconstruct the complete MWD using Eq. (9).

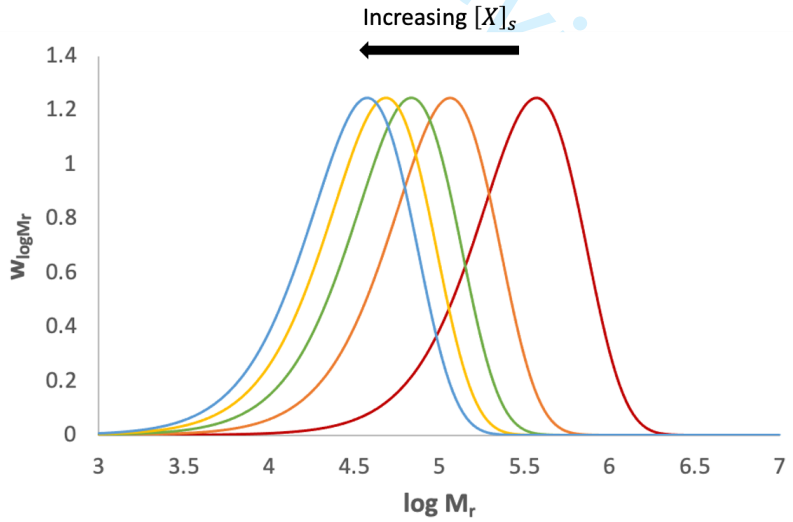

Figure 3 Effect of changing the concentration of chain transfer agent on the MWD of polyethylene made on an SS catalyst. From left to right, $[X]_s = 0, 0.02, 0.04, 0.06, 0.08$ mol·L^{-1} and $M_n = 187, 58, 34, 24, 29$ kg·mol^{-1}. Model parameters: $K_M = 1 \times 10^{-4}$, $K_X = 1 \times 10^{-2}$, $K_\beta/[M]_s = 5 \times 10^{-5}$, $[M]_s = 0.6$ mol·L^{-1}, $\bar{M} = 28$ g·mol^{-1}.

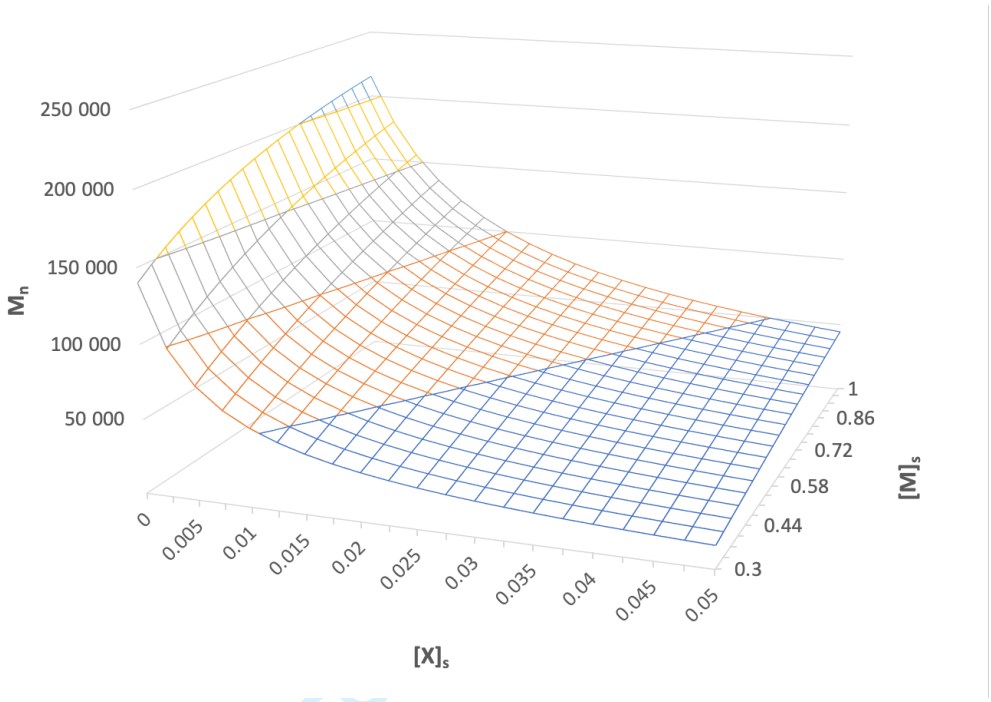

Figure 4 Effect of changing the concentrations of monomer and chain transfer agent on the M_n of polyethylene made with an SS catalyst. Model parameters are listed in the caption of Figure 3.

The MWDs represented in Figure 3 are more exceptions than the rule for commercial polyolefins. Some solution polymerization processes that use homogeneous metallocenes may make polymers with MWDs that approximate Flory MPD, but heterogenized metallocenes in slurry and gas-phase processes will typically make polyolefins with broader MWDs.[11],[12] Moreover, the *PDI* expected for polyolefins made with heterogeneous Ziegler-Natta or Phillips catalysts is much higher than 2. Several factors may contribute to this broadening, potentially including internal and external transport resistances, which we will discuss in Section 2.4. Right now, we will stay away from these complexities and focus only on phenomena taking place at the Catalysis level. If all other effects we encounter moving outward in Figure 2 are excluded, the only explanation for instantaneous MWDs that are wider than Flory MPD is the presence of more than one *type* of active site on the catalyst. Today most olefin catalysis experts agree that two or more site types exist in heterogeneous Ziegler-Natta and Phillips catalysts. They are, consequently, classified as multiple-site-type (MS) catalysts. Unfortunately, this is as far as the consensus goes. Nobody is sure how many site types there are, how they differ, and how we can control their creation precisely.

Luckily, from the point of view of polyolefin reaction engineering, it does not matter what these sites may be. We only need to determine the *minimum* number of site types needed to describe the MWD of a polyolefin made with an MS catalyst. This can be done via MWD deconvolution, a method that has been widely used for a couple of decades.[7],[13]-[15] We will explain how this concept can be used to describe the MWD of polymers made with an MS catalyst, such Ziegler-Natta, Phillips, and even some supported metallocenes.

The MWD of a polyolefin made with an MS catalyst with n site types is modeled as,

$$W_{\log M_r} = \sum_{i=1}^{n} m_i w_{\log M_r,i} = \lambda {M_r}^2 \sum_{i=1}^{n} m_i {\hat{\tau}_i}^2 \exp(-M_r \hat{\tau}_i) \tag{14}$$

where m_i is the mass fraction of polymer made in site type i and $\hat{\tau}_i$ is defined in Eq. (8) and (10) using the ratios K_{M_i}, K_{X_i}, and K_{β_i}. However, these parameters now assume different values for each site type. Molecular weight averages for the whole polymer are obtained from the mass fractions and molecular weight averages of polymer populations made on each site type,[7]

$$\bar{M}_n = 1 \Big/ \sum_{i=1}^{n} \frac{m_i}{M_{n_i}} \tag{15}$$

$$\bar{M}_w = \sum_{i=1}^{n} m_i M_{w_i} \tag{16}$$

Figure 5 shows the MWD of a polyethylene made with a 5-site-type catalyst having the kinetic parameters listed in Table 1. Seen under this lens, a polyolefin made with an MS catalyst is nothing but a blend of polyolefins made in several SS catalysts that behave independently of each other. Is this an oversimplification? Perhaps. One may even argue that it is likely so. But from a modeling point of view it is an extremely useful simplification that allows us to describe complex microstructures with as few parameters as possible.

Figure 5 shows that the MWD for the whole polymer, with $\overline{PDI} = 4.1$—a typical value for Ziegler-Natta resins—is much broader than those of its components. Since each active site type may respond differently to the chain transfer agent (distinct K_X values), changing $[X]_s$ may change not only M_n but also $\overline{PDI}$. For instance, when $[X]_s = 0$ this catalyst would make a polymer with a narrower MWD and $\overline{PDI} = 3.6$.

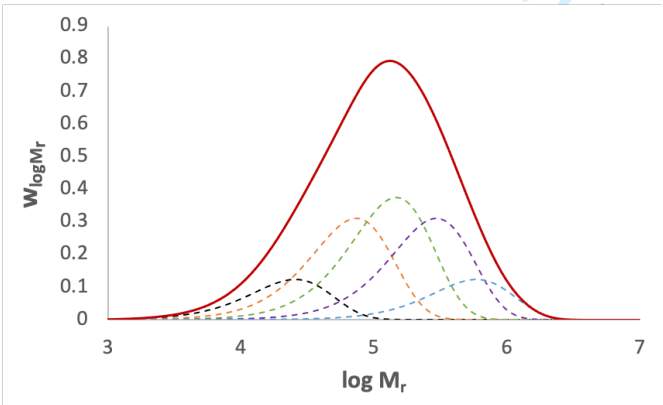

Figure 5 MWD of polyethylene made with an MS catalyst with 5 site types. Polymerization conditions: $[M]_s = 0.6$ mol·L^{-1}, $[X]_s = 0.04$ mol·L^{-1}, $\bar{M} = 28$ g·mol^{-1}. Other model parameters are listed in Table 1. Average molecular weights for polymer made on each site type are: $M_{n_1} = 12\,824$, $M_{n_2} = 36\,923$, $M_{n_3} = 73\,846$, $M_{n_4} = 147\,692$, $M_{n_5} = 295\,385$. The PDI of each MWD distribution is 2. For the whole polymer, $\bar{M}_n = 48\,398$, $\bar{M}_w = 198\,257$, $\overline{PDI} = 4.1$.

Table 1 MS catalyst kinetic parameters for simulations in Figure 5.

	Site 1	Site 2	Site 3	Site 4	Site 5
$\boldsymbol{m}$	0.1	0.25	0.3	0.25	0.1
$\mathbf{K_M}$	1×10^{-4}	5×10^{-5}	2.5×10^{-5}	1.25×10^{-5}	6.25×10^{-6}
$\mathbf{K_X}$	0.03	0.01	0.005	0.0025	0.00125
$\mathbf{K_\beta}$ (mol·L^{-1})	5×10^{-5}	2.5×10^{-5}	1.25×10^{-5}	6.25×10^{-6}	3.13×10^{-6}

This modeling approach uses the *minimum* number of site types—or, equivalently, the minimum number of Flory MPDs—to describe the MWD of a broader and more complex polyolefin. We cannot rule out the existence of more site types. Alternative models have been proposed to account for a continuous distribution of site types, which indeed implies an infinite number of site types.[16] The method illustrated in Figure 5 requires less effort and is based on a fundamental and widely accepted mechanism for the polymerization of olefins with coordination catalysts. Could we describe the MWD with fewer site types? Maybe. It depends on what other factors may affect the formation of the polymer chains. If we can rule out many of the higher level effects shown in Figure 2—and any MWD broadening artifacts during GPC analysis—we can answer this question with a confident *no*. If other factors play a role we may have to change our answer to *yes*, but we need to wait until we start discussing phenomena taking place in the outer layers of Figure 2 to explain why.

The CCD is another essential microstructural distribution of polyolefins. Stockmayer derived the instantaneous bivariate distribution for molecular weight and chemical composition (comonomer fraction) that can be used to describe the joint MWD-CCD of linear binary olefin copolymers made with an SS catalyst.[17] In addition to the assumptions made by Flory to arrive at the MPD, Stockmayer assumed that monomer type 1 or 2 could be added to growing polymer chains following the conditional propagation probabilities $P_{p_{11}} = 1 - P_{p_{12}}$ and $P_{p_{22}} = 1 - P_{p_{21}}$, where $P_{p_{ij}}$ is the probability of adding monomer *j* to a chain terminated in monomer *i*—if you are puzzled by this statement, skip ahead to Eq. (31) to (34) to find how these probabilities are related to propagation rate constants and frequencies. He also assumed that the molar masses of monomer 1 and 2 were the same, but this simplification hardly affects the predictions for polyolefins of commercial interest.[18]

The weight-basis Stockmayer bivariate distribution (BD) in log scale is given by the elegant equation,[7]

$$w_{\log M_r, F_1} = \lambda {M_r}^2 \hat{\tau}^2 \exp(-M_r \hat{\tau}) \sqrt{\frac{M_r}{2\pi\beta\bar{M}}} \exp\left[-\frac{M_r (F_1 - \bar{F}_1)^2}{2\beta\bar{M}}\right] \tag{17}$$

where, F_1 is the molar fraction of monomer 1 in a copolymer chain and $\bar{F}_1$ is the *average* fraction of monomer 1 in the *copolymer population*. It is worth clarifying how the definitions of these two variables differ: F_1 is the chemical composition of *a* copolymer chain in the population (like M_r is the molecular weight of *a* chain with r monomer and comonomer units), while $\bar{F}_1$ is the instantaneous *average* fraction of monomer 1 in the entire copolymer population (like M_n is the average molecular weight of the copolymer population).

The parameter β is defined as,

$$\beta = \bar{F}_1(1-\bar{F}_1)\sqrt{1-4\bar{F}_1(1-\bar{F}_1)(1-r_1r_2)} \quad (18)$$

where r_1 and r_2 are the reactivity ratios for monomer 1 and 2, respectively.[#]

The Mayo-Lewis equation can be used to calculate $\bar{F}_1$,

$$\bar{F}_1 = \frac{(r_1-1){f_1}^2 + f_1}{(r_1+r_2-2){f_1}^2 + 2(1-r_2)f_1 + r_2} \quad (19)$$

if we know the reactivity ratios, r_1 and r_2, and the molar fractions of comonomer 1 and 2, f_1 and $f_2 = 1 - f_1$, *at the active sites*,

$$f_1 = \frac{[M_1]_s}{[M_1]_s + [M_2]_s} = \frac{1}{1 + [M_2]_s/[M_1]_s} = \frac{1}{1+\rho_{21}} \quad (20)$$

$$f_2 = \frac{[M_2]_s}{[M_1]_s + [M_2]_s} = \frac{1}{1+\rho_{12}} \quad (21)$$

Note that we must know the molar fractions of comonomers 1 and 2 at the active sites to calculate $\bar{F}_1$, as we must also know the conditions around the sites to calculate the value of $\hat{\tau}$. Since the phenomena taking place at higher scales in Figure 2 affect these values, they will also affect the MWD and CCD of polyolefins.

Comparing Eq. (9) and (17), it is easy to conclude that Stockmayer BD is an extension of Flory MPD. While Flory MPD had a single parameter $\hat{\tau}$, Stockmayer's relies on two, $\hat{\tau}$ and β, to describe the bivariate MWD-CCD. Indeed, if we integrate Eq. (17) over the entire composition range, we arrive at Eq. (9).[7]

Let's learn what Stockmayer BD can teach us. In Figure 6, we simultaneously increased the fraction of ethylene, f_1, and the concentration of chain transfer agent at the active sites to find out how they affect the MWD-CCD of an ethylene/α-olefin copolymer. As f_1 decreases, the CCD moves to lower fractions of ethylene in the copolymer, $\bar{F}_1$, as predicted by the Mayo-Lewis equation. As the concentration of chain transfer agent increases, the copolymer MWD moves towards lower molecular weight averages. More interestingly, while the breadth of the MWD component remains the same for all copolymers ($PDI = 2$), the breadth of the CCD widens as $\bar{F}_1$ (down to $\bar{F}_1 = 0.5$) and M_n decreases, due to the statistical nature of polymerization.

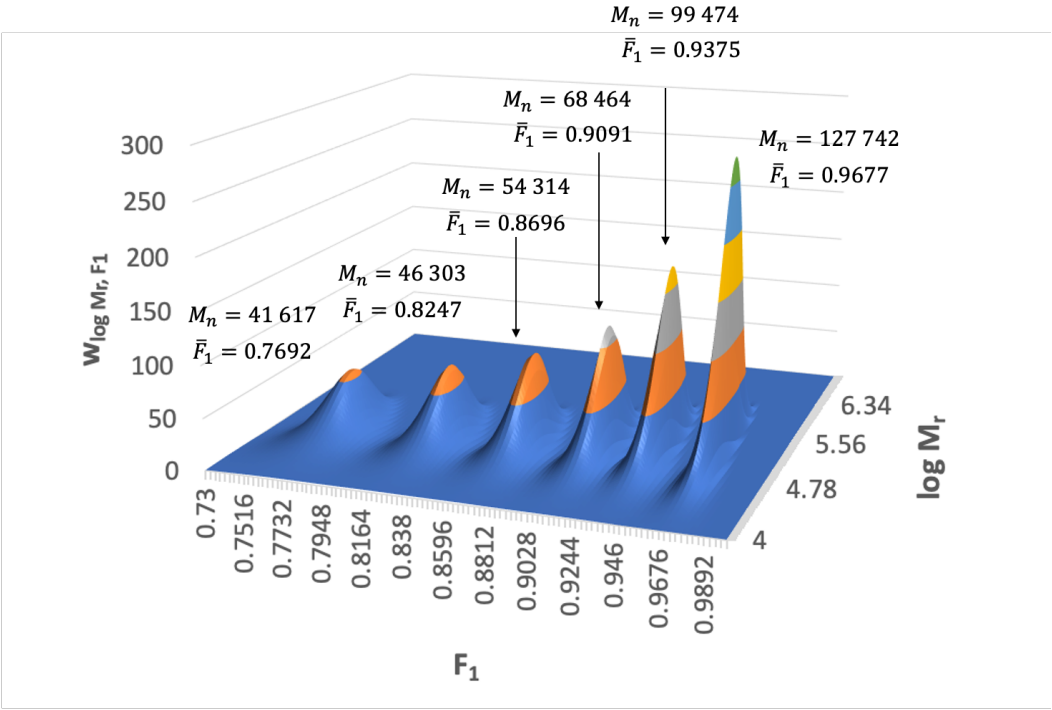

Figure 6 Effect of changing the concentration of chain transfer agent and fraction of comonomer 1 on the MWD-CCD of an ethylene/1-hexene copolymer made with an SS catalyst. From right to left: $[X]_s$ = 0.005, 0.01, 0.02, 0.03, 0.04, 0.05 mol·L^{-1} and f_1 = 0.75, 0.6, 0.5, 0.4, 0,32, 0.25. Model parameters: $K_M = 1 \times 10^{-4}$, $K_X = 1 \times 10^{-2}$, $K_\beta/[M]_s = 5 \times 10^{-5}$, $[M]_s$ = 0.6 mol·L^{-1}, M_1 = 28 g·mol^{-1} (ethylene), M_2 = 84 g·mol^{-1} (1-hexene), $r_1 = 10$ and $r_2 = 0.1$.

The MWD-CCDs shown in Figure 6 describe the instantaneous properties of a linear copolymer made with an SS catalyst. For an MS catalyst, we can repeat the approach used above for MWD and assume that the MWD-CCD of the entire polymer is a weighted superposition of several Stockmayer BDs, [7][19]-[23]

$$W_{\log M_r, F_1} = \sum_{i=1}^{n} m_i w_{\log M_r, F_1, i} = \lambda {M_r}^2 \sum_{i=1}^{n} {\hat{\tau}_i}^2 \exp(-M_r \hat{\tau}_i) \sqrt{\frac{M_r}{2\pi\beta_i \bar{M}_i}} \exp\left[-\frac{M_r \left(F_1 - \bar{F}_{1_i}\right)^2}{2\beta_i \bar{M}_i}\right] \quad (22)$$

where the subscript i identifies the different site types in the catalyst. The parameter β_i and the average comonomer fractions in the copolymer, $\bar{F}_{1_i}$, are calculated with Eq. (18) and (19), respectively, using the reactivity ratios for each site type, r_{1_i} and r_{2_i}. The average molecular weights for the whole polymer are calculated with Eq. (15) and (16), and the molar fraction of monomer 1 in the whole copolymer is calculated as the weighted average of the copolymer compositions made on each site type,

$$\bar{\bar{F}}_1 = \sum_{i=1}^{n} m_i \bar{F}_{1_i} \tag{23}$$

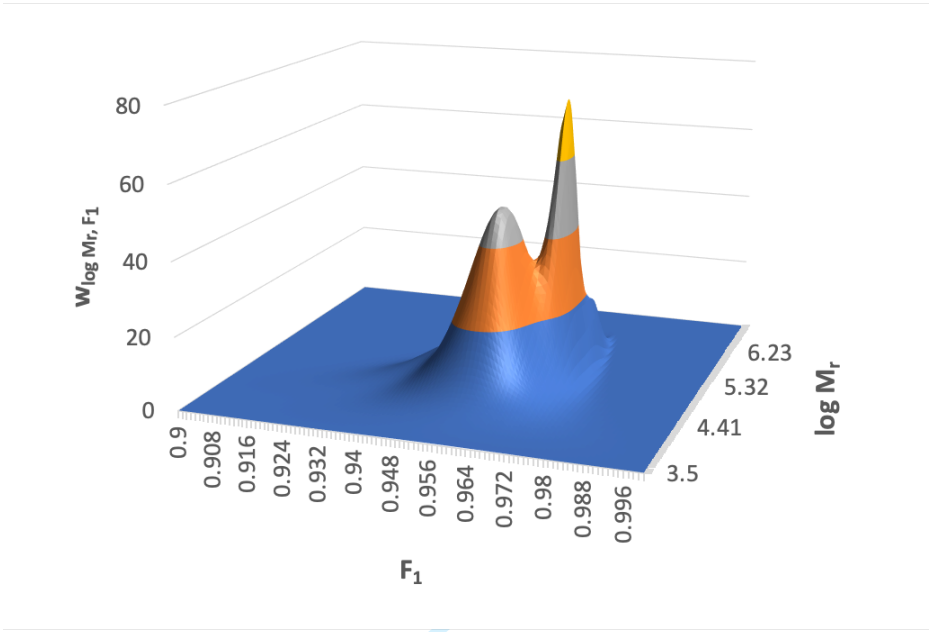

Figure 7 Bivariate MWD-CCD of an ethylene/1-hexene copolymer made with an MS catalyst having 5 site types. Polymerization conditions: $f_1 = 0.75$, $[M_T]_s = [M_1]_s + [M_2]_s = 0.6$ mol·L^{-1}, $[X]_s = 0.04$ mol·L^{-1}. Other model parameters are listed in Table 2. For the whole polymer, $\bar{M}_n = 28\,973$, $\bar{M}_w = 116\,778$, $\overline{PDI} = 4.03$, $\bar{\bar{F}}_1 = 0.96$.

Figure 7 shows how the bivariate MWD-CCD of an ethylene/1-hexene copolymer made with an MS catalyst would look like, using the parameters listed in Table 2. The familiar bimodal composition profile we associate with Ziegler-Natta LLDPE resins is apparent from this simulation. This figure illustrates how powerful this approach really is: from a set of parameters related to the minimum number of site types on the catalyst, we can reconstruct the whole MWD-CCD of a complex polyolefin.

Deconvolution methods have also been proposed to extract the values of these parameters from GPC and chemical composition distribution analyses (CEF, TREF, CRYSTAF, or HT-TGIC),[24]-[26] but this is a substantially more complex problem than the MWD deconvolution procedure mentioned above.

Table 2 MS catalyst kinetic parameters for simulations in Figure 7.

	Site 1	Site 2	Site 3	Site 4	Site 5
$\boldsymbol{m}$	0.15	0.25	0.25	0.3	0.05
$\mathbf{K_M}$	1×10^{-4}	5×10^{-5}	2.5×10^{-5}	1.25×10^{-5}	1×10^{-5}
$\mathbf{K_X}$	0.04	0.02	0.01	0.0025	0.001
$\mathbf{K_\beta}$ (mol·L^{-1})	5×10^{-5}	2.5×10^{-5}	1.25×10^{-5}	6.25×10^{-6}	5×10^{-5}
$\boldsymbol{r_1}$	6	7.2	8	10	11.5
$\boldsymbol{r_2}$	0.167	0.139	0.125	0.1	0.067

The CCD component of the Stockmayer BD can be found by integrating it over the range of all possible molecular weights,[7]

$$w_{F_1} = \int_0^\infty w_{\log M_r, F_1} \mathrm{d}\log M_r = \frac{3}{4\sqrt{2\beta \bar{M} \hat{\tau}}} \left[1 + \frac{(F_1 - \bar{F}_1)^2}{2\beta \bar{M} \hat{\tau}}\right]^{-5/2} \tag{24}$$

Eq. (24) is simply the projection, on the $w_{\log M_r, F_1} \times F_1$ plane, of the MWD-CCD shown in Figures 6 and 7. Figure 8 illustrates the use of Eq. (24). The shapes of these distributions are similar to those measured with CEF and similar CCD analytical methods, making the basis for CCD deconvolution methods.

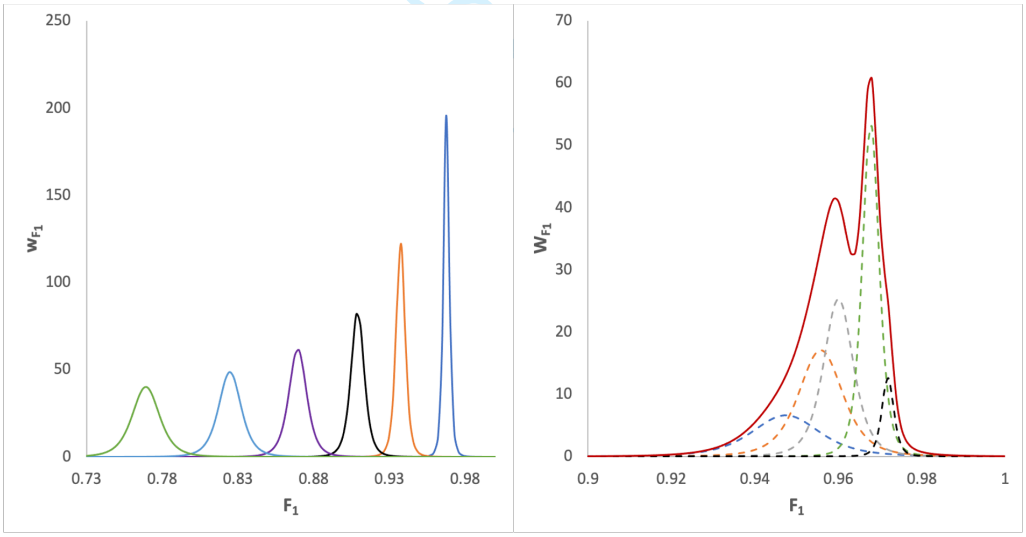

Figure 8 CCD components of the Stockmayer BDs shown in Figure 6 and 7.

The CCD, as quantified with Stockmayer BD, is an *intermolecular* distribution: it measures how the molar fraction of monomer or comonomer vary from chain to chain in a polymer population. The CSLD is another relevant composition distribution for olefin copolymers. Differently from the CCD, the CSLD is an *intramolecular* distribution: it measures the distribution of comonomer sequences *within* the copolymer chains.[27]-[29] We will illustrate its use for the triad distribution of a binary copolymer. Six combinations are possible in this case: $M_1M_1M_1, M_1M_1M_2, M_2M_1M_2, M_1M_2M_1, M_2M_2M_1$, and $M_2M_2M_2$. The triad distribution can be calculated with the same conditional propagation probabilities associated with the Stockmayer BD with the equations,

$$\bar{F}_{111} = \bar{F}_1 {P_{p}}_{11}^{\,2} \tag{25}$$

$$\bar{F}_{112} = \bar{F}_1 {P_{p}}_{11} {P_{p}}_{12} + \bar{F}_2 {P_{p}}_{21} {P_{p}}_{11} \tag{26}$$

$$\bar{F}_{212} = \bar{F}_2 {P_{p}}_{21} {P_{p}}_{12} \tag{27}$$

$$\bar{F}_{121} = \bar{F}_1 {P_{p}}_{12} {P_{p}}_{21} \tag{28}$$

$$\bar{F}_{221} = \bar{F}_2 {P_{p}}_{22} {P_{p}}_{21} + \bar{F}_1 {P_{p}}_{12} {P_{p}}_{22} \tag{29}$$

$$\bar{F}_{222} = \bar{F}_2 {P_{p}}_{22}^{\,2} \tag{30}$$

where $\bar{F}_{ijk}$ is the molar fraction of the triad with comonomer sequence ijk ($i, j, k = 1$ or 2), and $\bar{F}_1$ is the molar fraction of monomer 1 in the copolymer, given by the Mayo-Lewis equation. Expressions for other *n*-ads can be derived following the same rationale.

The conditional propagation probabilities are given by ratios of propagation frequencies,

$$P_{p_{12}} = \frac{f_{p_{12}}}{f_{p_{12}} + f_{p_{11}}} = \frac{k_{p_{12}}[M_2]}{k_{p_{12}}[M_2] + k_{p_{11}}[M_1]} = \frac{1}{1 + r_1 f_1/f_2} = \frac{1}{1 + r_1 \rho_{12}} \tag{31}$$

$$P_{p_{11}} = 1 - P_{p_{12}} \tag{32}$$

$$P_{p_{21}} = \frac{f_{p_{21}}}{f_{p_{21}} + f_{p_{22}}} = \frac{k_{p_{21}}[M_1]}{k_{p_{21}}[M_1] + k_{p_{22}}[M_2]} = \frac{1}{1 + r_2 f_2/f_1} = \frac{1}{1 + r_2 \rho_{21}} \tag{33}$$

$$P_{p_{22}} = 1 - P_{p_{21}} \tag{34}$$

Figure 9 shows how the triad distribution depends on the molar fraction of monomer 1 at the active site for an SS catalyst with $r_1 = 10$ and $r_2 = 0.1$. The triad distribution depends only on the values of r_1 and r_2, which depend only on catalyst type, (weakly) on temperature, and on the ratio of the two monomers at the active sites, ρ_{ij}. If this ratio changes due to phenomena happening at other reactor levels, so will the CSLD.

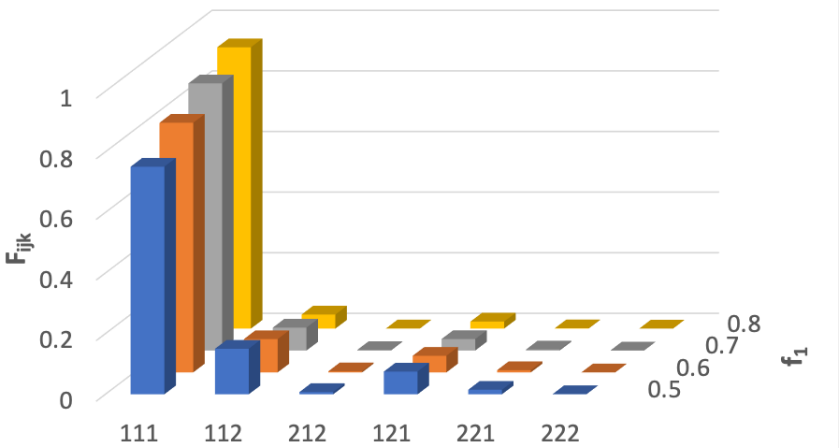

Figure 9 Effect of fraction of monomer 1 on the triad distribution of a binary copolymer made with an SS catalyst with $r_1 = 10$ and $r_2 = 0.1$.

These equations can be extended to describe the triad distribution of a copolymer made with an MS catalyst following the usual weighted superposition approach,

$$\bar{\bar{F}}_{ijk} = \sum_{i=1}^{n} m_i \bar{F}_{1_{ijk}} \tag{35}$$

Figure 10 illustrates the instantaneous triad distribution for an olefin copolymer made with a hypothetical 5-site-type catalyst. The CSLD for the whole polymer (shown in red) is a weighted average of the different triad distributions for copolymer populations made on each site type. A deconvolution method combining MWD and ^{13}C NMR triad and tetrad deconvolution has been proposed to identify the minimum number of site types on MS catalysts following this modeling approach.[27]-[29]

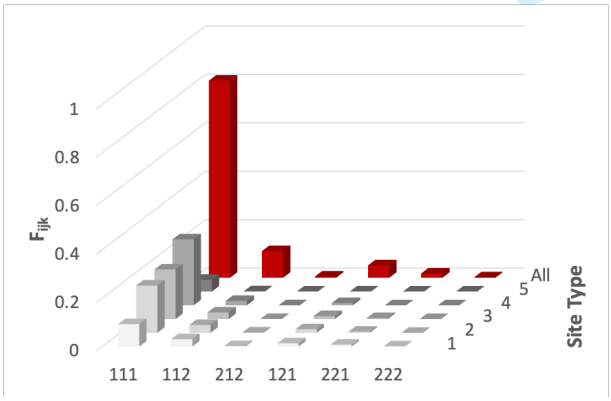

Figure 10 Triad distribution for a copolymer made with an MS catalyst when $f_1 = 0.75$. The triad distributions in grey are for polymer made by each site type; the distribution in red is for the whole polymer made with the MS catalyst. Model parameters: 1) $m_1 = 0.15, r_{1_1} = 2, r_{2_1} = 0.9$, 2) $m_2 = 0.25, r_{1_2} = 4, r_{2_2} = 0.5$, 3) $m_3 = 0.25, r_{1_3} = 5, r_{2_3} = 0.5$, 4) $m_4 = 0.3, r_{1_4} = 10, r_{2_4} = 0.01$, 5) $m_5 = 0.05, r_{1_5} = 30, r_{2_5} = 0.001$.

Except for EPDM rubbers, olefin terpolymers are relatively rare and mostly used in specialty applications such as propylene/ethylene/α-olefin adhesives. The MWD of these polymers can still be described with Flory MPD, but Stockmayer BD does not apply to their joint MWD-CCD. An expression for the instantaneous CCD of linear olefin terpolymers has been developed,[30] but it can only be used for the special case when the frequencies of propagation for the three comonomers do not depend on the type of comonomer attached to the end of the polymer chain (Bernoullian Model). No analytical solutions exist for the CCD of terpolymers that follow the more generic case, when the propagation frequencies depend on the types of comonomers added to the chain *and* last added to the chain (Terminal or Markov Order 1 Model). In this case, population balances or Monte Carlo methods must be used.[7] The CSLD of terpolymers, on the other hand, can be calculated with expressions like the ones we showed above for binary copolymers.

The SD and RD are essential to quantify the crystallinity and melting distributions of polypropylene. Both are intramolecular distributions, like the CSLD. The SD is modelled using probabilities for meso (*m*, isotactic placement) or racemic (*r*, syndiotactic placement) insertions. The triad distribution, for instance, contains three distinct sequences: *mm*, *mr*, and *rr*. Similarly, the RD is modelled as 1-2 or 2-1 insertion sequences: $m_{1\text{-}2}$, $m_{2\text{-}1}$, $r_{1\text{-}2}$, and $r_{2\text{-}1}$.[31] From the set of probabilities for each insertion mode, we can build expressions for *n*-ads that are like the ones shown in Eq. (25) to (30). These equations describe SS catalysts; for MS catalysts, we need to use the weighted sum of the *n*-ads, as we did in Eq. (35) for the CSLD. Since these distributions do not introduce new concepts relevant to the objectives of this article, we will not discuss them any further.

Terminal branching is the most likely mechanism for the formation of LCB in SS or MS catalysts.[32] This mechanism requires a catalyst than can polymerize *macromonomers*—dead chains with terminal vinyl groups—with ethylene, propylene, and α-olefins. When a macromonomer is inserted in a growing polymer chain, its long pendant side chain forms an LCB. Macromonomers may be made *in situ* during the polymerization of ethylene and α-olefins by transfer to ethylene or β-hydride elimination of living chains terminated with an ethylene unit. If a chain terminated with an α-olefin unit undergoes either of these transfer steps, the resulting dead chain would be terminated with a vinylidene group, which is not reactive enough to allow for its reincorporation. LCBs can also be formed during propylene polymerization, provided that the chains undergo methyl elimination to make polypropylene macromonomers with terminal vinyl groups. The frequencies of macromonomer incorporation, β-hydride elimination, methyl elimination, and transfer to ethylene depend strongly on the type of catalyst and, to a lesser extent, on temperature. Selecting the right catalyst, therefore, is essential to maximize LCB formation.

An instantaneous trivariate distribution (molecular weight, chemical composition, and LCB) has been derived for polymers made with SS catalysts.[33]-[35] The same equation applies to MS catalysts if we assume that macromonomers made in one site type are not incorporated by sites of different types. If this hypothesis is wrong, then the polymer microstructure can only be modelled using numerical or stochastic methods.[36]-[40] Despite the importance of LCB on the properties of some commercial polyethylenes, including it in our discussion would make this article excessively long.

In this section we focused on using instantaneous distributions to describe the microstructure of polyolefins. This is not the only mathematical modeling method suited to this task. Population balances and the method of moments have been used more extensively than instantaneous

distributions to describe the MWD and CCD of polyolefins.[41]-[43] Monte Carlo methods are also becoming increasingly more popular.[44] However, whenever possible, we would rather use instantaneous distributions because they provide a wealth of microstructural information packaged in simple analytical expressions. Moreover, they do not depend on time and can be decoupled from some of the time-depended phenomena we will describe in the other modeling levels below.

2.2 Polymerization Kinetics

Polymerization kinetics is linked to the type of catalyst and cocatalyst used to make polyolefins. One could argue, perhaps convincingly, that the Catalysis and Polymerization Kinetics levels should be merged. However, we prefer to decouple them because time plays no role on the Catalysis level, but it becomes the protagonist in the Polymerization Kinetics level. We admit that this is our personal choice, but we will prove its an elegant one herein.

The simplest model for homopolymerization kinetics with an SS catalyst requires only three elementary steps: site activation, monomer propagation, and site deactivation,[7]

$$C + Al \overset{k_a}{\rightarrow} P_0 \tag{36}$$

$$P_r + M \overset{k_p}{\rightarrow} P_{r+1} \tag{37}$$

$$P_r \overset{k_d}{\rightarrow} C_d + D_r \tag{38}$$

where C is a catalyst precursor site, Al is a cocatalyst molecule, M is a monomer molecule, C_d is a deactivated site, P_r is a living polymer chain of length r, and D_r is a dead polymer chain of length r. We did not include transfer steps because they do not directly affect the rate of monomer propagation. However, they may with some catalysts, especially when hydrogen is used as a chain transfer agent. We will return to this case later in this section.

Using Eq. (36) to (38), we can derive an equation for the rate of homopolymerization,[7]

$$R_p = f_p \frac{1 - \exp[-f_a(1 - f_d/f_a)t]}{1 - f_d/f_a}[C_0]\exp(-f_d t) \tag{39}$$

where the propagation frequency is defined in Eq. (3) and the site activation and deactivation frequencies are given by,

$$f_a = k_a[Al]_s \tag{40}$$

$$f_d = k_d \tag{41}$$

The model described in Eq. (39) is simple—some may dismiss it as being simplistic—but it can describe (sometimes with small modifications) the homo- and copolymerization rates of

olefins with many SS and MS catalysts.[11],[12],[45]-[54] Figure 11 illustrates how changing f_p, f_a, and f_d affect the polymerization rates predicted with Eq. (39). The propagation frequency fixes how high R_p may reach, f_a how long it takes to get to the maximum value of R_p, and f_d how quickly R_p drops from its maximum value. This model excels because of its clarity and grace; even though deviations from this behavior do occur, it can still capture the polymerization kinetics with most SS and MS catalysts.

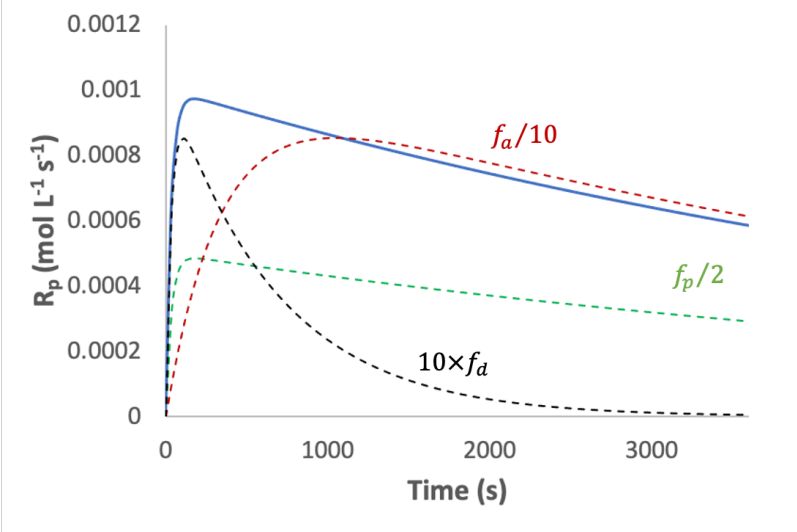

Figure 11 Rate of polymerizations predicted with Eq. (39). Parameters for the base-case catalyst (solid blue line): $f_p = 1 \times 10^5$ s^{-1}, $f_a = 3 \times 10^{-2}$ s^{-1}, $f_d = 1.5 \times 10^{-4}$ s^{-1}, $[C_0] = 1 \times 10^{-8}$ mol·L^{-1}.

We can integrate Eq. (39) from $t = 0$ to $t = t_p$ to find how much polymer is made during the polymerization,

$$Y_p = \bar{M} V_R \int_0^{t_p} R_p \mathrm{d}t = \frac{f_p}{1 - f_d/f_a} \left[\frac{1 - \exp(-f_d t_p)}{f_d} - \frac{1 - \exp(-f_a t_p)}{f_a} \right] \bar{M} [C_0] V_R \qquad (42)$$

where V_R is the volume of the reaction medium.

Figure 12 shows how the polymer yield varies with time for the same cases studied in Figure 11. The fast-deactivating catalyst (dotted black curve) is inadequate for reactors with long residence times, while the yield of the slow-activating catalyst (dotted red curve) lags behind of its faster-activating counterpart (solid blue line).

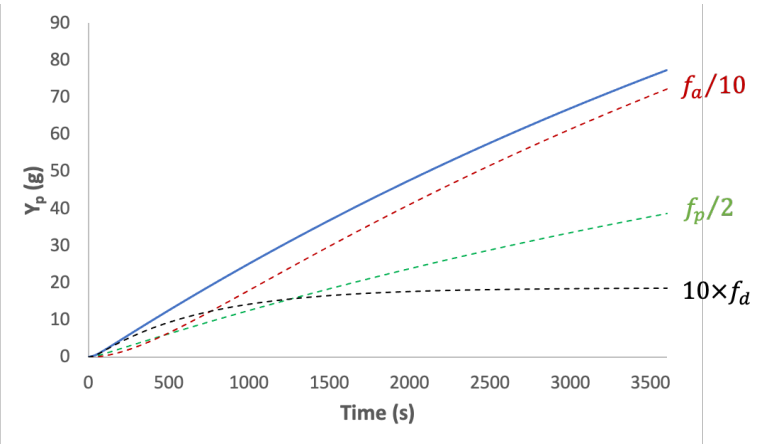

Figure 12 Polymer yield predicted with Eq. (42). Parameters for base-case catalyst (solid blue line): $f_p = 1 \times 10^5$ s^{-1}, $f_a = 3 \times 10^{-2}$ s^{-1}, $f_d = 1.5 \times 10^{-4}$ s^{-1}, $[C_0] = 1 \times 10^{-8}$ mol·L^{-1}, $V_R = 1$ L, $\bar{M} = 28$ (polyethylene).

If we want to connect this homopolymerization kinetics model with the previous Catalysis level, we must ask the question: Do SS catalysts with different f_p, f_a, and f_d, like the ones studied in Figures 11 and 12, produce homopolymers with different MWDs, *assuming they have the same ratios of transfer-to-propagation frequencies*? The answer is no. If these catalysts have the same values for τ, then all of them will make polymers with identical MWDs. The base-case catalyst (blue solid line) will have the highest yield for $t_p = 3600$ s while the fast-deactivating catalyst (dotted black line) will have the lowest, but if their τ values are the same, they will make polymer with undistinguishable MWDs at *any* polymerization time. The MWD—and other microstructural distributions—for polymers made with SS catalysts does not depend on time, *assuming that the active sites are exposed to the same conditions throughout the polymerization*. We will see later that this is easier said than done, but we will assume it to be true for now.

How can we extend this model to MS catalysts? You probably guessed it right. We just add the polymerization kinetics models for each site type,

$$R_{p_T} = \sum_{i=1}^{n} R_{p_i} = [C_0]_T \sum_{i=1}^{n} x_{i_0} f_{p_i} \frac{1 - \exp\left[-f_{a_i}\left(1 - f_{d_i}/f_{a_i}\right)t\right]}{1 - f_{d_i}/f_{a_i}} \exp\left(-f_{d_i} t\right) \tag{43}$$

where $[C_0]_T$ is the total concentration of active sites, and x_{i_0} is the molar fraction of sites of type i at $t = 0$. The subscript i indicates that the frequencies for site activation, propagation, and site deactivation vary among different site types. It is notoriously difficult to estimate x_i, f_{p_i}, f_{a_i}, and f_{d_i} for each site type of an MS catalyst, but some methods for this estimation have been proposed in the literature.[48],[55] A similar equation could be derived for the polymer yield of each site type and for the whole catalyst, as a sum of Eq. (42) for each site type.

Let's illustrate some of the consequences of working with an MS catalyst in which the sites types follow different polymerization kinetics curves. We will keep this example as simple as possible: an MS catalyst with only two site types. It is easy to visualize this system by imagining it consists of two metallocenes co-supported on SiO_2 particles. (The same principles apply to multisite heterogeneous Ziegler-Natta and Phillips catalysts.) Figure 13 shows the rates of polymerization for the model dual-site catalyst. Site 1 activates more slowly, but is more stable

than site 2, which activates quickly, but also deactivates faster than site 1. Consequently, the mass fraction of polymer made on site 1, m_1, increases throughout the polymerization,

$$m_1 = \frac{Y_{p_1}}{Y_{p_1} + Y_{p_2}} \tag{44}$$

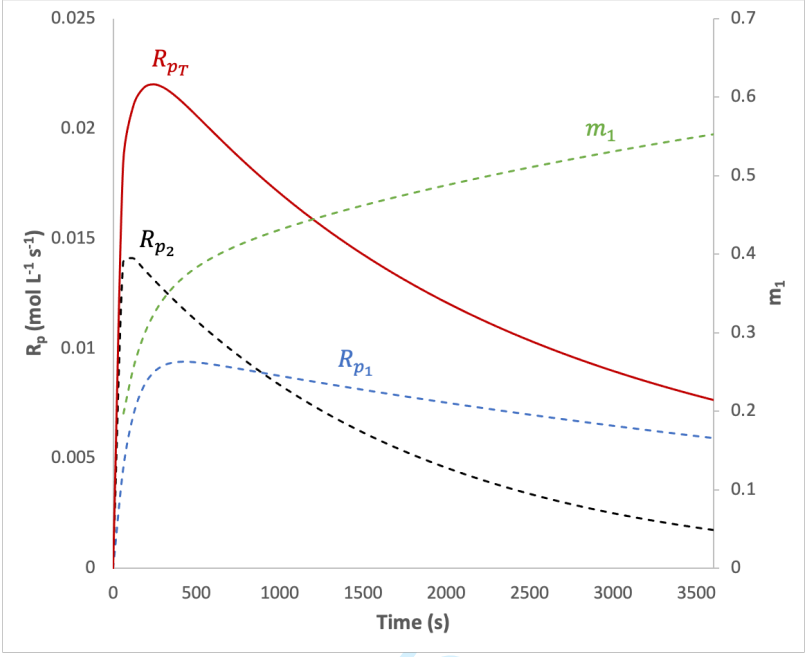

Figure 13 Polymerization rates for a dual site catalyst. Model parameters: 1) $f_{p_1} = 1 \times 10^5$ s^{-1}, $f_{a_1} = 1 \times 10^{-2}$ s^{-1}, $f_{d_1} = 1.5 \times 10^{-4}$ s^{-1}, $[C_0]_1 = 1 \times 10^{-8}$ mol·L^{-1}, $M_{n_1} = 200\,000$, 2) $f_{p_2} = 1.5 \times 10^5$ s^{-1}, $f_{a_2} = 5 \times 10^{-2}$ s^{-1}, $f_{d_2} = 6 \times 10^{-4}$ s^{-1}, $[C_0]_2 = 1 \times 10^{-8}$ mol·L^{-1}, $M_{n_2} = 40\,000$. $V_R = 1$ L, $\bar{M} = 28$ (polyethylene).

In this catalyst, site 1 makes polymer with higher molecular weight ($M_{n_1} = 200\,000$, $PDI_1 = 2$) than site 2 ($M_{n_2} = 40\,000$, $PDI_2 = 2$). Even though the MWDs of the populations made on each site type do not change during the polymerization, their proportions do. Consequently, the MWD of the whole polymer changes during the polymerization, as shown in Figure 14. This figure elucidates how phenomena taking place in the Polymerization Kinetics level affect the properties defined in the Catalysis level. As we explained above, time now plays a major role: the individual MWDs remain the same (Catalyst level), but their combination (Polymerization Kinetics level) does not.

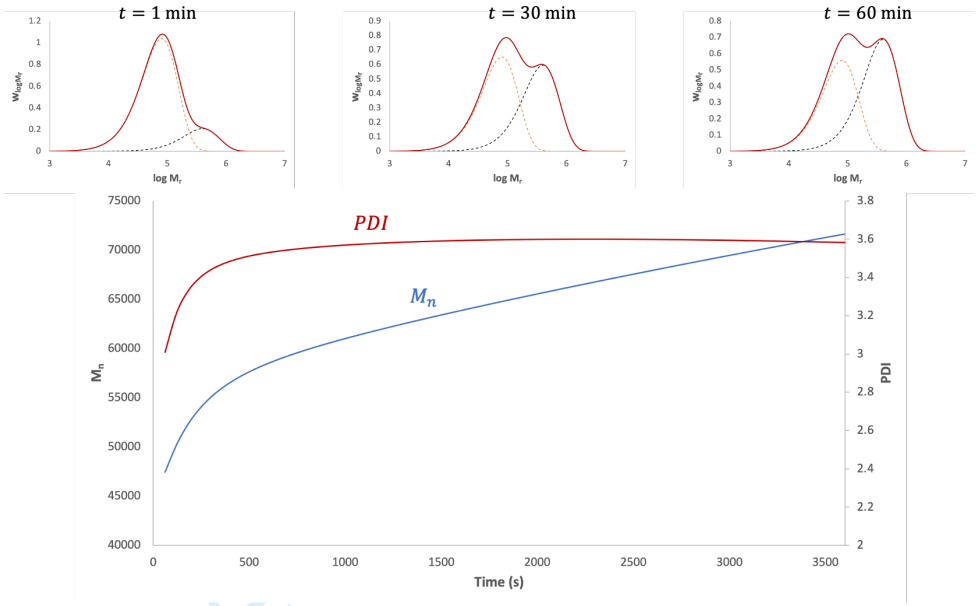

Figure 14 Molecular weight averages and MWDs for polyethylene made with the dual catalysts shown in Figure 13.

Let's now examine a model for copolymerization kinetics. Binary copolymerizations that follow the Terminal Model (Markov Order 1) require four different propagation steps,[7]

$$P_{r_1} + M_1 \xrightarrow{k_{p11}} P_{(r+1)_1} \tag{45}$$

$$P_{r_1} + M_2 \xrightarrow{k_{p12}} P_{(r+1)_2} \tag{46}$$

$$P_{r_2} + M_1 \xrightarrow{k_{p21}} P_{(r+1)_1} \tag{47}$$

$$P_{r_2} + M_2 \xrightarrow{k_{p22}} P_{(r+1)_2} \tag{48}$$

We could start from scratch and derive a copolymerization model for the mechanism defined by Eq. (45) to (48). However, it is more expedient to transform the homopolymerization model quantified in Eq. (39) into a copolymerization model by substituting k_p—or f_p, see Eq. (3)—with the pseudo-kinetic constant $\hat{k}_p$. Differently from a conventional rate constant, which depends only on temperature, pseudo-kinetic constants also depend on the molar fractions of the chemical species involved in the reaction.[8]-[10] Thus, if the chemical composition around the active sites changes during the polymerization, so does the value of $\hat{k}_p$. The pseudo-kinetic propagation constant for this binary copolymerization is given by,

$$\hat{k}_p = k_{p_{11}}\phi_1 f_1 + k_{p_{12}}\phi_1 f_2 + k_{p_{21}}\phi_2 f_1 + k_{p_{22}}\phi_2 f_2 \quad (49)$$

where f_i is the molar fraction of monomer type i at the active site and ϕ_i is the molar fraction of growing chains terminated in monomer type i.

It is easy to calculate ϕ_1 by making the long chain approximation, which assumes that in a population of polymer with long chains, the number of sequences M_1M_2 equals that of M_2M_1,[7]

$$\phi_1 = \frac{k_{p_{21}} f_1}{k_{p_{21}} f_1 + k_{p_{12}} f_2} = \frac{f_{p_{21}}}{f_{p_{21}} + f_{p_{12}}} \quad (50)$$

We can calculate the pseudo-propagation frequency, $\hat{f}_p$, by multiplying both sides of Eq. (49) by the total concentration of comonomers at the active site, $[M_T]_s = [M_1]_s + [M_2]_s$,

$$\hat{f}_p = \left(f_{p_{11}} + f_{p_{12}}\right)\phi_1 + \left(f_{p_{21}} + f_{p_{22}}\right)\phi_2 \quad (51)$$

Therefore, the equations for copolymerization rate and yield become,

$$R_p = \hat{f}_p \frac{1 - \exp[-f_a(1 - f_d/f_a)t]}{1 - f_d/f_a}[C_0]\exp(-f_d t) \quad (52)$$

$$Y_p = \frac{\hat{f}_p}{1 - f_d/f_a}\left[\frac{1 - \exp\left(-f_d t_p\right)}{f_d} - \frac{1 - \exp\left(-f_a t_p\right)}{f_a}\right]\bar{M}[C_0]V_R \quad (53)$$

The values for f_d and f_a remain the same since they do not depend on the fraction of monomer 1 and 2 at the active sites.

Figure 15 shows how the copolymerization rate depends on the molar fraction of comonomer according to this model. Since monomer 2 (the α-olefin) reacts more slowly than monomer 1 (ethylene), the value of $\hat{f}_p$ and the rate of polymerization decrease as the fraction of α-olefin at the active site increases, but the shape of the R_p curve remains the same.

This behaviour has been observed for SS catalysts,[49] but it may not be enough to explain the copolymerization kinetics of ethylene and α-olefins with MS catalysts (and less often with some SS catalysts), for which R_p unexpectedly increases when an α-olefin is present in small concentrations in the reactor. This rate enhancement behavior—sometimes called *the comonomer effect*—is counterintuitive since we know that α-olefins polymerize at slower rates than ethylene ($k_{p_{22}} \ll k_{p_{11}}$). Two main explanations have been offered for this observation, based on physical or chemical effects. The physical effect hypothesis attributes the rate enhancement to the higher solubility of ethylene and α-olefins in the less crystalline ethylene/α-olefin copolymer phase surrounding the active sites and to cosolubility effects, phenomena that we will discuss later in this article. A few models have been proposed for the chemical effect hypothesis, such as β-agostic interactions or the trigger mechanism, but none has reached a wide consensus. The curious reader

can find out how to modify the copolymerization model in Eq. (52) to account for the comonomer rate enhancement effect in our book.[7]

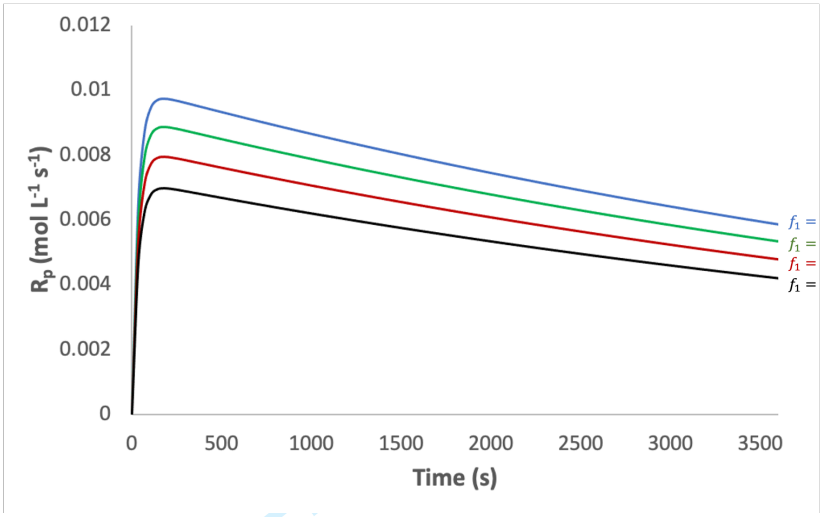

Figure 15 Copolymerization rates as a function of comonomer composition in the reactor. Model parameters: $[M_T]_s = 1$ mol·L^{-1}, $[C_0] = 1 \times 10^{-8}$ mol·L^{-1}, $k_{p_{11}} = 1 \times 10^5$ L·mol^{-1}·s^{-1}, $k_{p_{12}} = 1 \times 10^4$ L·mol^{-1}·s^{-1}, $k_{p_{21}} = 5 \times 10^4$ L·mol^{-1}·s^{-1}, $k_{p_{22}} = 5 \times 10^3$ L·mol^{-1}·s^{-1}, $f_a = 0.03$ s^{-1}, $f_d = 1.5 \times 10^{-4}$ s^{-1}.

Like the homopolymerization case above, the bivariate MWD-CCD of a polyolefin made with an SS catalyst is not affected by polymerization time. However, the MWD-CCD of a polymer made with an MS catalyst having sites types with distinct activation and deactivation frequencies does depend on time.

The rates of polymerization and yield of an MS catalyst used for copolymerization are calculated with the equations,

$$R_{p_T} = \sum_{i=1}^{n} R_{p_i} = [C_0]_T \sum_{i=1}^{n} x_{i_0} \hat{f}_{p_i} \frac{1 - \exp\left[-f_{a_i}\left(1 - f_{d_i}/f_{a_i}\right)t\right]}{1 - f_{d_i}/f_{a_i}} \exp\left(-f_{d_i} t\right) \tag{54}$$

$$Y_{p_T} = \sum_{i=1}^{n} R_{p_i} = \bar{M}[C_0]_T V_R \sum_{i=1}^{n} x_{i_0} \frac{\hat{f}_{p_i}}{1 - f_{d_i}/f_{a_i}} \left[\frac{1 - \exp\left(-f_{d_i} t_p\right)}{f_{d_i}} - \frac{1 - \exp\left(-f_{a_i} t_p\right)}{f_{a_i}}\right] \tag{55}$$

Figure 16 shows the predicted rates of copolymerization of ethylene and 1-hexene made with a dual site catalyst. The particular combination illustrated in Figure 16 is interesting, but undesirable, because site 1 activates faster and deactivates more slowly than site 2, while all propagation frequencies of site 2 are higher than those of site 1. Consequently, the mass fraction of polymer made in site 1 is initially high, passes through a minimum as site 2 activates slowly, then increases again as site 2 deactivates faster than site 1.

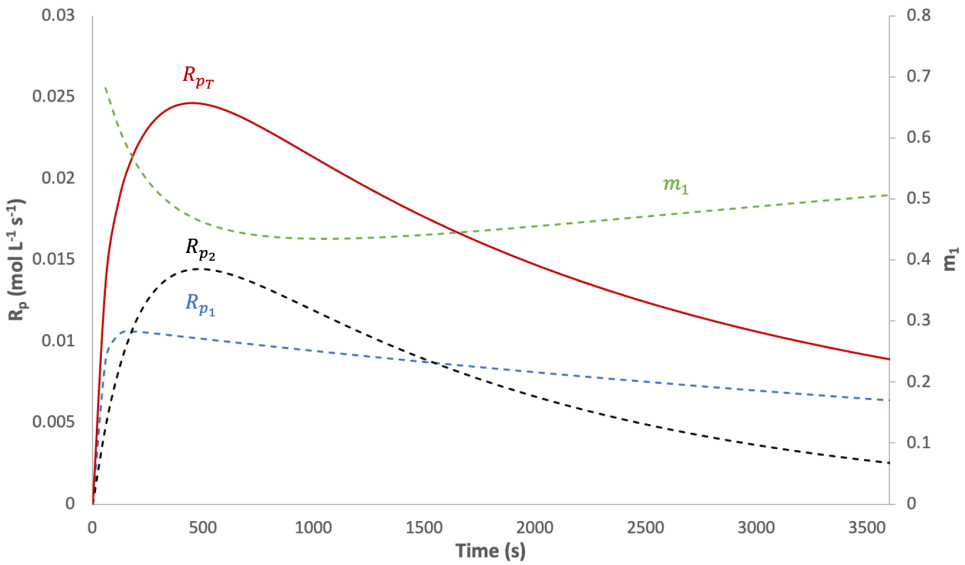

Figure 16 Polymerization rates for the copolymerization of ethylene and 1-hexene with a dual site catalyst when the molar fraction of ethylene in the active sites is $f_1 = 0.9$ and $V_R = 1$ L. Model parameters: 1) $f_{p_{11,1}} = 1 \times 10^5$ s^{-1}, $f_{p_{12,1}} = 1 \times 10^4$ s^{-1}, $f_{p_{21,1}} = 5 \times 10^4$ s^{-1}, $f_{p_{22,1}} = 5 \times 10^3$ s^{-1}, $r_{1_1} = 10$, $r_{2_1} = 0.1$, $f_{a_1} = 3 \times 10^{-2}$ s^{-1}, $f_{d_1} = 1.5 \times 10^{-4}$ s^{-1}, $[C_0]_1 = 1 \times 10^{-8}$ mol·L^{-1}, $M_{n_1} = 200\,000$, $\bar{F}_{1_1} = 0.9890$, 2) $f_{p_{11,2}} = 1.5 \times 10^3$ s^{-1}, $f_{p_{12,2}} = 5 \times 10^4$ s^{-1}, $f_{p_{21,2}} = 7.5 \times 10^4$ s^{-1}, $f_{p_{22,2}} = 2.5 \times 10^4$ s^{-1}, $r_{1_2} = 3$, $r_{2_2} = 0.333$, $f_{a_2} = 5 \times 10^{-3}$ s^{-1}, $f_{d_2} = 6 \times 10^{-4}$ s^{-1}, $[C_0]_2 = 1 \times 10^{-8}$ mol·L^{-1}, $M_{n_2} = 40\,000$, $\bar{F}_{1_2} = 0.9643$.

This mismatch in polymerization kinetics between the two site types, combined with the fact that site 2 makes polymer with lower molecular weight averages and higher 1-hexene fractions than site 1, causes the MWD-CCD to change substantially during the polymerization, as depicted in Figure 17. Therefore, the reactor average residence time affects the properties of the ethylene/1-hexene copolymer substantially, which is bad news indeed. We only used this example to illustrate how phenomena taking place in the Polymerization Kinetics level may affect the polymer properties arising from the Catalysis level.

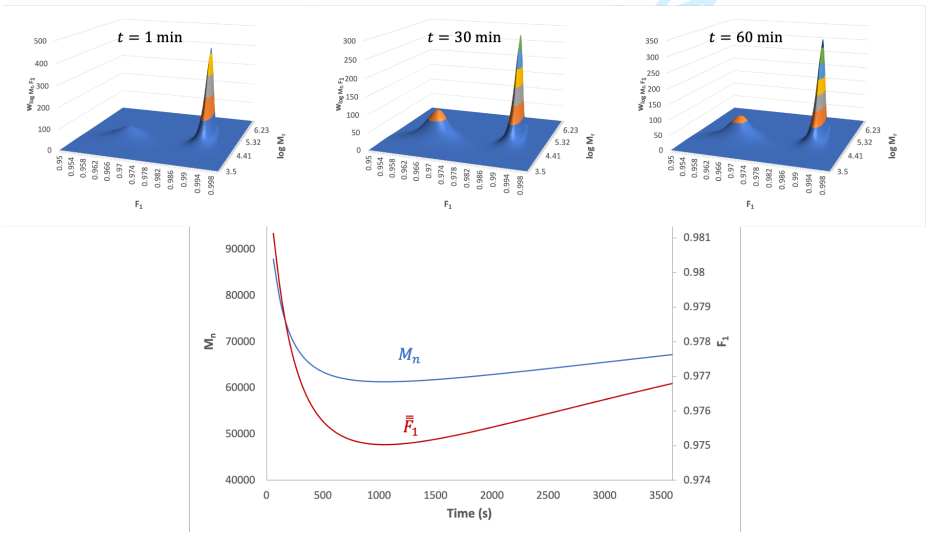

Figure 17 Effect of polymerization time on the MWD-CCD of an ethylene/1-hexene copolymer made with a dual SS catalysts. Simulation parameters are shown in Figure 16.

Hydrogen is used to control the molecular weight of industrial polyolefins. In addition to acting as a chain transfer agent, it also affects the polymerization rate, particularly with heterogeneous Ziegler-Natta catalysts: hydrogen typically decreases the polymerization rate of ethylene, but increases the polymerization rate of propylene. From a polyolefin reaction engineering perspective, we can handle this effect in two ways. The simplest and most pragmatic is to estimate k_p values at different hydrogen concentrations using the models we showed above and use an empirical correction factor, η_H, to account for the hydrogen effect,[7]

$$R_p = \eta_H f_p \frac{1 - \exp[-f_a(1 - f_d/f_a)t]}{1 - f_d/f_a}[C_0]\exp(-f_d t) \tag{56}$$

A few mechanisms, such as slow metal-hydride initiation and β-agostic interactions have been suggested to explain how hydrogen affects the rate of ethylene polymerization.[56]-[60] The former assumes that metal-hydride sites formed after transfer to hydrogen or β-hydride elimination incorporate ethylene at slower rates than sites formed after transfer to ethylene or cocatalyst. In this case, we can show that the correction factor η_H is given by the equation,[7]

$$\eta_H = \frac{f_p}{1 + \frac{f_{t_H} + f_{t_\beta}}{f_{i_H}}} \tag{57}$$

where f_{i_H} is the frequency of monomer insertion in metal-hydride sites. Eq. (57) teaches us that if $f_{i_H} \ll f_{t_H} + f_{t_\beta} \ll f_p$, then $\eta_H < 1$. Similarly, if $f_{i_H} \cong f_p \gg f_{t_H} + f_{t_\beta}$, then $\eta_H \cong 1$, and hydrogen does not affect the polymerization rate of ethylene. The model based on β-agostic interactions is more elaborate, but eventually leads to an expression that is an extension of Eq. (57).[7] If neither of these more fundamental models work, the simplest option is to find an empirical expression for η_H that fits your experimental data.

In contrast, hydrogen usually increases the polymerization rate of propylene with Ziegler-Natta catalysts. The most accepted explanation is that living polypropylene chains terminated in 2-1 insertions incorporate propylene more slowly than those terminated in 1-2 units.[61]-[63] When added to the reactor, H_2 can reactivate these "dormant" sites in a process that has been shown to be reversible.[64],[65] Assuming that the rate of propylene consumption by 2-1 terminated sites is negligible, the rate of propylene polymerization is given by,[7]

$$R_p = \eta_{12} f_p \frac{1 - \exp[-f_a(1 - f_d/f_a)t]}{1 - f_d/f_a}[C_0]\exp(-f_d t) \tag{58}$$

where η_{12} is the molar fraction of active sites terminated in 1-2 insertions,

$$\eta_{12} = \frac{1 + f_{t_{H,21}}/f_{p_{21,12}}}{1 + f_{t_{H,21}}/f_{p_{21,12}} + f_{p_{12,21}}/f_{p_{21,12}}} = \frac{1 + \tau_{21}}{1 + \tau_{21} + \pi} \tag{59}$$

where $f_{t_{H,21}}$ is the frequency of transfer to hydrogen of 2-1 terminated sites, $f_{p_{12,21}}$ is the frequency of 2-1 insertions on 1-2 terminated sites, and $f_{p_{21,12}}$ is the frequency of 1-2 insertions on 2-1 terminated sites. The parameter τ_{21} is the ratio of the frequencies of transfer to hydrogen and 1-2 propagation for 2-1 (dormant) sites, and π is the ratio of the frequencies for 1-2 to 2-1 and 2-1 to 1-2 insertions (changes in regioregularity). If τ_{21} (high transfer to H_2 frequency) is much larger than π, then $\eta_{12} \to 1$ and the polymerization rate increases. Figure 18 shows how the fraction of 1-2 terminated sites approaches 1 as $f_{p_{12,21}} \to 0$ (no regio-insertion defects) and $f_{t_{H,21}} \gg f_{p_{21,12}}$ (high transfer to H_2 frequency).

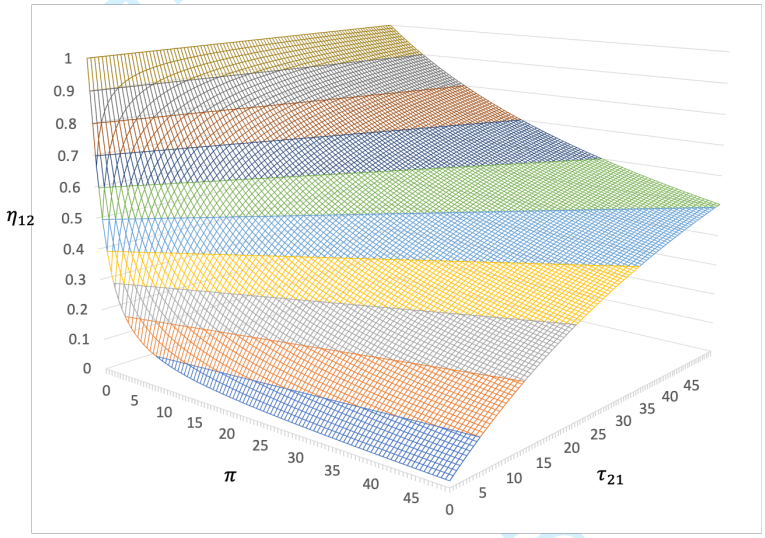

Figure 18 Effect of $\tau_{21} = f_{t_{H,21}}/f_{p_{21,12}}$ and $\pi = f_{p_{12,21}}/f_{p_{21,12}}$ on the fraction of sites terminated in 1-2 propylene insertions according to the model in Eq. (59).

Typically, three or more site types are needed to describe the microstructural distributions of polyolefins made with an MS catalyst, each associated with one type of active site, as we have shown in the Catalyst section above. To be consistent, we should anticipate the same number of sets of parameters to describe the polymerization kinetics with these catalysts. Even though methods have been proposed for this type of detailed estimation, more pragmatically we can often describe the polymerization rate with an MS catalyst with only one or two sets of *lumped* f_a, f_p, and f_d. This simplification works when the values of f_a and f_d of the different site types are similar, even if their f_p values are different. Figure 19 illustrates this behaviour for an MS catalyst with four site types having different values for f_{p_i}, but the same for f_{a_i} and f_{d_i}. (Incidentally, since all site types activate and deactivate at the same rates, the microstructural distributions of the polymers made with the catalyst in Figure 19 would not depend on reactor residence time. This type of site type combination is the most adequate to assure that the polymer properties are independent of polymerization time.)

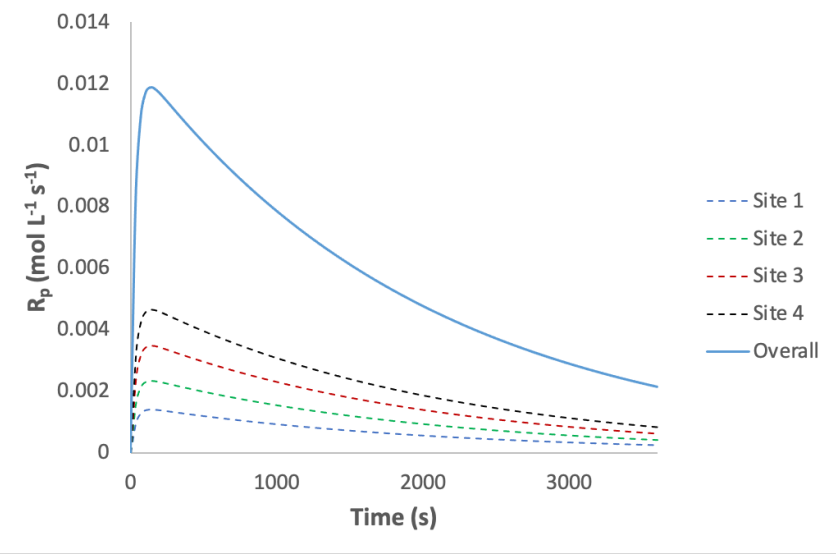

Figure 19 Polymerization kinetics with an MS catalyst. The activation and deactivation constants were assumed to be the same for all site types. Model parameters: $f_a = 3 \times 10^{-2}$ s^{-1}, $f_d = 5 \times 10^{-4}$ s^{-1}, 1) $f_{p_1} = 5 \times 10^4$ s^{-1}, $x_1 = 0.3$, 2) $f_{p_2} = 1 \times 10^5$ s^{-1}, $x_2 = 0.25$, 3) $f_{p_3} = 1.5 \times 10^5$ s^{-1}, $x_3 = 0.25$, 4) $f_{p_4} = 2.5 \times 10^5$ s^{-1}, $x_4 = 0.2$. $\tilde{f}_p = 1.275 \times 10^5$ s^{-1}, $[C_0]_T = 1 \times 10^{-4}$ mol·L^{-1}.

From Eq. (54), it is easy to see that the lumped propagation frequency, $\tilde{f}_p$, for this MS catalyst is given by the weighted average,

$$\tilde{f}_p = \sum_{i=1}^{n} x_{i_0} f_{p_i} \tag{60}$$

Another important phenomena that must be considered in mathematical models at this level are the effects of cocatalyst type and cocatalyst/catalyst ratio on polymerization kinetics parameters, propagation-to-transfer ratios (τ), and reactivity ratios.[66]-[69] These parameters are also affected by internal and external electron donors used in catalysts for propylene polymerization.[50],[54],[70]-[72] From a fundamental modeling point of view, we know very little on how to account for these factors *a priori*. The usual, and often frustrating, approach is to re-estimate the necessary model parameters when different types and concentrations of cocatalysts and/or electron donors are used with a given catalyst type.

2.3 Thermodynamic Equilibrium

We need to know the concentrations of all reactive species (ethylene, propylene, α-olefins, hydrogen, etc.) at the active sites to use the models described in the Catalysis and Polymerization Kinetics levels. These concentrations are relatively easy to estimate for solution polymerization reactors, in which polymer, solvent, and reagents coexist in a liquid homogeneous medium, but they are harder to estimate for gas-phase and slurry polymerizations promoted by heterogeneous catalysts because they are the concentrations of reagents in the amorphous polymer phase surrounding the active sites. In a gas-phase polymerization, the reagents are partitioned between

the gas phase and the amorphous polymer phase; in slurry polymerizations, the partition also involves the liquid diluent phase suspending the catalyst particles.[73]

Under thermodynamic equilibrium, the chemical potential of species i is the same among different phases,

$$\mu_{i_s} = \mu_{i_l} = \mu_{i_g} \tag{61}$$

where the subscripts g, l, and s refer to gas, liquid, and solid phases, respectively.

The formulation in Eq. (61) is as general as possible, but of little use in polyolefin reaction engineering studies. In its simplest form, assuming ideal gas and ideal solution behaviors, the concentration of a small molecule (such as the monomer) coexisting in different phases is quantified with linear equations,

$$[M]_s = H_{M_{s-l}}[M]_l \tag{62}$$

$$[M]_s = H_{M_{s-g}}[M]_g \tag{63}$$

$$[M]_l = H_{M_{l-g}}[M]_g \tag{64}$$

where $H_{M_{s-l}}$, $H_{M_{s-g}}$, and $H_{M_{l-g}}$ are the partition coefficients (or Henry's Law constants) for the monomer between solid-liquid, solid-gas, and liquid-gas phases, respectively. These partition coefficients depend on temperature, polymer microstructure, and monomer type. Similar expressions can be written for comonomer, hydrogen, diluent, or any other small molecule that can absorb in the amorphous polymer phase.

When these equations can be applied, calculating the concentration of monomer and other chemical species at the active sites is straightforward. Let's consider the simplest case of ethylene homopolymerization in a gas-phase reactor. How do we incorporate these equilibrium relations in the calculation of the parameter τ in Flory MPD? Substituting the required phase equilibrium equations for monomer and chain transfer agent in Eq. (8), we obtain an analogous equation for τ as a function of the concentrations of monomer and chain transfer agent in the gas phase of the reactor,

$$\tau = \mathrm{K}_M + \mathrm{K}_X \frac{H_{X_{s-g}}}{H_{M_{s-g}}} \cdot \frac{[X]_g}{[M]_g} + \mathrm{K}_\beta \frac{1}{H_{M_{s-g}}} \cdot \frac{1}{[M]_g} \tag{65}$$

In Eq. (65) we also assumed no resistances to diffusion of the penetrant species in the amorphous phase of the polymer. You will read more about how these resistances may affect the simulation results in the following section.

Similarly, we can transform Eq. (39) for the rate of polymerization to the following expression,

$$R_p = f_{p_g} \frac{1 - \exp[-f_a(1 - f_d/f_a)t]}{1 - f_d/f_a} [C_0] \exp(-f_d t) \quad (66)$$

where f_{p_g} is the propagation frequency based on the concentration of monomer in the gas phase,

$$f_{p_g} = H_{M_{s-g}} k_p [M]_g \quad (67)$$

If the ideal equilibrium equations formulated in Eq. (62) to (64) were enough to describe all olefin polymerization conditions, the Thermodynamic Equilibrium level would be a trivial exercise. This, evidently, is not true. Even though linear relations governed by partition coefficients have been used widely and are adequate for low to moderate concentrations of single light penetrants, they fail to describe more complex, multicomponent systems under a wider range of conditions that lead to the swelling or plasticization of the polymer amorphous phase. More advanced thermodynamic equilibrium models, such as the Sanchez-Lacombe and perturbed-chain statistical association fluid theory (PC-SAFT) equations of state, are recommended for these cases.[74]-[76]

The Sanchez-Lacombe equation of state is based on the Flory-Huggins theory. It has been applied to model phase equilibria of the different components in olefin polymerization reactors, being one of the most widely used thermodynamic models in the polymer industry. It predicts well the thermodynamic properties of small molecules, polymer chains, and their mixtures. The behavior of a pure component is estimated with three parameters: characteristic temperature, characteristic pressure, and close-packed density. Mixtures require additional parameters, k_{ij}, that account for binary interactions between components i and j. These parameters are used to fit the Sanchez-Lacombe model to experimental solubility data. The PC-SAFT equation of state is based on statistical associating fluid theory and uses statistical mechanics methods. Independently of which equation of state is selected, they introduce methods to describe how the presence of one species affect the concentrations of the other species in the system, which is lacking from the ideal Henry's Law models in Eq. (62) to (64).

What is the effect of the Thermodynamic Equilibrium level on the Catalysis or Polymerization Kinetics level? If we assume the ideal behaviour described in Eq. (62) to (64), the answer is a disappointing *none*. These equations teach us that the concentrations of reactive species at the active sites are linear functions of their concentrations in the bulk gas or liquid phases of the reactor. As we already saw above in Eq. (65) to (67), our previous equations can be reformulated in terms of bulk concentrations using partition coefficients that depend only on temperature for a given polymer–small molecule pair. What these ideal equations cannot do, however, is to predict how the components of a multicomponent mixture of monomer, comonomer, hydrogen, diluent, and condensing agents interact (as quantified by the parameters k_{ij} in the Sanchez-Lacombe model, for instance) and affect each other's concentrations in the vicinity of the active sites.

Instead of stating that the concentration of monomer in the amorphous polymer phase is only a function of the temperature and monomer concentration in the liquid or gas phase,

$$[M]_s = f(T, [M]_{l,g}) \tag{68}$$

models such as Sanchez-Lacombe and PC-SAFT postulate that $[M]_s$ is a complex function that also depends on the concentration of many other species in the reactor,

$$[M_1]_s = f(T, [M_1]_{l,g}, [M_2]_{l,g}, \dots, [X]_{l,g}, \dots) \tag{69}$$

where $[X]_{l,g}$ is the concentration of other small molecules such as hydrogen, nitrogen, diluent, and condensing agents.

Now, things start becoming more interesting at the Thermodynamic Equilibrium level, don't they? Let's start exploring how these cosolubility effects may alter the two previous modeling levels by modeling the polymerization rate, MWD, and CCD of ethylene/1-hexene copolymers made in a gas-phase reactor in the presence of an induced condensing agent (ICA) such as n-pentane. It has been reported that increasing the partial pressure of n-pentane makes causes an increase in the rate of polymerization, R_p, a decrease in the molar fraction of 1-hexene in the copolymer, $\bar{F}_2$, and an increase in the polymer molecular weight average, M_w.[77] Since n-pentane is an inert, a plausible explanation for these responses is to assume that n-pentane acts as a *cosolvent* for ethylene (increasing $[M_1]_s$ and consequently R_p and M_w) and as an *antisolvent* for 1-hexene (decreasing $[M_2]_s$ and consequently $\bar{F}_2$). This effect, evidently, would be missed by an ideal solution model for gas-solid equilibrium.

This effect is investigated in Figure 20 for the copolymerization of ethylene and 1-hexene with a supported SS catalyst in a gas phase reactor. The plots on the right side show how the partial pressure of n-pentane changes the concentrations of ethylene and 1-hexene at the active sites.

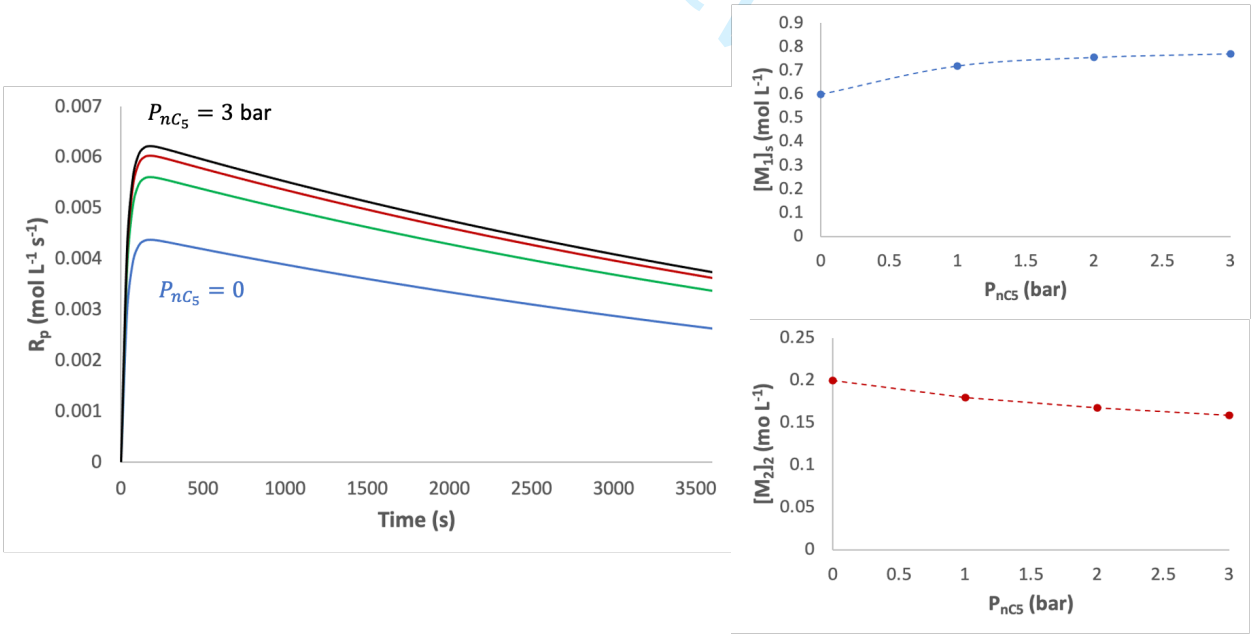

Figure 20 Effect of n-pentane (nC_5) partial pressure on ethylene/1-hexene polymerization rate with an SS catalyst. Model parameters: $[C_0] = 1 \times 10^{-8}$ mol·L^{-1}, $k_{p_{11}} = 1 \times 10^5$ L·mol^{-1}·s^{-1}, $k_{p_{12}} = 1 \times 10^4$ L·mol^{-1}·s^{-1}, $k_{p_{21}} = 5 \times 10^4$ L·mol^{-1}·s^{-1}, $k_{p_{22}} = 5 \times 10^3$ L·mol^{-1}·s^{-1}, $f_a = 0.03$ s^{-1}, $f_d = 1.5 \times 10^{-4}$ s^{-1}.

Increasing the partial pressure of n-pentane increases the concentration of ethylene (cosolvent effect) and decreases the concentration of 1-hexene (antisolvent effect) in the vicinity of the active sites. Since ethylene is more reactive than 1-hexene (neglecting the comonomer effect discussed above) the rate of polymerization also increases when more n-pentane is added to the reactor. Note that the propagation rate constants $k_{p_{11}}$, $k_{p_{12}}$, $k_{p_{21}}$, and $k_{p_{22}}$(listed in the caption of Figure 20) remain the same, since they depend only on temperature, but the propagation frequencies $f_{p_{11}}$, $f_{p_{12}}$, $f_{p_{21}}$, and $f_{p_{22}}$ (see Table 3) change because the concentrations of ethylene and 1-hexene at the active sites are affected by how much n-pentane is added to the reactor. If we ignored this fact and used only the concentrations of ethylene and 1-hexene in the gas phase, $[M_1]_g$ and $[M_2]_g$, we would conclude, erroneously, that the partial pressure of n-pentane affected the propagation rates of ethylene and 1-hexene.

Since the total and relative concentrations of ethylene and 1-hexene depend on how much n-pentane is absorbed in the polymer particles, we should expect that the joint MWD-CCD of the polymer will also be affected by the presence of the ICA. And indeed, it is. Assuming that no hydrogen or other chain transfer agent was added to the reactor, the definition of Flory MPD's parameter τ for this binary copolymer is,

$$\tau = \frac{\hat{k}_{t_M}}{\hat{k}_p} + \frac{\hat{k}_{t_\beta}}{\hat{k}_p([M_1]_s + [M_2]_s)} \tag{70}$$

where $\hat{k}_p$ is the pseudo propagation rate constant, defined in Eq. (49), and the pseudo rate constants for transfer to monomer/comonomer and β-hydride elimination are given by the following equations,

$$\hat{k}_{t_M} = k_{t_{M_{11}}}\phi_1 f_1 + k_{t_{M_{12}}}\phi_1 f_2 + k_{t_{M_{21}}}\phi_2 f_1 + k_{t_{M_{22}}}\phi_2 f_2 \tag{71}$$

$$\hat{k}_{t_\beta} = k_{t_{\beta_1}}\phi_1 + k_{t_{\beta_2}}\phi_2 \tag{72}$$

Substituting these definitions in Eq. (70) and converting the kinetic rate constants into frequencies, we arrive at the equation,

$$\tau = \frac{\left(f_{t_{M_{11}}} + f_{t_{M_{12}}}\right)\phi_1 + \left(f_{t_{M_{21}}} + f_{t_{M_{22}}}\right)\phi_2 + f_{t_{\beta_1}}\phi_1 + f_{t_{\beta_2}}\phi_2}{\left(f_{p_{11}} + f_{p_{12}}\right)\phi_1 + \left(f_{p_{21}} + f_{p_{22}}\right)\phi_2} \tag{73}$$

which would never win a contest for the most beautiful equation in polyolefin reaction engineering, but it is still a useful definition of the parameter τ in terms of propagation and chain transfer frequencies.

We are now ready to calculate what effect n-pentane may have in the MWD of ethylene/1-hexene copolymers using Flory MPD, Eq. (9). Figure 21 shows that the MWD shifts towards higher averages as the pressure of n-pentane in the reactor increases, since the rate of propagation-to-transfer to ethylene is higher than that for 1-hexene. Note that the chain transfer constants listed

in the caption of Figure 21 remain the same: M_w increases solely because the concentration of ethylene increases and the concentration of 1-hexene decreases at the active sites.

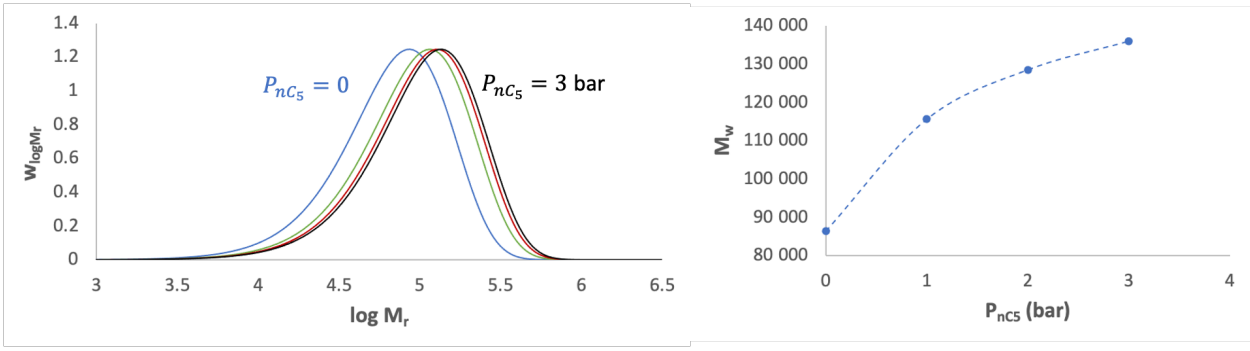

Figure 21 Effect of n-pentane (nC_5) pressure the MWD and M_w of ethylene/1-hexene copolymers made with a supported SS catalyst. Model parameters (in addition to those listed in the caption of Figure 20): $k_{t_{M_{11}}} = 1$ L·mol^{-1}·s^{-1}, $k_{t_{M_{12}}} = 100$ L·mol^{-1}·s^{-1}, $k_{t_{M_{21}}} = 1$ L·mol^{-1}·s^{-1}, $k_{t_{M_{22}}} = 100$ L·mol^{-1}·s^{-1}, $k_{\beta_1} = 10$ s^{-1}, $k_{\beta_2} = 100$ s^{-1}.

Table 3 Effect of n-pentane on the frequencies of propagation and chain transfer, and on the average molecular weights and compositions of an ethylene/1-hexene copolymer made with a model supported SS catalyst.

	n-Pentane Pressure (bar)			
	0	1	2	3
$[M_1]_s$	0.6	0.72	0.756	0.771
$[M_2]_s$	0.2	0.18	0.167	0.159
f_1	0.75	0.8	0.923	0.93
ϕ_1	0.938	0.952	0.958	0.960
$f_{p_{11}}$	4.5×10^4	5.8×10^4	6.2×10^4	6.4×10^4
$f_{p_{12}}$	1.5×10^3	1.4×10^3	1.4×10^3	1.3×10^3
$f_{p_{21}}$	2.3×10^4	2.9×10^4	3.1×10^4	3.2×10^4
$f_{p_{22}}$	7.5×10^2	7.2×10^2	7.0×10^2	$7.\times10^2$
$\hat{f}_p$	4.5×10^4	5.8×10^4	6.2×10^4	6.4×10^4
$f_{t_{M_{11}}}$	0.45	0.58	0.62	0.64
$f_{t_{M_{12}}}$	15	14.4	13.7	13.1
$f_{t_{M_{21}}}$	0.45	0.58	0.62	0.64
$f_{t_{M_{22}}}$	15	14.4	14.3	13.8
$\hat{f}_{t_M}$	15.5	15	14.3	13.8
f_{β_1}	10	10	10	10
f_{β_2}	100	100	100	100
$\hat{f}_\beta$	15.6	14.3	13.8	13.6
$\hat{\tau}$	2.31×10^{-5}	1.73×10^{-5}	1.56×10^{-5}	1.47×10^{-5}
M_n	43 208	57 839	64 283	68 024
M_w	86 416	115 679	128 566	136 049
$\bar{F}_1$	0.968	0.976	0.978	0.980

Table 3 illustrates how the propagation and transfer frequencies, as well as average molecular weights, vary with n-pentane concentration according to this model. Table 3 also shows

how the average fraction of ethylene in the copolymer depends on the concentration of n-pentane absorbed in the polymer particles. With this information in hand, we can use the CCD component of the Stockmayer BD, Eq. (24), to describe how the CCD changes under these conditions (Figure 22).

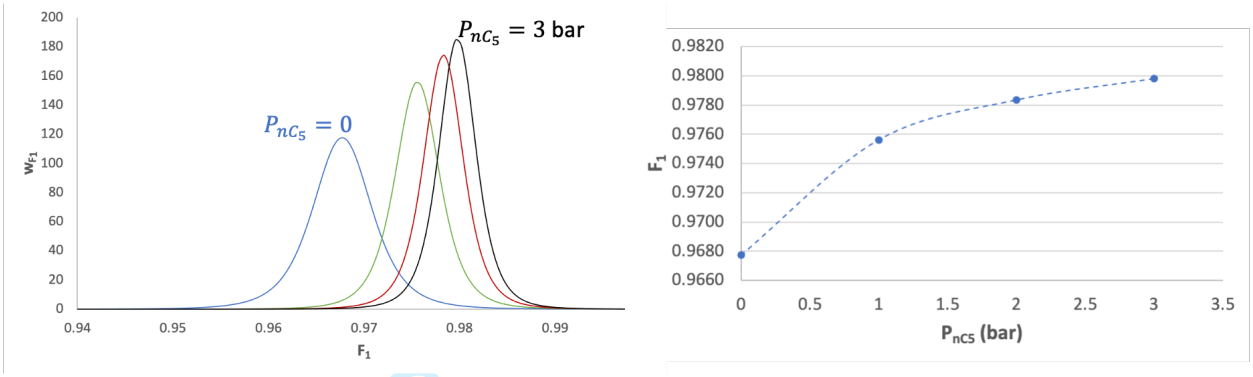

Figure 22 Effect of n-pentane (nC_5) pressure on the CCD and $\bar{F}_1$ of ethylene/1-hexene copolymers made with a supported SS catalyst. Model parameters are listed in Figure 20 and 21.

Finally, if we wish, we can visualize the effect of n-pentane on the joint CCD-MWD of these copolymers using Eq. (17), as shown in Figure 23. As P_{nC_5} increases, the Stockmayer BD becomes narrower and shifts towards lower 1-hexene fractions and higher molecular weights.

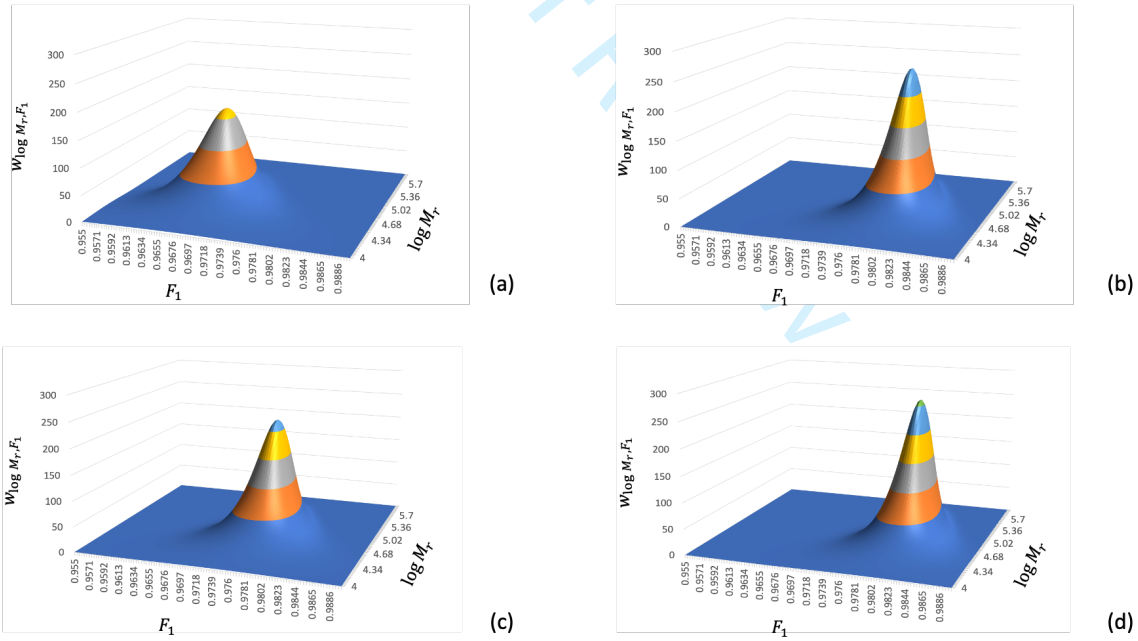

Figure 23 Effect of n-pentane (nC_5) pressure on the bivariate MWD-CCD of ethylene/1-hexene copolymers made with a supported SS catalyst. Model parameters are listed in Figure 20 and 21: a) $P_{nC_5} = 0$ bar, b) $P_{nC_5} = 1$ bar, c) $P_{nC_5} = 2$ bar, d) $P_{nC_5} = 3$ bar.

Even though the simulations above described the microstructure and yield of a copolymer made with a supported SS catalyst, the same approach could be extended to a heterogeneous MS

catalyst, such as a Ziegler-Natta catalyst, or for the case when two or more metallocene catalysts are supported on the same carrier.

This example is just the tip of the iceberg on how thermodynamic equilibrium in multicomponent mixtures may affect the microstructure and yield of polyolefins. Another intriguing example of phenomena occurring at this scale is observed when we compare the performances of the same catalyst in gas-phase and slurry reactors. We could naively assume that if the concentration of all reactive species were the same in the bulk phases of both reactors (gas phase and liquid diluent), then all other factors being the same at the Catalysis (same catalyst type) and Polymerization Kinetics (same activation, deactivation and propagation rates) levels, the polymers made on both reactors would have identical microstructures and polymerization rate curves. In reality, as may be apparent after we explained the effect of n-pentane above, the diluent in the slurry reactor changes the concentration of monomer and comonomer near the active sites, thus affecting the polymer microstructure and yield.[73] Many publications in the literature emphasize the importance of equilibrium thermodynamics for the complete understanding of olefin polymerization processes.[78]-[94]

2.4 Particle Transport Phenomena

A few inorganic carriers have been used to support coordination catalysts for olefin polymerization. Ziegler-Natta catalysts are typically supported on $MgCl_2$, while Phillips and metallocene catalysts are mostly supported on SiO_2. The nearly spherical porous catalysts particles enter the reactor either pristine or pre-polymerized (in polypropylene processes). Monomer molecules must diffuse through the stagnant boundary layer (external resistance) and into the pores (internal resistance) of the catalyst before they reach the active sites where they become part of polymer chains. The nascent polymer molecules fill the catalyst pores, giving rise to compressive stresses that eventually rupture the catalyst particle into thousands of smaller fragments surrounded by the polymer phase. The polymer particle keeps expanding as more polymer is produced, until it eventually exits the polymerization reactor.

From a chemical reaction engineering point of view, each polymer particle can be viewed as a micron-sized semi-batch reactor: monomer, comonomer, hydrogen, and other chemical species diffuse into it, but no product (polymer) leaves the particle. The heat of polymerization is transported from the particle to the bulk phase like in a semi-batch reactor equipped with a cooling jacket. Mathematical models developed to describe this diffusion-reaction process are called Single Particle Models (SPM).[42] In these systems, we should expect mass and heat transfer limitations to generate radial profiles of concentration and temperature in the polymer particle. If the active sites located along the radius of the polymer particle are exposed to distinct concentrations of reagents and temperatures, we should also expect them to make polyolefins with different microstructures. If this happens, the MWD, CCD, CSLD, SRD, RRD, LCB, and R_p become a function of the radial position in the polymer particle.[95] Moreover, since the polymer particle is constantly expanding as more polymer is formed, the severity of the mass and heat transfer resistances also changes with time. Consequently, polymer microstructure and R_p become a function of the age of the particle in the reactor (reactor residence time).[96]-[99]

Heat and mass transfer limitations will always broaden the microstructural distributions of a polyolefin. By how much will depend on the magnitude and duration of these limitations. Regardless, some degree of microstructural broadening may be expected when a polyolefin made

with a supported catalysts is compared to its counterpart made with the same catalyst in a solution polymerization reactor operated under temporal and spatial uniform conditions.

For a long time, two models competed to explain the unexpectedly broad MWDs of polymers made with heterogeneous Ziegler-Natta catalysts: *physical models* relied on mass and heat transfer limitations to explain this broadening, while *chemical models* attributed it to the presence of multiple site types.[7] Today we know that both factors play complementary roles in broadening not only the MWD, but also other microstructural distributions of polyolefins made with supported catalysts. We have already discussed chemical models in the Catalysis level. In this section, we will concentrate on physical models.

Two main mathematical models have been developed to quantify the phenomena happening in the Internal and External Phenomena level: the multigrain model (MGM) and the polymeric flow model (PFM). They are compared in Figure 24.

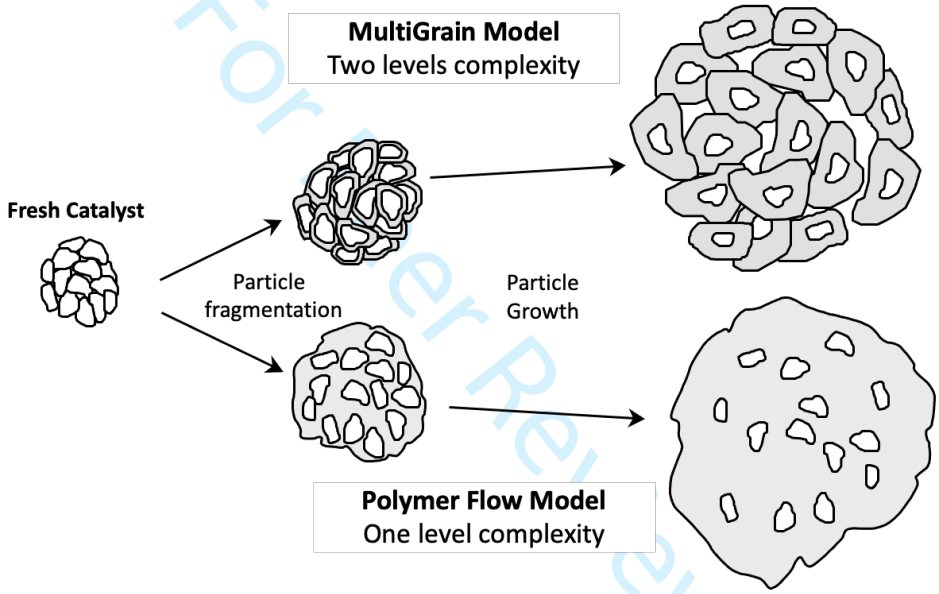

Figure 24 Comparison of the multigrain model (MGM) and the polymeric flow model (PFM).

The MGM assumes that the porous catalyst/polymer particle (*macroparticle* or *primary particle*) is an aggregate of many *microparticles* (*micrograins* or *secondary particles*). The active sites are assumed to be located on the surface of the *non-porous* microparticles.[100],[101] As the polymerization proceeds, the polymer chains envelope the microparticles and cause the macroparticle to expand, while preserving the shape of the original catalyst particle. This *replication phenomenon* is observed experimentally with most supported olefin polymerization catalysts. Since two levels of mass and heat transfer are involved, the MGM requires the solution of two sets of partial differential equations. The PFM, on the other hand, does not distinguish between micro- and macroparticles. Instead, it assumes that the active sites are distributed within a porous, yet continuous polymer phase surrounding the catalyst fragments.[95],[102],[103] The random-pore polymeric flow model (RPPFM) is a variation of the PFM that combines the two levels of diffusion of the MGM in a single effective diffusivity.[104]-[107]

We know from electron microscopy (SEM and TEM) studies that while catalyst particles resemble the MGM description of particle morphology, this changes rapidly as the polymerization starts, the particles fragment and grow by expansion. For this reason the PFM is currently preferred by many authors to the MGM. One might assume that the PFM is less accurate than the MGM, but this is not necessarily true. The PFM condenses the mathematical formulation of the MGM by assuming that the two levels of mass and heat transfer (at the micro- and macroparticles) can be collapsed into a single level. In reality, both models—like any mathematical model—are simplifications of the reality. The real question we must ask is: can they help us understand what happens inside a polymer particle? As polymer reaction engineers, our task is to select the model that best represents the process we are trying to describe with the fewer number of adjustable parameters. We think that the PFM, or the RPPFM, is often a good compromise between accuracy and simplicity. We will restrict our analysis to these two models in the remaining of this section.

We will being our analysis in this section with isothermal polymer particles. This does not mean that intraparticle heat transfer resistances are negligible during olefin polymerization. In fact, it has been shown that they may be considerable, particularly in gas-phase polymerizations, leading to significant radial temperature profiles. However, our main purpose in this overview article is to show how intraparticle transfer phenomena may affect the results of the other modeling scales; for this goal, mass transfer resistances alone are a convenient starting point.

According to the PFM, the concentrations of monomers in the amorphous polymer phase are given as,

$$\frac{\partial[M_{p_i}]}{\partial t} = \frac{1}{r^2}\frac{\partial}{\partial r}\left(r^2 D_{e_i}\frac{\partial[M_{p_i}]}{\partial r}\right) - R_{M_i} \tag{74}$$

The effective diffusivity, D_{e_i}, is a combined effective diffusivity of monomer i in the pores *and* polymer phase surrounding the active sites. In the RPPFM formulation, D_{e_i} is given by the equation,

$$D_{e_i} = \frac{\varepsilon}{{\tau_L}^2} D_{i,m} + (1-\varepsilon)(1+3\varepsilon)D_{p_i} \tag{75}$$

Since both ε and τ_p change with time, so does D_{e_i}. Finally, the initial and boundary conditions are,

$$[M_{p_i}] = [M_{p_i}]_0 \; @ \; t = 0, \forall \, r \tag{76}$$

$$\frac{\partial[M_{p_i}]}{\partial r} = 0 \; @ \; r = 0, \forall \, t \tag{77}$$

$$[M_{p_i}] = [M_{p_i}]_{eq} = f(T, [M_i], [X_i] \ldots .); \; D_{e_i}\frac{\partial[M_i]}{\partial r} = k_s([M_i]_b - [M_i]) \; @ \; r = R_L, \forall \, t \tag{78}$$

If we examine at the factors controlling mass transfer resistances at the particle level, it is interesting to note that the more significant mass transfer effects occur inside the particle, since the arrival of reactive species at the active sites is controlled to a large extent by diffusion through the polymer phase surrounding them.[108] This is reflected in Eq. (75), which defines an effective diffusivity as a combination of diffusion through the amorphous polymer phase and particle pores. The diffusivity through the polymer phase is three to four orders of magnitude lower than that through the particle pores in a gas phase process. This difference amounts to an order of magnitude in slurry phase, but diffusion through the polymer phase is still the rate limiting step. The other important factor in Eq. (75) is the particle porosity; its value effectively defines the characteristic length scale for diffusion in the polymer phase: the lower the porosity, the greater the length scale will become for diffusion through the polymer phase to the active sites. In other words, the internal morphology of the polymer particle affects the rate of mass transfer, and thus the observed rate of polymerization and polymer microstructure. If diffusion occurs primarily through the polymer phase in a particle with low porosity, then mass transfer limitations increase. Contrarily, if diffusion is mostly through the pores of the particle, mass transfer limitations may be negligible.

The factors determining the morphology and the evolution of particle morphology are complex subjects that have been the object of several articles.[42],[109]-[112] We will not dwell on them herein. Suffices to say that, as the particles fragment and expand, factors that impact the dissipation of mechanical energy in the particles—such as the polymerization rate, which generates mechanical stress due to polymer accumulation in the pores, and the rigidity/deformability of the formed polymer, which is responsible for dissipating this stress—affect the internal morphology of the particles.[113]-[116] Currently, no model can predict a priori the internal structure of the polymer particles. This poses a few challenges that must be overcome to model the impact of mass transfer resistances on polymer properties at the level of the polymer particle.

Regardless of these complexities and which SPM we select to describe intraparticle transport resistances, the final result is a radial concentration gradient of monomer, comonomer, hydrogen, and other reagents: the concentrations are higher at the surface of the polymer particle and lower at the center. These gradients are also dynamic: they are steeper at the beginning of the polymerization, because of the higher concentration of active sites, and decrease as the polymerization proceeds because the active sites get diluted in the formed polymer chains. In addition, catalyst site deactivation will also soften the concentration gradients at higher polymerization times. Figure 25 shows how the concentration gradients for ethylene and 1-hexene could look like as a function of time in a polymer particle. The exact shapes, including which concentration profiles are steeper (ethylene or 1-hexene?), depend on how reactive the catalyst is with respect to ethylene and 1-hexene, and on the diffusivities of both monomers in the amorphous polymer phase. The main message here is that the concentrations will decrease from surface to center, and that the radial profiles will become less steep as the polymerization goes on and the polymer particle expands. The most important question is: how do these radial profiles affect the polymer microstructure and the polymerization rate?

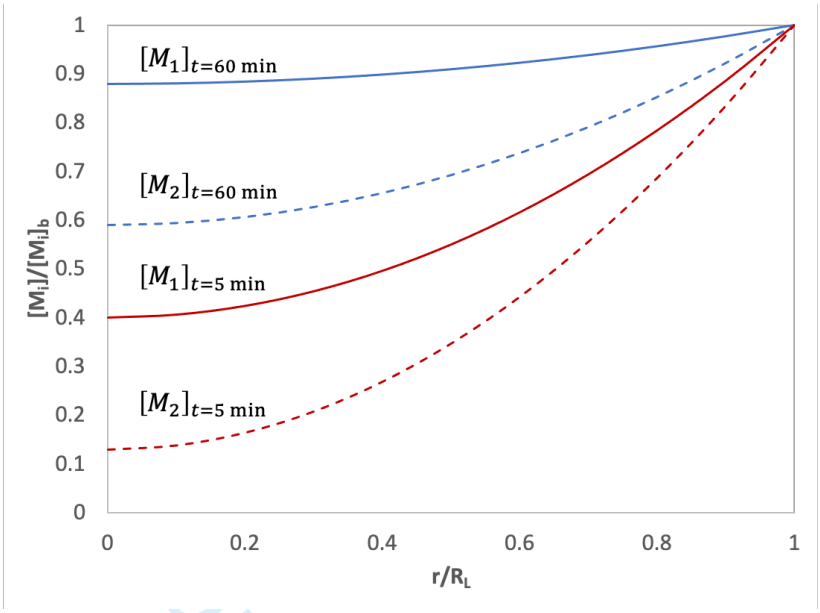

Figure 25 Hypothetical dimensionless ethylene, $[M_1]$, and 1-hexene, $[M_2]$, radial profiles.

Assuming that hydrogen is present as a chain transfer agent and that its concentration is the same across the particle (no concentration gradients), the *local instantaneous* molecular weight averages and chemical compositions of the ethylene/1-hexene copolymer populations made after 5 and 60 minutes at different radii in the polymer are compared in Figure 26. Pay attention to the emphasis on the words *local* and *instantaneous*. These values apply to polymer populations made in a given radial positions (local) at a short time interval (instantaneous).

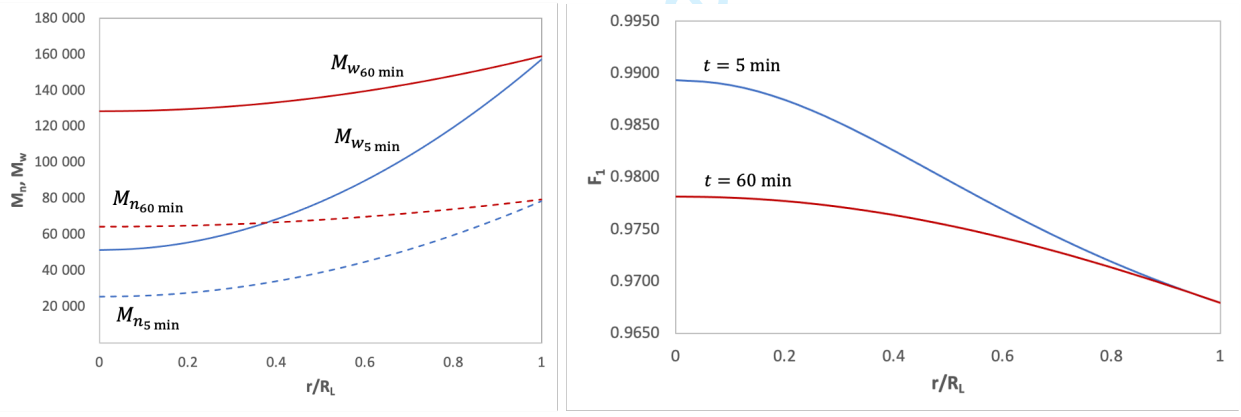

Figure 26 Local instantaneous molecular weight and chemical composition averages as a function of time and particle radius for the concentration gradients shown in Figure 27 assuming a SS supported catalyst. Model parameters: $[M_1]_{r=R_L} = 0.6$ mol·L^{-1}, $[M_2]_{r=R_L} = 0.2$ mol·L^{-1}, $[H_2]_{\forall\, r} = 0.03$ mol $\cdot\, L^{-1}$, $[C_0] = 1 \times 10^{-4}$ mol·L^{-1}, $k_{p_{11}} = 1 \times 10^5$ L·mol^{-1}·s^{-1}, $k_{p_{12}} = 1 \times 10^4$ L·mol^{-1}·s^{-1}, $k_{p_{21}} = 5 \times 10^4$ L·mol^{-1}·s^{-1}, $k_{p_{22}} = 1 \times 10^3$ L·mol^{-1}·s^{-1}, $k_{t_{H_1}} = 1 \times 10^3$ L·mol^{-1}·s^{-1}, $k_{t_{H_2}} = 1 \times 10^3$ L·mol^{-1}·s^{-1}, $k_{t_{\beta_1}} = 1$ s^{-1}, $k_{t_{\beta_2}} = 10$ s^{-1}, $f_a = 0.03$ s^{-1}, $f_d = 1 \times 10^{-4}$ s^{-1}, $R_{L_{t=5\ \text{min}}} = 20$ μm, $R_{L_{t=60\ \text{min}}} = 250$ μm.

The molecular weight and composition averages at 5 and 60 minutes are the same at the surface of the polymer particle, since it is exposed to the same concentrations of ethylene, 1-

hexene, and hydrogen, but differ inside the polymer particle because these concentrations are different, as shown in Figure 25. Both M_n and M_w decrease towards the center of the particle because the overall monomer concentration, $[M_T] = [M_1] + [M_2]$, decreases while the concentration of hydrogen, $[H_2]$, remains constant. The fraction of ethylene in the copolymer, $\bar{F}_1$, increases towards the center of the particle since the 1-hexene concentration profile is steeper than that for ethylene. Including the heat balance would exacerbate these trends, as the higher temperatures in the centre of the particle would also lower M_n and affect $\bar{F}_1$.

The local averages shown in Figure 26 were calculated with the expressions we showed in the Catalysis section: Eq. (12), (13), and (19) for M_n, M_w, and $\bar{F}_1$, respectively. The definition for τ must be changed to account for transfer to hydrogen during this binary copolymerization. The reader should be able to derive it like we did for Eq. (73),

$$\tau = \frac{\left(f_{t_{H_1}} + f_{\beta_1}\right)\phi_1 + \left(f_{t_{H_2}} + f_{\beta_2}\right)\phi_2}{\left(f_{p_{11}} + f_{p_{12}}\right)\phi_1 + \left(f_{p_{21}} + f_{p_{22}}\right)\phi_2} \tag{79}$$

The method of moments is commonly used to calculate these averages.[10],[19],[117] Even though the method of moments is powerful, we prefer the method of instantaneous distributions because it is simpler to use and can describe complete distributions, not only averages, as we have demonstrated above. The complete solution of the population balances leading to the moment equations is another method to obtain complete microstructural distributions,[118] but at a much higher computational cost. We do not recommend it if the instantaneous distributions for the system are known.

It is also interesting to compare the local instantaneous MWDs and CCDs of the polymer populations made at different radii. Figure 27 shows these distributions after 5 minutes of polymerization. We used 30 radial discretization points in these simulations, each associated with an MWD and CCD. It is enlightening, we think, to see how the distributions drift according to the radial positions in which they are made. Since each distribution follows Flory MPD and Stockmayer BD, the instantaneous distribution integrated over all radii must be broader than its individual local components. This is the main argument advocated by the supporters of physical models to explain why the MWD and CCD of polyolefins made with supported catalysts is broader than the predicted with Flory and Stockmayer distributions.

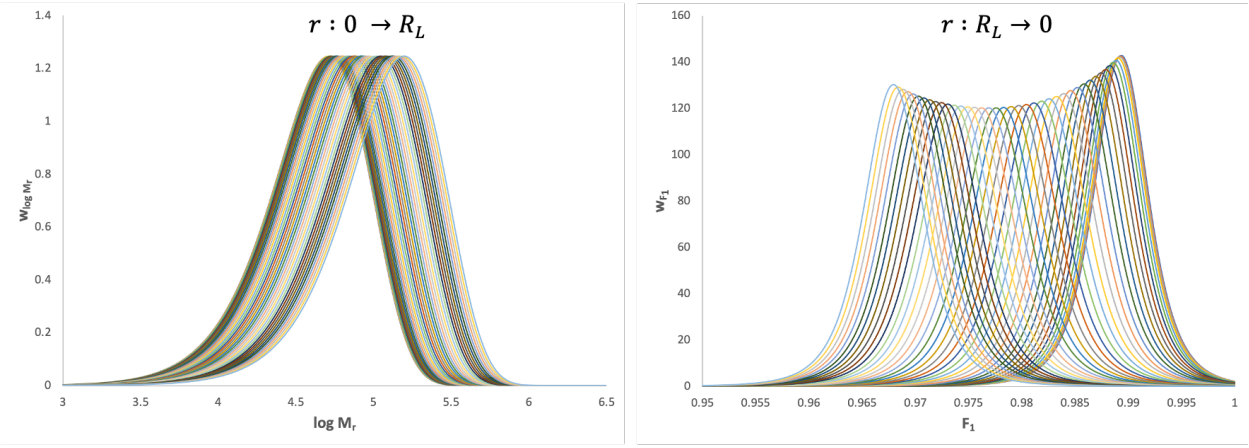

Figure 27 Local instantaneous MWDs and CCDs for the copolymers shown in Figure 28. All distributions are normalized: $\int_0^\infty w_{\log M_r} \mathrm{d}r = \int_0^1 w_{F_1} \mathrm{d}F_1 = 1$.

Before we can perform this integration, we need to multiply each distribution by the mass fraction of polymer made on each radial position, m_{r_i}. These mass fractions are calculated using the rates of polymerizations at each particle radius and the volume of each control element,

$$m_{r_i} = \frac{R_{p_{r_i}} \Delta V_{r_i} \bar{M}_{r_i}}{\sum_{i=0}^{n_r} R_{p_{r_i}} \Delta V_{r_i} \bar{M}_{r_i}} = \frac{\int_{r_i}^{r_{i+1}} R_p(r) \bar{M}(r) r^2 \mathrm{d}r}{\int_0^{R_L} R_p(r) \bar{M}(r) r^2 \mathrm{d}r} \tag{80}$$

where $R_{p_{r_i}}$ is the local rate of polymerization, $\bar{M}_{r_i r_i}$ is the local average molar mass of the copolymer repeating unit, n_r is the number of radial positions in the particle, and ΔV_{r_i} is the volume of the control element,

$$\Delta V_{r_i} = \frac{4}{3}\pi({r_i}^3 - {r_{i+1}}^3) \tag{81}$$

Figure 28 shows how the distributions in Figure 27 look like after these weights are applied to them. Much more polymer is made in the outermost radial positions; therefore, they dominate the molecular architecture of the whole polymer.

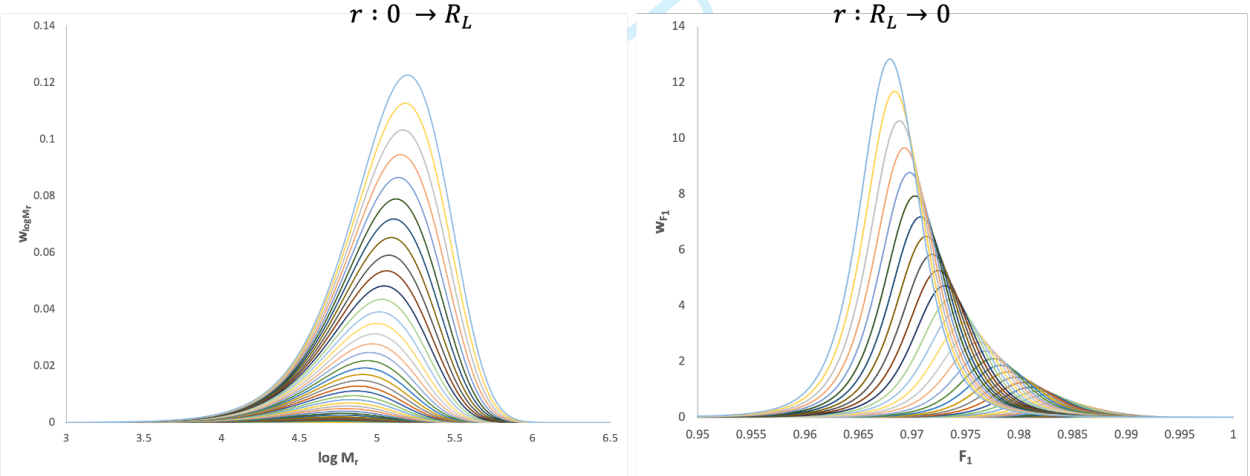

Figure 28 Local instantaneous MWDs and CCDs for the copolymers shown in Figure 27, weighted according to their mass fractions.

We can also inspect how the bivariate MWD-CCD varies within the particle using this approach. Figure 29 illustrates this concept for three different particle radii.

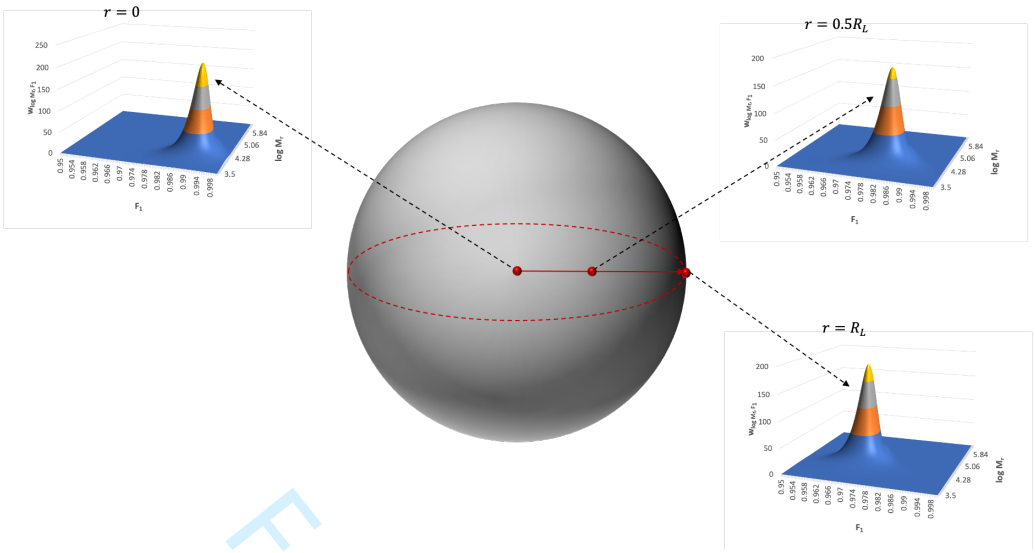

Figure 29 Local instantaneous Stockmayer BD at different particle locations when $t = 5$ min.

Figure 30 shows the instantaneous MWD and CCD for the whole polymer particle at a polymerization time of 5 minutes. For this example, when $t = 5$ min, $M_n = 58\,578$, $M_w = 123\,906$, $PDI = 2.12$, and $\bar{F}_1 = 0.9721$. Interestingly, when $t = 60$ min, $M_n = 73\,798$, $M_w = 148\,041$, $PDI = 2.006$, and $\bar{F}_1 = 0.9715$. The instantaneous average molecular weights increase with time because the concentrations of ethylene and 1-hexene increase and their gradients flatten, which also causes the $PDI \to 2$, indicating that the mass transfer limitations are no longer severe. The copolymer composition, on the other hand, does not vary much with time in this example because the relative concentrations of ethylene to 1-hexene remain practically the same throughout the polymerization.

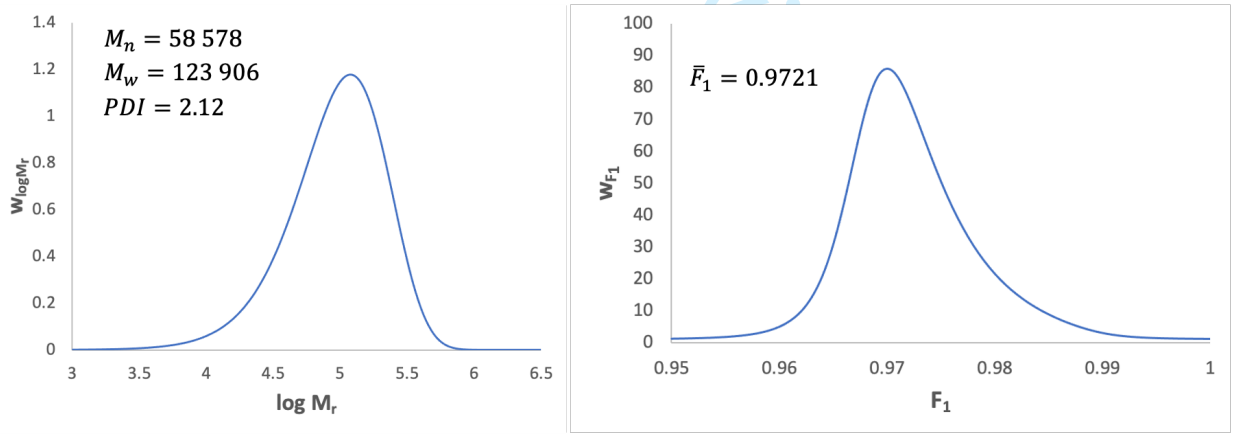

Figure 30 Instantaneous MWDs and CCDs for the copolymers shown in Figure 28, integrated over the whole polymer particle when $t = 5$ min.

It is important to emphasize that these are the distributions produced *at* 5 minutes, not *after* 5 minutes. They were calculated adding all the local distributions shown in Figure 28 using the equations,

$$w_{\log M_r} = \sum_{i=0}^{n_r} m_{r_i} \left(w_{\log M_r}\right)_i \tag{82}$$

$$w_{F_1} = \sum_{i=0}^{n_r} m_{r_i} \left(w_{F_1}\right)_i \tag{83}$$

The cumulative microstructural distributions, obtained after a polymerization time t has elapsed, are calculated in a similar way, by multiplying each instantaneous distribution (for the whole particle) by the mass fraction of polymer made in that particular time interval, Δt, and adding them over all time intervals.

It is also interesting to understand how mass transfer limitations affect the instantaneous rate of polymerization. Since the concentration of ethylene and 1-hexene drop from the surface to the center of the catalyst particle, so will the rate of copolymerization (Figure 31). The rates of copolymerization at both times decrease from the surface to the center of the particle, as expected. When $t = 5$ min, R_p is higher at the surface than when $t = 60$ min because the catalyst sites have not deactivated at the same extent as when $t = 60$ min, but for $r/R_L < 0.8$ the polymerization rates become smaller because the monomer and comonomer concentration profiles are much steeper at short polymerization times. Of course, if the catalyst activated more slowly (build-up type kinetic curves), the results would be substantially different.

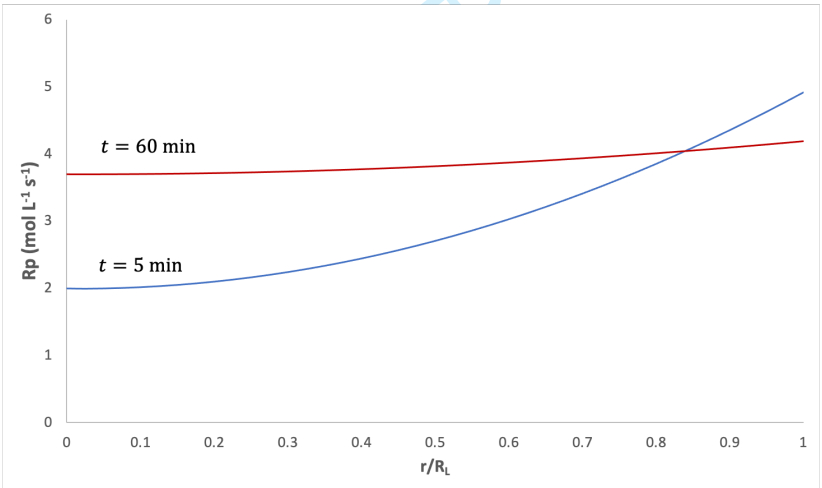

Figure 31 Instantaneous rates of polymerization as a function of radial position in the polymer particle. See Figure 26 for model parameters.

We can calculate the instantaneous effectiveness factor for this model catalyst with the classic reaction engineering equation,

$$\eta = \frac{4\pi \int_0^{R_L} R_{p_r} \bar{M}_r r^2 \mathrm{d}r}{\frac{4}{3}\pi R_L^{\ 3} R_{p_{r=R_L}} \bar{M}_{r=R_L}} \tag{84}$$

For the two polymerization times studied in Figure 31, we would find that $\eta_{t=5\ \mathrm{min}} = 0.74$ and $\eta_{t=60\ \mathrm{min}} = 0.93$, that is, the catalyst becomes more *effective* at higher polymerization times when the nascent polymer has diluted the active sites and reduced mass transfer limitations. This is a typical finding for most supported SS and MS catalysts.

Heat transfer resistances are also hard to model, but for different reasons. Intraparticle heat transfer is reasonably easy to quantify because the effective thermal conductivity of the polymer phase is well known, and the energy flux out of the particle is approximately independent of its morphology. However, as with all model-building exercises, we need to make assumptions about how heat is evacuated from the particles. In the model shown below for the PFM, and in virtually all SMPs in the literature, it is assumed that energy is transferred from the particle only by convective heat transfer, as quantified by the convective heat transfer coefficient, *h*, in Eq. (88). This value of this coefficient must be chosen with care because the particles in the reactor have a distribution of sizes and, most importantly, are not alone in the reactor! Using a simple expression, such as the Ranz-Marshall correlation, will often lead to significant underprediction of the heat flux exiting the particle.[119],[120] This point will be discussed further in the following section.

For the PFM, the energy balance is commonly written as,

$$\rho c_p \frac{\partial T}{\partial t} = \frac{1}{r^2}\frac{\partial}{\partial r}\left(r^2 k_e \frac{\partial T}{\partial r}\right) - \left(-\Delta H_p\right) R_M \tag{85}$$

where ρ, c_p, and k_e are the effective density, heat capacity, and thermal conductivity of the polymer particle, ΔH_p is the overall enthalpy of polymerization, and R_M is the overall local rate of polymerization ($\sum_{i=1}^{N} R_{M_i}$). The initial and boundary conditions for Eq. (85) are,

$$T = T_0 \ @\ t = 0, \forall\ r \tag{86}$$

$$\frac{\partial T}{\partial r} = 0 \ @\ r = 0, \forall\ t \tag{87}$$

$$\rho c_p \frac{\partial T}{\partial r} = h(T_b - T) \ @\ r = R_L, \forall \tag{88}$$

2.5 Particle Interactions

All the SPM discussed in the previous section assume that the polymer particles can be treated independently of each other. This is not realistic, since olefin polymerization reactors are operated at the highest-allowable solids contents to maximize their productivity. Polymer particles are suspended in an inert diluent in slurry processes using mechanical stirrers. In gas-phase reactors, they are either fluidized by the upwards flow of monomers, nitrogen, and hydrogen in fluidized-bed reactors (FBR), or kept afloat in the gas phase under the action of sophisticated stirrers in vertical or horizontal gas-phase stirred reactors.[7] Furthermore, gas phase processes can also contain liquid droplets, in the case of condensed mode operation, or even liquid-rich zones in super-condensed mode.

Because all olefin polymerization processes strive to achieve maximum productivity (or space-time yields), the solids concentration in the diluent or gas-phase is kept at least from 30 to 40% on a volume basis in FBRs and CSTRs, and higher still in loop reactors and stirred gas-phase reactors. The upper solids content limit depends on multiple factors such as heat transfer capacity, fluidization criteria, and medium viscosity. Regardless of the reactor type and polymer particle fluidization/suspension, one thing is certain: the particles do not evolve alone, but rather collide with other particles in the reactor, the reactor walls, other internal fittings, and eventually liquid droplets in some three-phase reactors.

The impact of these interactions is felt at different levels: some might form agglomerates, while others might produce fines; some may impact heat transfer efficiency, while others may cause wall sheeting. The one thing that all of these phenomena have in common is that they are poorly understood on a quantitative level. This level is probably the least understood and conceptually the most difficult to model. Not surprising, it is almost always ignored in most modelling studies!

Particle agglomeration, for instance, may pose a number of problems for reactor operation, as unexpected large particles can lead to defluidization in FBRs, damage pumps in slurry loop reactors, or sediment in slurry autoclave reactors. Large particle agglomerates may also experience severe mass transfer limitations, which reduce the local rate of polymerization and lead to the production of polymer with low molecular weight.[121]

There is more than one cause for agglomeration.[122] Agglomerates can form whenever particles become sticky and collide with enough energy to remain stuck together. Possible sources for increased stickiness include: 1) Particles overheating: if particles overheat due to high rates of polymerization and poor heat removal, the polymer on their surfaces may exceed its softening point; 2) Use of condensing agents in gas phase reactors: Running a gas phase reactor in condensed mode requires the use of induced condensing agents (ICA) such as iso-butane or iso-pentane. In addition enhancing heat removal from the reactor, ICAs also plasticize the polymer and make it stickier. Moreover, they may also lower the effective melting point of the polymer, making it stickier at a lower temperature, as illustrated in Figure 32 for the DSC melting curves of a sample of dry HDPE and the same HDPE mixed with 20 wt.% of n-hexane; 3) Softening of particles in slurry reactors (eventually combined with overheating): Different diluents (iso-butane versus hexane for polyethylene) may alter the physical properties of the polymer and increase stickiness, particularly for high MFI, highly amorphous materials; 4) Production of soft polymer: LLDPE with high α-olefin content or ethylene-propylene rubber in high impact polypropylene processes are inherently sticky and are known to produce agglomerates.

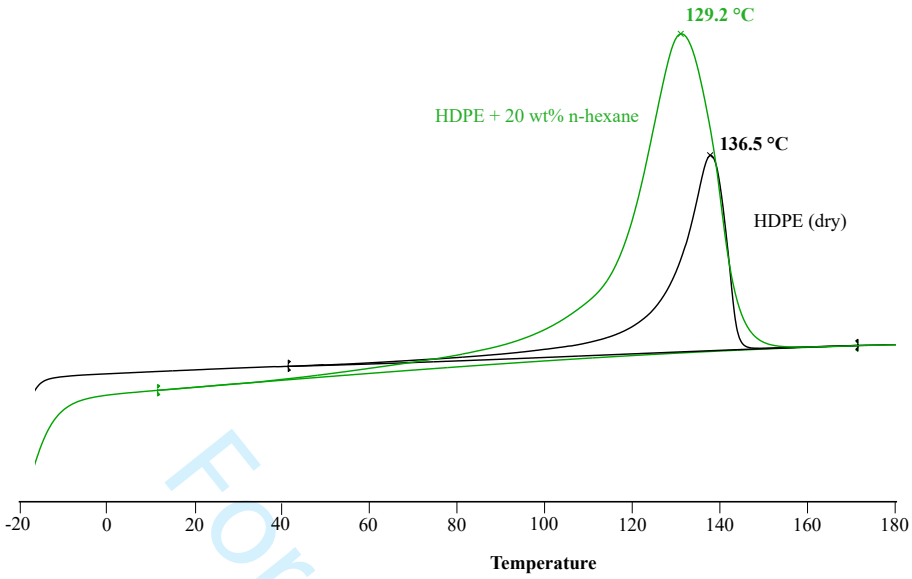

Figure 32 Melting point curves of a sample of dry HDPE and the same HDPE with 20 weight percent n-hexane. Both the melting temperature and the melt onset of the same with n-hexane are significantly lower, and one expects the polymer to be much stickier.

Other reasons for particle agglomeration include electrostatic[123] interactions and liquid bridging in gas phase reactors. If one considers all the causes for particle agglomeration, it becomes apparent why developing a quantitative model to quantify agglomeration process is so challenging. It is generally accepted that particle agglomeration is a two-body problem, with the rate of agglomeration being proportional to size of each particle in the collision and the probability that the collision will result in the formation of a larger, distinct agglomerate. Developing an expression for the probability of a given outcome from a collision is currently beyond the state-of-art understanding. For one thing, our ability to quantify the stickiness of a particle is limited. Even if one could, the collision energy between two otherwise identical pairs of particles is not constant in a reactor, since the particles move at distinct velocities in different zones of the reactor. Temperature gradients in the reactor could also lead to different levels of stickiness for a given particle depending on where it is located.

Mathematically, the probability that a given collision may form an agglomerate is expressed with an agglomeration kernel constant, K_{ag}, and the expression that defines the rate of agglomeration, $R_{ag}(d_i, d_j)$, of two particles with diameters d_i and d_j as a function of the number of agglomerates formed per unit volume of the reactor per unit time is given by,

$$R_{ag}(d_i, d_j) = K_{ag}(d_i, d_j)\, n_i n_j \tag{89}$$

where n_i and n_i are the number of particles of diameters d_i and d_j respectively. The group of Kiparissides proposed linking the expression for K_{ag} to an average temperature of the colliding particles, but settled for an empirical expression that favored the agglomeration of small particles between themselves.[124] The agglomeration kernel is often an empirically adjusted constant.[125] The difficulties of trying to develop an expression for K_{ag} are easy to imagine given the multiplicity of complex physical processes that it describes. Despite the fact that particle agglomeration can severely affect reactor operation, especially for FBRs, energy-conserving engineers often simply neglect this term in their reactor models.[124]

It should also be noted that if particle-particle collisions do not form agglomerates, they may have the opposite effect and generate fines. If particles have irregular shapes, such as protrusions or flaky outer layers, collisions could lead some of these protuberances to breaking off from the main particles. One way to prevent this from happening is to raise the reactor temperature, causing the polymer to become less brittle and more ductile.[127] This allows the parts of the particle that might break off at lower temperature to flex and/or bend, and to remain attached to the main particle.

In a different vein, particle-particle interactions can also influence heat transfer in ways that are difficult to accurately quantify. As heat transfer issues are of primary importance for gas-phase reactors, most of the work done to understand how heat is removed from the polymerizing particles has been done for gas phase reactors. The SPM energy balance described in Eq. (85) to (88) assumes that the heat of polymerization is transferred through the particles by conduction, and then through the particle boundary layer by convection. The rate of heat removal at the particle surface is determined by the convective heat transfer coefficient, h, as shown in Eq. (88), which is usually estimated using empirical correlations. One of the first models of this type for the simulation of particle to fluid heat transfer is the Ranz-Marshall correlation,[127]

$$Nu = \frac{hd_p}{k_g} = 2 + 0.6\left(\frac{d_p\rho_g u}{\mu_g}\right)^{0.5}\left(\frac{\mu_g C_{p_g}}{k_g}\right)^{0.33} \tag{90}$$

where Nu is the Nusselt number, d_p is the particle diameter, u is the relative fluid-particle velocity, and ρ_g, μ_g, k_g, and C_{p_g} are the density, viscosity, thermal conductivity, and heat capacity of the fluid. This type of correlation, developed for the evaporation of droplets, is adequate for isolated particles. However, it has been shown that while this correlation is sufficient for low concentration systems,[119],[120] it is necessary to account for particle-particle interactions at solid levels more coherent with commercial operation conditions. These interactions can take the form of larger particles shielding smaller ones from the flowing gas that change the local convective heat transfer conditions.[128],[129] Physical interactions between large and small particles, even for short periods of time, can cool down small active particles via conductive heat transfer by contacting them with larger ones.

Take, for example, the computational fluid dynamic simulations in Figure 33, which illustrates the impact of contacting particles of different sizes oriented in different gas flows. All particles were simulated as polymer particles having grown for different times from the same catalyst particles. The small particles are the same size in all four images. Since the simulation

assumed that the catalyst did not deactivate, the total rate of heat production per particle was identical but the heat generation rate per unit surface (or volume) changed. For 80 and 150 μm particles (Figure 33.a-b), the temperature at the centers of the small particles were a function of the direction of gas flow: less heat was removed when they were shielded by the larger particles and, consequently, the particles heated up. We can also see that the hottest spot in the small particles moves from a location near the trailing edge of the particle when the flow is right-to-left, and somewhere near the point of contact in the other case. Several differences appear when comparing Figure 33.c-d to the previous ones. First, the temperature profile of either particle are similar, regardless of the flow direction. Since regardless of the flow direction, most of the surface of the large particle is exposed to the gas the heat transfer from this particle is similar in both cases. The small particle is always inside the inertial boundary layer of the large particle and, consequently its temperature is not effected by the flow direction either. On the other hand, the heat flux from the larger particle is 2.8 times lower than that from the 150 μm particle in Figure 33.a-b. It is, therefore, easier to cool despite generating the same amount of heat as the other particles. Despite being the same in all four simulations, the small particle is much cooler in Figure 33.c and 33.d because convective heat transfer to the cooler large particle is the dominant mechanism of heat transfer.

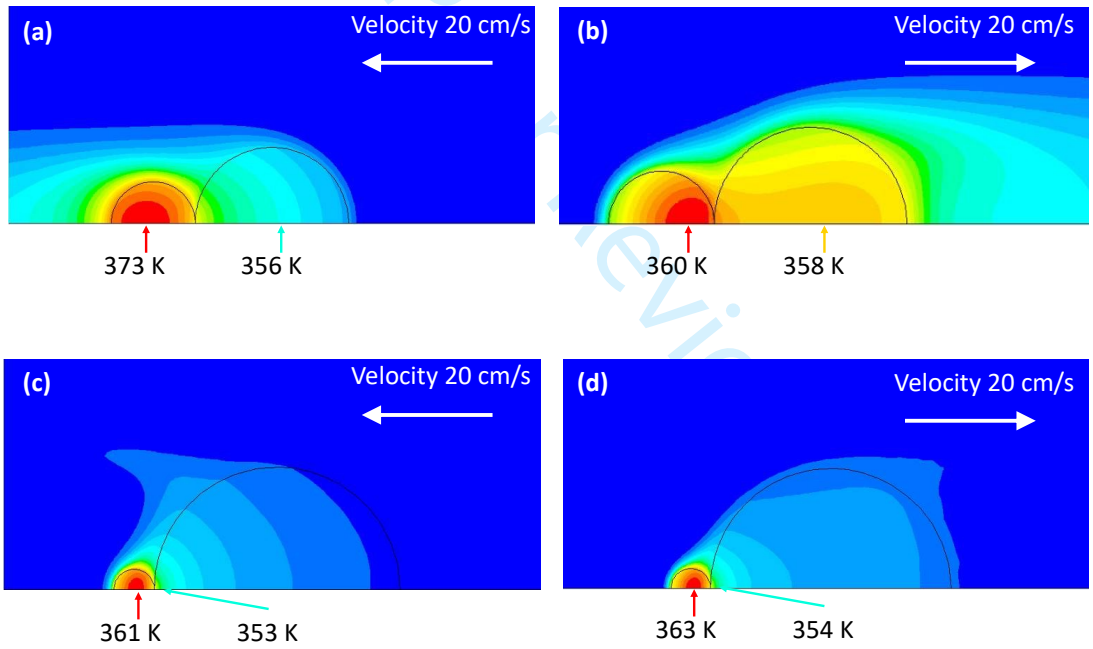

Figure 33 Computation fluid dynamic simulations of polymerizing particles of polyethylene in a gas streams. Free stream velocity 20 cm/s for all images. The flow is from right to left in (a) and (c), and from left to right in (b) and (d). Images (a) and (b): large particle diameter 150 μm, small particle diameter 80 μm. Images (c) and (d): Large particle diameter 500 μm, small particle diameter 80 μm. All polymer particles began as catalyst particles of the same size (30 μm) and same average activities. For other simulation details, see reference.[130]

Simplified simulations such as these are useful to explore isolated (idealistic) cases of heat transfer, but the complexity of all possible particle-particle interactions makes it difficult to describe heat transfer with a single correlation. What seems clear from these simple simulations is

that these different temperature profiles would affect the phenomena taking place at the all the other modeling levels we described above.

Interactions between particles and the reactor wall (or other metal surfaces) can often cause significant problems in a polymerization reactor. Electrically charged particles, for instance, created if polymerizing particles break up into fines, can lead to reactor wall sheeting in FBRs. If a particle carries a charge, it can be attracted to a metallic surface. Once there, it can attract particles of the opposite charge, initiating a sequence of electrostatic agglomeration events. Once the surface is covered with polymerizing particles, the local heat transfer coefficients decrease, causing the particle to overheat and the polymer to become sticky, which will lead to further agglomeration.

The physical complexity of the different interactions we discussed above is such that developing robust process models to integrate them into a multilevel approach is daunting. It is possible that certain aspects of these interactions will one day be describable with computational fluid dynamic models, for instance collision frequency and energy levels, particle interactions with local flow fields, and local rates of heat transfer between the different phases in the reactor, but we are certainly not there yet. Significant fundamental work remains to be done at this level, firstly to improve our scientific understanding of the potential interactions in the reactor, and secondly to develop verifiable mathematical models to quantify them.

2.6 Reactor Fluid Dynamics

This scale is the perhaps the most difficult to investigate. Perhaps for this reason it is often neglected in polyolefin reaction engineering studies. After all, one can use simple representations of the reactor to predict reactor behaviour at a certain level. For instance, Alves et al.[131] modeled the impact of changing levels of induced condensing agents on the productivity and average residence time of a commercial scale FBR with a model that treated the FBR as an ideal CSTR. Other modeling approaches, such compartmentalized reactor models, can be used to investigate temperature and concentration profiles; combining polymerization kinetic models and single particle models with population balances allows us to explore the relationship between reactor operation conditions and polymer microstructure. These models can be used to relate events that occur at the macro- and micro-scales[132] However, they rely on time-averaged properties and, at the current time, none allows for randomly occurring events or meso-scale phenomena that can lead to loss of bed stability. Furthermore, no existing models include particle-particle interactions. Zoning (that is, representing the reactor as a series of interconnected stirred tanks, each with different states and/or phases) is somewhat arbitrary and based on FBR models from the 1970s. If we wish to obtain a detailed picture of what is happening in the reactor and understand how and why events such as local defluidisation, flow segregation, etc. can happen, we need far more detailed models of the flow in the reactor itself.

It is widely accepted that, when properly done, CFD modeling can provide significant insight into the hydrodynamics and macroscale phenomena in FBRs. Numerical modeling of processes at laboratory, pilot and industrial scales by N-Euler CFD modeling approaches (such as NEPTUNE_CFD) are becoming powerful tools to support optimization or scaling-up of polymerization processes[133]-[136] and the development of new processes based on innovative concepts.[137] Despite the usefulness of such models, there are clear limitations with respect to the correct description of the hydrodynamics (mixing and segregation of solids) of multiphase flows, and the proper modeling of reactor hydrodynamics is still in its infancy.

A recent review on modeling of gas phase reactors for ethylene polymerization made it clear that the models that one finds in the literature are necessarily simplified because otherwise they cannot be solved in a reasonable timeframe.[125] These investigations have assumed simplistic polymerization kinetics, ignored intraparticle mass and heat transfer effects, and as rule did not try to predict the effect of reactor fluid dynamics, and heat and mass transfer effects on the microstructure of polyolefins, the structure of the polymer particles, and how the particles interact in the reactor.

Traditionally, for CFD-based modeling of large scale gas phase polymerization reactors, full Eulerian (two-fluid or multi-fluid) models based on the Kinetic Theory of Granular Flows have been used to study (all assuming uniform particle size): gas bubbles behaviour and solids mixing[138], pressure effects,[139] bed size effects,[140] and heat production in the solid phase.[141] In addition mixing and segregation of particles[142]-[144] has been studied using multi-fluid models allowing the incorporation of multiple solid phases.

Furthermore, CFD modeling requires validation and fundamental information that we do not yet possess to capture the realities of industrial processes. Except for solution processes, the vast majority of polyolefin processes employing coordination catalysts are multiphase systems. As we discussed in the previous section, we have a very difficult time trying to model particle-particle interactions, which are obviously important in such systems. In a solution process we are dealing with only one phase, and while the fluid is a very viscous non-Newtonian mixture, it is within reach of current understanding (and computational power) to model the hydrodynamics here.

The experimental challenges to CFD model validation are imposing. In particular, reactor hydrodynamics are scale-dependent. It is extremely difficult to reproduce the fluid flows that we encounter at the commercial scale on a pilot or laboratory scale, as well as very challenging and expensive to do so at the pressures, temperatures and viscosities found in real reactors. It might be possible to validate CFD simulations on small scale reactors, and then extrapolate to larger systems, but this still means validating flow fields in reactors operating at pressures above ambient (making the use of steel reactors mandatory and rendering it difficult to visualize the flows).

2.7 Reactor Residence Time Distribution

The reactor residence time distribution (RTD) is the outmost level in the hierarchical scheme proposed in Figure 2. Since the RTD level can be predicted using the methods in the CFD level, it may be argued that it should not be classified separately from it. We disagree with this hypothetical objection. The models in the RTD level are simpler and easier to apply than those in the CFD level. Consequently, they have been combined with models in other level more often than those in the CFD level.

Industrial reactor technologies for the production of polyolefins vary substantially (stirred vertical and horizontal autoclaves, loop reactors, fluidized beds, multizone reactors), but they are mostly operated at steady-state (except in grade transitions, and shut-down and start-up operations) and the catalyst/polymer particles follow an RTD that approximates that of an ideal continuous stirred tank reactor (CSTR). In contrast, during the development of new catalysts and products, lab-scale autoclave reactors are generally operated in semi-batch or batch mode. CSTRs and batch/semi-batch reactors have drastically different RTDs.[145] Figure 34 compares the RTDs of polymer particles in an ideal CSTR and in a batch/semi-batch reactor with the same average residence time. While the polymer particles stay different times in a CSTR, they remain exactly

the same time in a batch/semi-batch autoclave reactor. If we do not account for this difference, we should not be surprised when a lab-developed catalyst performs differently in an industrial reactor. The consequences of these RTD differences should be clear from some of the examples discussed above. For instance, Figure 17 showed that the MWD-CCD of a polyolefin made with a dual-site catalyst depended on time. Likewise, radial concentration profiles of ethylene and 1-hexene were also time dependant (Figure 27), making M_n, M_w, and $\bar{F}_1$ to change with time (Figure 26).

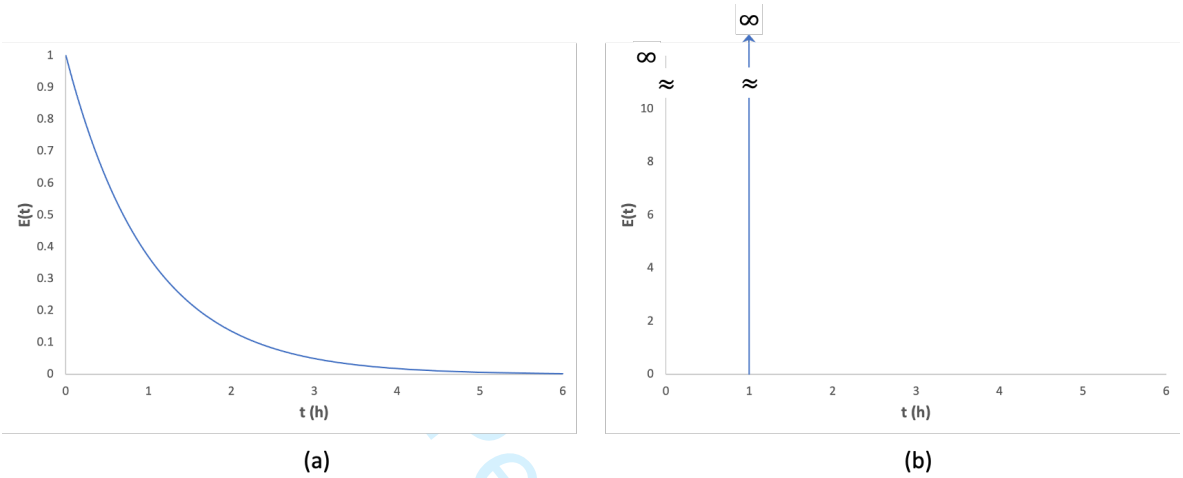

Figure 34 Reactor RTDs for polymer particles in: a) ideal CSTR, b) batch or semi-batch reactor. The average residence time in the CSTR is 1 h. The residence time in the batch/semi-batch reactor is also 1 h.

The effect of RTD on polymer particle size distribution (PSD) has been modelled with different degrees of sophistication. Most of these models used population balances to describe how the RTD (ideal, non-ideal, or empirical) of a single or of a series of reactors influenced the PSD of the resulting polymer, the fractions of polymer made on different reactors in the series (for the case of heterophasic or bimodal reactor blends) or, in some cases, intraparticle mass and heat transfer resistances.[146]-[163] Because population balances require the solution of simultaneous differential-integral equations, it may become cumbersome to handle complex polymerization kinetics, catalyst particle non-uniformities, reactor RTDs or catalyst PSDs of unusual shapes, and inter- and intraparticle mass and heat transfer effects. A more generic approach, relying on Monte Carlo simulation, was proposed recently.[96]-[99] We will use this technique to illustrate the effect of RTD on the previous modeling scales. Besides being the most powerful method developed so far to describe the RTD level, it is also the easiest to comprehend. It also allows us to introduce the concept of Monte Carlo simulation—not discussed anywhere else in this overview paper—that has been gaining renewed interest in polymerization reaction engineering.[44]

Monte Carlo methods use randomly generated numbers to select one event among a set of possible events. Let's introduce this concept by selecting how long a polymer particle will stay in an ideal CSTR. The set of events, in this case, is all the allowable times a polymer particle may stay in a CSTR. The RTD of an ideal CSTR is given by the classic equation,

$$E(t) = \frac{1}{\tau_R} \exp\left(-\frac{t}{\tau_R}\right) \tag{91}$$

where $E(t)$ is the probability density function for the RTD and τ_R is the average residence time in the CSTR. Figure 34.a was generated with Eq. (91) setting $\tau_R = 1$ h. The cumulative distribution associated with Eq. (91) is,

$$F(t) = \int_0^{t_p} E(t)\mathrm{d}t = 1 - \exp\left(-\frac{t_p}{\tau_R}\right) \tag{92}$$

Figure 35 shows $E(t)$ and $F(t)$ for an ideal CSTR with $\tau_R = 1$ h.

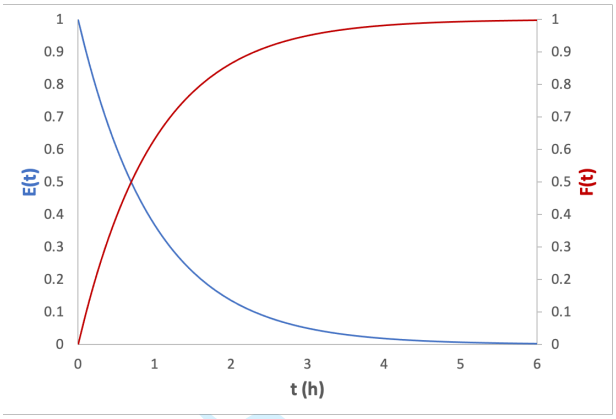

Figure 35 $E(t)$ and $F(t)$ for an ideal CSTR with $\tau_R = 1$ h.

We will now use the cumulative distribution in Figure 35 to randomly select the time a catalyst particle (also randomly selected, as we will show later) stays in the reactor. We accomplish this by generating a random number between 0 and 1. Since we know the analytical solution for the cumulative distribution $F(t)$ (which is convenient, but not necessary, to use this method), it is straightforward to calculate this time by setting $F(t) = \mathrm{RND}$ and then solving for t_p,

$$t_p = -\tau_R \ln(1 - \mathrm{RND}) \tag{93}$$

where $\mathrm{RND} \in [0,1]$ is the randomly generated number. Figure 36 illustrates this procedure assuming that $\mathrm{RND} = 0.5770$. In this case, $t_p = 0.8603$ h.

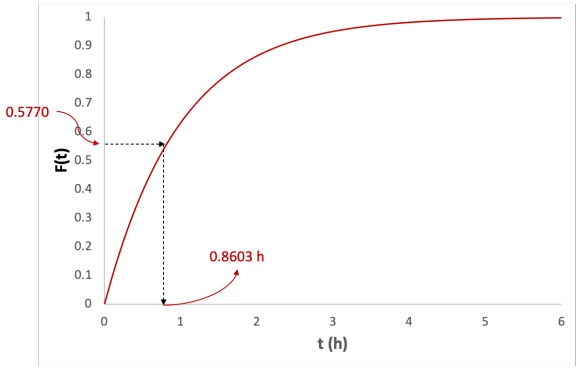

Figure 36 Selecting the value for t_p for $\mathrm{RND} = 0.5770$ ($t_p = 0.8603$ h, $\tau_R = 1$ h).

We can now use this randomly-selected polymerization time to calculate the polymerization rates and yields (Polymerization Kinetics level), radial intraparticle mass and temperature profiles (Particle Transport Phenomena level), and polymer microstructure (Catalysis level).

We must also know the size of the catalyst particle entering the reactor to model interparticle transport phenomena. Most publications using SPMs use the average diameter of the catalyst PSD for these calculations. The Monte Carlo approach, on the other hand, can conveniently handle catalyst particles of different sizes.[99] The procedure to select the catalyst diameter is the same we used to choose the polymerization time: Calculate the cumulative PSD for the catalyst and use a random number to select a diameter. This process is illustrated in Figure 37 for a catalyst that follows a log-normal distribution with average $\overline{d_p} = 20$ μm and $\sigma = 12.7$ μm. If RND = 0.7993, then $d_p = 24.6$ μm.

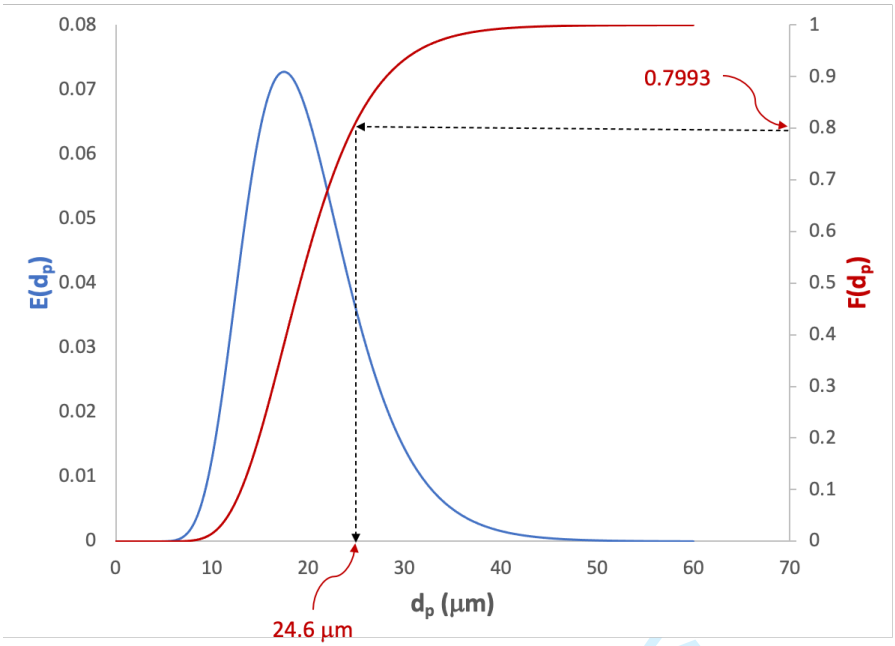

Figure 37 Selecting the value for d_p for RND = 0.7993 ($d_p = 24.6$ μm) for a catalysts with a PSD having $\overline{d_p} = 20$ μm and $\sigma = 12.7$ μm.

Let's illustrate how this process works by randomly selecting 3 catalysts particles from the PSD in Figure 37 and their respective reactor residence times from Figure 36. The random numbers, catalyst diameters, and polymerization times are listed in Table 4. We will assume this is a supported dual-site catalyst with the reaction frequencies shown in Figure 16 and $[C_0]_1 = [C_0]_2 = 1 \times 10^{-4}$ mol·L^{-1} (initial concentrations of active sites in the catalyst particles).

Table 4 Random numbers, catalyst diameters and volumes, and reactor residence times.

#	RND	d_{p_0} (μm)	V_{p_0} (cm^3)	RND	t_p (h)	d_p @ t_p (μm)
C_1	0.7210	22.8	6.206×10^{-9}	0.5798	0.867	274.3
C_2	0.0601	12.0	9.048×10^{-10}	0.2686	0.313	111.5
C_3	0.2485	15.6	1.988×10^{-9}	0.8745	2.075	214.8

To simplify the calculations, we will assume that mass and heat transfer resistances in the particles are negligible. The polymer yield for each particle is calculated with a modified version of Eq. (42), by replacing V_R, the reactor volume, with V_{p_0}, the initial volume of the particle,

$$Y_{p_T} = \sum_{i=1}^{n} R_{p_i} = \bar{M}[C_0]_T V_{p_0} \sum_{i=1}^{n} x_i \frac{\hat{f}_{p_i}}{1 - f_{d_i}/f_{a_i}} \left[\frac{1 - \exp(-f_{d_i} t_p)}{f_{d_i}} - \frac{1 - \exp(-f_{a_i} t_p)}{f_{a_i}} \right] \quad (94)$$

where $n = 2$ for the dual site catalyst.

The first variable we can calculate is the diameter of the polymer particle exiting the reactor after a residence time t_p. The volume of a sphere is given by,

$$V_p = \frac{1}{6} \pi {d_p}^3 \quad (95)$$

If we assume that the volume of the catalyst fragments is negligible compared to the volume of the polymer in the particle, we can also write,

$$V_p = \frac{Y_{p_T}}{\rho_p} \quad (96)$$

where ρ_p is the density of the semi-crystalline (amorphous phase + crystallites) polymer phase.

Therefore, the time-dependent diameter of the polymer particle leaving the reactor can be calculated with the equation,

$$d_p(t_p) = \sqrt[3]{\frac{6 Y_{p_T}(t_p)}{\pi \rho_p}} \quad (97)$$

The yields per particle and final diameters of the three randomly sampled particles are also listed in Table 4. Catalysts particles that stay different times in the reactor form polymer particles of different diameters. Figure 38 illustrates this procedure.

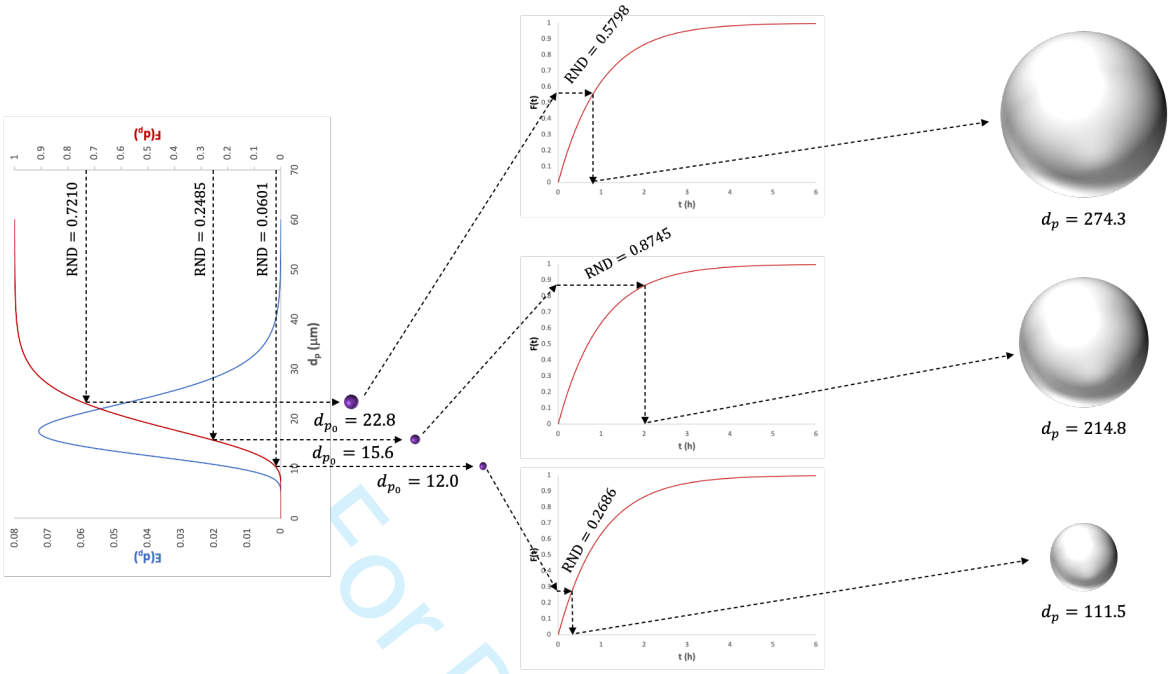

Figure 38 Graphical representation of the process used to generate the results in Table 4.

Since the two site types in this catalyst activate and deactivate at different rates, and also make polymer populations with different molecular weight and chemical composition averages, we should expect that their MWD-CCD will also be a function of reactor residence time (see Figure 16 and 17). Figure 39 shows that the simulations confirm our expectations.

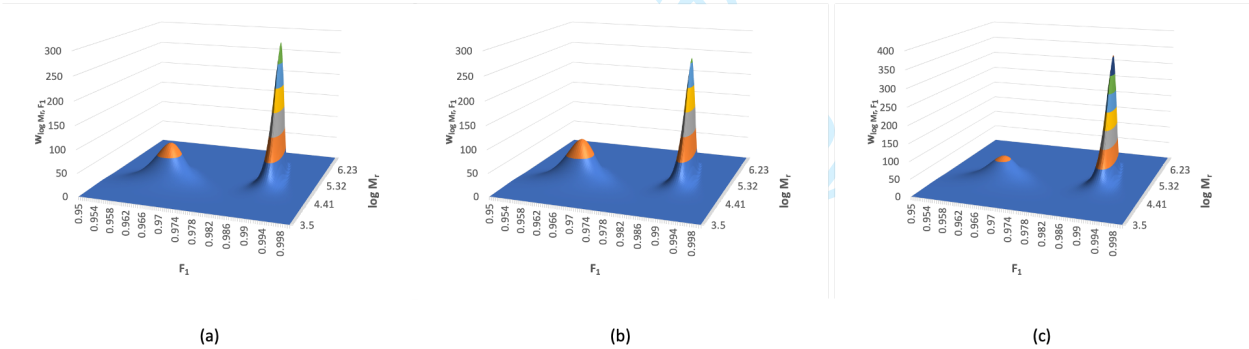

Figure 39 MWD-CCD for the polymer particles represented in Figure 38: a) $t_p = 0.867$ h, $M_n = 71\,205$, $\bar{F}_1 = 0.9778$, b) $t_p = 0.313$ h, $M_n = 65\,902$, $\bar{F}_1 = 0.9764$, c) $t_p = 2.075$ h, $M_n = 76\,231$, $\bar{F}_1 = 0.9790$.

This simulation must be repeated for a large number of catalyst particles to calculate the properties for a representative sample of the polymer particle population.

In the simulations above, we only combined three levels—Catalysis, Polymerization Rate, and RTD—but other levels in Figure 2 could be considered, such as the Internal and External Transfer Phenomena[96] and the Thermodynamic Equilibrium[94] levels. This Monte Carlo approach has been used to calculate the effect of RTD on the PSD of particles made in a single or

in a series of reactors,[99] on the polymer fluff packing density,[98] and on the MWD-CCD of polymers made in a series of reactors.[96],[97]

3 Conclusions

We tasked ourselves with an ambitious goal when we decided to write this overview paper: to cover all levels of mathematical modeling needed to describe olefin polymerization with coordination catalysts, from the active site all the way to the macroscopic phenomena taking place in the polymerization reactor. Our choice of seven modeling levels may be considered idiosyncratic, as most choices in mathematical modeling tend to be, but we would like to argue that these levels effectively compartmentalize the relevant physical and chemical phenomena according to the scales they describe (micro, meso, and macro) *and* the mathematical models they use. Breaking down the multiscale problem of olefin polymerization into these levels is, in our opinion, a powerful way to deal with these convoluted mathematical modeling problems.

When it comes to developing or using a model, a common question is "how complex should the model be?" An equally common answer is "as complex as needed." This answer does not help anyone because often who is asking the question does not know how complex the model needs to be to meet its objectives. Frankly, often neither do we. Perhaps classifying the relevant phenomena in different levels and evaluating how each level affects the outcomes of the simulations is a good way to start answering this pesky question. If we only need to predict polymer yields and average properties under a relatively narrow range of conditions, a simple model using apparent kinetic constant rates at the Catalyst and Polymerization Kinetics levels may suffice. If, on the other hand, we need to describe a wider range of polymerization conditions in the presence of varying concentrations of inert condensing agents in a fluidized bed reactor, we may need to include additional models at the levels of Thermodynamic Equilibrium and Particle Transport Phenomena. Or, if our focus is more at the macroscopic scale and our focus is to understand how the size distribution of the polymer particles evolve in a polymerization reactor, we may be able to work with very simple models at the Polymerization Kinetics level and focus our efforts on developing more sophisticated models at the Reactor Residence Time level. The ability to add and subtract models in different levels is, arguably, the most important advantage of this Divide-and-Conquer multilevel approach.

In this overview we showed that much is known about some of these modeling levels, such as Catalysis and Polymerization Kinetics, for instance, but pitifully little in some others, such as Particle Interactions and Reactor Fluid Dynamics. Much still remains to be done even at the levels in which we are more confident, while some other levels still remain as *terra incognita*. Instead of being discouraged, this is the reason that keeps us, researchers in polyolefin reaction engineering, so engaged with this field. Even after several decades of impressive commercial success, polyolefins still remain an intriguing research area with many unanswered questions. Progress in faster computer processors, more efficient algorithms, and new mathematical modeling tools will keep allowing us to increase the depth of the models at each level, and to integrate more and more levels in our simulation programs to quantify all relevant aspects of olefin polymerization with coordination catalysts.

Nomenclature

Acronyms

BD	Bivariate distribution
^{13}C NMR	Carbon-13 nuclear magnetic resonance
CCD	Chemical composition distribution
CEF	Crystallization elution fractionation
CFD	Computational fluid dynamics
CLD	Chain length distribution
CRYSTAF	Crystallization analysis fractionation
CSLD	Comonomer sequence length distribution
CSTR	Continuous stirred-tank reactor
EPDM	Ethylene/propylene/diene monomer terpolymer
FBR	Fluidized bed reactor
GPC	Gel permeation chromatography
HT-TGIC	High-temperature thermal gradient interaction chromatography
ICA	Induced condensing agent
LCB	Long chain branch(ing)
LDPE	Low density polyethylene
LLDPE	Linear low density polyethylene
MGM	Multigrain model
MPD	Most probable distribution
MS	Multiple-site-type catalyst
MWD	Molecular weight distribution
PC-SAFT	Perturbed-chain statistical association fluid theory equations of state
PFM	Polymeric flow model
PSD	Particle size distribution
RND	Randomly generated number, $\in [0.1]$
RPPFM	Random-pore polymeric flow model
RRD	Regioregularity distribution
RTD	Residence time distribution
SEM	Scanning electron microscopy

SPM	Single particle model
SRD	Stereoregularity distribution
SS	Single-site-type catalyst
TEM	Transmission scanning microscopy
TREF	Temperature rising elution fractionation

Symbols

Al	Cocatalyst
$[Al]_s$	Cocatalyst concentration at the active site, mol·L^{-1}
C	Catalyst precursor site
$[C_0]$	Concentration of active sites at $t = 0$, mol·L^{-1}
$[C_0]_T$	Total concentration of active sites at $t = 0$, mol·L^{-1}, for an MS catalyst.
C_d	Deactivated site
C_{p_g}	Heat capacity of the fluid, Eq. (90)
C_p	Heat capacity of the polymer particle
D_{e_i}	Effective diffusivity of monomer type *i* in the polymer particle, cm^2·s, Eq. (75)
$D_{i,m}$	Molecular diffusivity of monomer *i* in the mixture inside the pores of a polymer particle, cm^2·s
d_p	Catalyst/polymer particle diameter
$\overline{d_p}$	Average catalyst/polymer particle diameter
d_{p_0}	Initial catalyst diameter
D_{p_i}	Diffusivity of monomer type *i* in the amorphous polymer phase, cm^2·s
D_r	Dead chain with *r* monomeric units
$E(t)$	Probability density function for reactor residence time distribution, Eq. (91)
$F(t)$	Cumulative reactor residence time distribution, Eq. (93)
f_a	Site activation frequency, s^{-1}, Eq. (39)
f_d	Site deactivation frequency, s^{-1}, Eq. (40)
f_i	Molar fraction of comonomer type *i* at the active site
f_{i_H}	Frequency of monomer insertion in metal-hydride sites
F_i	Molar fraction of comonomer type 1 in the copolymer
$\bar{F}_i$	Average molar fraction of comonomer type *i* in copolymer made with a SS catalyst

$\bar{\bar{F}}_i$	Average molar fraction of comonomer type *i* in a copolymer made with a MS catalyst, Eq. (23)
$\bar{F}_{ijk}$	Molar fraction of the triad with comonomer sequence *ijk*, Eq. (25) to (26)
$\bar{\bar{F}}_{ijk}$	Molar fraction of the triad with comonomer sequence *ijk*, MS catalyst, Eq. (35)
f_p	Propagation frequency, s^{-1}, Eq. (3)
$\tilde{f}_p$	Lumped propagation frequency, s^{-1}, Eq. (55)
f_{p_g}	Propagation frequency based on the concentration of monomer in the gas phase, Eq. (67)
$f_{p_{12,21}}$	Frequency of 2-1 insertions on 1-2 terminated sites
$f_{p_{21,12}}$	Frequency of 1-2 insertions on 2-1 terminated sites
$f_{p_{ij}}$	Propagation frequency for monomer *j* adding to chain terminated in monomer *i*
f_{t_β}	β-Hydride elimination frequency, s^{-1}, Eq. (6)
f_{t_H}	Transfer to H_2 frequency, s^{-1}
$f_{t_{H,21}}$	Frequency of transfer to hydrogen of 2-1 terminated sites
f_{t_i}	Chain transfer frequency, s^{-1}
f_{t_M}	Transfer to monomer frequency, s^{-1}, Eq. (4)
f_{t_X}	Transfer to small molecule frequency, s^{-1}, Eq. (5)
$H_{M_{s-g}}$	Solid-gas partition coefficient for monomer, Eq. (63)
$H_{M_{s-l}}$	Solid-liquid partition coefficient for monomer, Eq. (62)
$H_{X_{s-g}}$	Solid-gas partition coefficient for chain transfer agent
ΔH_p	Overall enthalpy of polymerization
k_a	Activation rate constant, $L \cdot mol^{-1} \cdot s^{-1}$
k_e	Thermal conductivity of the polymer particle
k_d	Deactivation rate constant, s^{-1}
k_g	Thermal conductivity of the fluid, Eq. (90)
k_p	Propagation rate constant, $L \cdot mol^{-1} \cdot s^{-1}$
$k_{p_{ij}}$	Propagation rate constant for adding monomer *j* to a chain terminated in monomer *i*, $L \cdot mol^{-1} \cdot s^{-1}$
$\hat{k}_p$	Pseudo-propagation rate constant, $L \cdot mol^{-1} \cdot s^{-1}$
k_s	Convective mass transfer coefficient in the boundary layer surrounding a polymer particle, cm s^{-1}

k_{t_β}	b-Hydride elimination rate constant, s^{-1}
k_{t_M}	Transfer to monomer rate constant, $L \cdot mol^{-1} \cdot s^{-1}$
k_{t_X}	Transfer to small molecule rate constant, $L \cdot mol^{-1} \cdot s^{-1}$
K_{ag}	Agglomeration kernel constant, Eq. (89)
$K_{M_{l-g}}$	Liquid-gas partition coefficient for monomer, Eq. (64)
h	Convective heat transfer coefficient for the polymer particle
$H_{M_{s-g}}$	Solid-gas partition coefficient for monomer, Eq. (63)
$H_{M_{s-l}}$	Solid-liquid partition coefficient for monomer, Eq. (62)
$H_{X_{s-g}}$	Solid-gas partition coefficient for chain transfer agent
m_i	Mass fraction of polymer made on site type *i*
m_{r_i}	Mass fraction of polymer made on radius *r*, Eq. (80).
M	Monomer
$\bar{M}$	Average molar mass of the repeating unit
M_i	Molar mass of monomer type *i*
$[M_i]$	Concentration of monomer type *i*, $mol \cdot L^{-1}$
$[M_{p_i}]$	Concentration of monomer type *i* in the amorphous polymer phase, $mol \cdot L^{-1}$
$[M_{p_i}]_{eq}$	Concentration of monomer i in the polymer in equilibrium with the concentration of monomer i in the pores of the macroparticle, $mol \cdot L^{-1}$
$[M_i]_0$	Initial concentration of monomer type *i* in a polymer particle, $mol \cdot L^{-1}$
$[M_i]_b$	Concentration of monomer type *i* in the bulk phase of the reactor, $mol \cdot L^{-1}$
$[M]_g$	Monomer concentration in the gas phase, $mol \cdot L^{-1}$
$[M]_l$	Monomer concentration in the liquid phase, $mol \cdot L^{-1}$
$[M]_s$	Monomer concentration at the active site or in the solid phase, $mol \cdot L^{-1}$
$[M_i]_s$	Concentration of monomer type *i* at the active site, $mol \cdot L^{-1}$
$[M_T]_s$	Total concentration of monomer and comonomer at the active site, $mol \cdot L^{-1}$
M_n	Number average molecular weight
$\bar{M}_n$	Number average molecular weight for a polymer made in an MS catalyst, Eq. (15)
M_r	Molecular weight of a chain of length r
M_w	Weight average molecular weight
$\bar{M}_w$	Weight average molecular weight for a polymer made with an MS catalyst, Eq. (16)

M_z	z-Average molecular weight
n	Number of catalyst active site types
n_i	Number of particles with diameter d_i
Nu	Nusselt number, Eq. (90)
$P_{p_{ij}}$	Probability of adding monomer *j* to a chain terminated in monomer *i*, Eq. (31) to (34)
P_r	Living polymer chain with *r* monomeric units
P_{r_i}	Living polymer chain with *r* monomeric units terminated in monomer *i*
PDI	Polydispersity index
$\overline{PDI}$	Polydispersity index of a polymer made with an MS catalyst
r	Number of monomer units in a polymer molecule, chain length / radial position in a polymer particle
r_1, r_2	Reactivity ratios
R_{ag}	Agglomeration kernel function, Eq. (89)
R_c	Radius of the catalyst fragment, cm
R_L	Radius of a macroparticle, cm
R_{M_i}	Rate of polymerization for monomer type *i*, mol·L^{-1}
R_M	Overall local rate of polymerization
R_p	Rate of polymerization, mol·L^{-1}
R_{p_i}	Rate of polymerization for site type *i*, mol·L^{-1}
R_{p_T}	Total polymerization rate, MS catalyst, mol·L^{-1}
R_s	Radius of the microparticle, cm
t	Time, s
t_p	Polymerization time, s
T	Temperature
T_b	Bulk reactor temperature
u	Relative fluid-particle velocity, Eq. (90)
w_{F_1}	CCD component of the bivariate MWD-CCD of a copolymer made with an SS catalyst
W_{F_1}	CCD component of the bivariate MWD-CCD of a copolymer made with an MS catalyst
$w_{\log M_r}$	Flory most probable MWD, weight basis, log scale, Eq. (9)

$W_{\log M_r}$	Flory most probable MWD, weight basis, log scale, MS polymer, Eq. (14)
$w_{\log M_r,F_1}$	Stockmayer bivariate distribution, weight basis, log scale, Eq. (17)
$W_{\log M_r,F_1}$	Stockmayer bivariate distribution, weight basis, log scale, MS polymer, Eq. (22)
$w_{\log r}$	Flory most probable CLD, weight basis, log scale, Eq. (1)
V_p	Polymer particle volume, cm^3
V_{p_0}	Initial volume of the catalyst particle, cm^3
V_R	Volume of the reaction medium, L
x_{i_0}	Molar fraction of site type *i* in an MS catalyst when $t = 0$
$[X]_g$	Concentration of hydrogen, cocatalyst, impurities, and other small molecules in the gas phase, $L \cdot mol^{-1}$
$[X]_s$	Concentration of hydrogen, cocatalyst, impurities, and other small molecules in solid phase or around the active site, $L \cdot mol^{-1}$
Y_p	Polymer yield, g.

Greek Letters

β	Stockmeyer bivariate distribution parameter, Eq. (18)
ε	Polymer particle porosity or void fraction
η	Instantaneous effectiveness factor, Eq. (84)
η_{12}	Molar fraction of active sites terminated in 1-2 insertions
η_H	Correction factor for H_2 effect on propagation rate
K_β	k_{t_β}/k_p, $mol \cdot L^{-1}$
K_M	k_{t_M}/k_p
K_X	k_{t_X}/k_p
λ	$1/\log e = 2.3026$
μ_g	Viscosity of the fluid, Eq. (90)
μ_{i_g}	Chemical potential of species i in the gas phase
μ_{i_l}	Chemical potential of species i in the liquid phase
μ_{i_s}	Chemical potential of species i in the solid phase
π	Ratio of the frequencies for 1-2 to 2-1 and 2-1 to 1-2 insertions
ρ	Density of the polymer particle, $g \cdot cm^3$
ρ_g	Density of the fluid, Eq. (90)

ρ_{ij}	Ratio of the molar concentrations of monomer *i* to monomer *j*, Eq. (20) and (21)
ρ_p	Density of the semi-crystalline polymer, g·cm^3
τ	Ratio between the sum of the frequencies of all chain transfer reactions and the frequency of propagation, Eq. (2) and (7)
$\hat{\tau}$	Modified parameter τ, Eq. (10)
τ_{21}	Ratio of the frequencies of transfer to hydrogen and 1-2 propagation for 2-1 sites
τ_L	Thiele modulus
τ_R	Average residence time in the reactor
ϕ_i	Molar fraction of living chains terminated in monomer *i*

References

[1] J. B. P. Soares, *Macromol. React. Eng.* **2014**, *8*, 235.

[2] W. H. Ray, J. B. P. Soares, R. A. Hutchinson, *Macromol. Symp.* **2004**, *206*, 1.

[3] J. B. P. Soares, A. E. Hamielec, *Macromol. React. Eng.* **2007**, *1*, 53.

[4] J. B. P. Soares, A. E. Hamielec, *Macromol. React. Eng.* **2008**, *2*, 115.

[5] P. J. Flory, *J. Am. Chem. Soc.* **1936**, *58*, 1877.

[6] P. J. Flory, *J. Am. Chem. Soc.* **1937**, *59*, 241.

[7] J. B. P. Soares, T. F. McKenna, *Polyolefin Reaction Engineering*. Wiley-VCH, Weinheim, 2012.

[8] A. E. Hamielec, J. F. McGregor, A. Penlidis, *Makromol. Chem. Macromol. Symp.***1987**, *10*/*11*, 521.

[9] T. Xie, A. E. Hamielec, *Makromol. Chem. Theory Simul.* **1993**, *2*, 455.

[10] M. Dubé, J. B. P. Soares, A. Penlidis, *Ind. Eng. Chem. Res.* **1977**, *36*, 966.

[11] S. Mehdiabadi, O. Lhost, A. Vantomme, J. B. P. Soares, *Macromol. React. Eng.* **2021**, DOI: 10.1002/mren.202100041.

[12] S. Mehdiabadi, O. Lhost, A. Vantomme, J. B. P. Soares, *Ind. Eng. Chem. Res.* **2021**, *60*, 9739.

[13] V. V. Vickroy, H. Schneider, R. F. Abbott, *J. Appl. Polym. Sci.* **1993**, *50*, 551.

[14] J.B.P. Soares, A.E. Hamielec, *Polymer* **1995**, *36*, 2257.

[15] J. B. P. Soares, R. F. Abbott, J. N. Willis, X. Liu, *Macromol. Chem. Phys.* **1996**, *197*, 3383.

[16] J. B. P. Soares, *Polym. React. Eng.* **1998**, *6*, 225.

[17] W. H. Stockmayer, *J. Chem. Phys.* **1945**, *13*, 199.

[18] J. B. P. Soares, A. E. Hamielec, *Macromol. Theory Simul.* **1995**, *4*, 305.

[19] J.B.P. Soares, A. Penlidis, in *Preparation, Properties and Technology of Metallocene-Based Polyolefins*, J. Scheirs and W. Kamisnky (editors), John Wiley and Sons, Chichester, **2000**, 237.

[20] J. B. P. Soares, D. Beigzadeh, T. A. Duever, A. A. da Silva Filho, *Polym. React. Eng.* **2000**, *8*, 241.

[21] A. A. da Silva Filho, G. B. de Galland, J. B. P. Soares, *Macromol. Chem. Phys.* **2000**, *201*, 1226.

[22] J.B.P. Soares, *Chem. Eng. Sci.* **2001**, *56*, 4131.

[23] K. Chen, S. Mehdiabadi, B. Liu, J. B. P. Soares, *Macromol. React. Eng.* **2016**, *10*, 206.

[24] A. A. Alghyamah, J. B. P. Soares, *Macromol. Symp.* **2009**, *285*, 81.

[25] A. A. Alghyamah, J. B. P. Soares, *Macromol. Rapid Commun.* **2009**, *30*, 384.

[26] C. Hornchaiya, S. Anatawaraskul, J. B. P. Soares, S. Mehdiabadi, *Macromol. Phys. Chem.* **2019**, 1800522.

[27] M. A. Al-Saleh, J. B. P. Soares, T. A. Duever, *Macromol. React. Eng.* **2010**, *4*, 578.

[28] M. A. Al-Saleh, J. B. P. Soares, T. A. Duever, *Macromol. React. Eng.* **2011**, *5*, 587.

[29] M. A. Al-Saleh, J. B. P. Soares, T. A. Duever, *Macromol. React. Eng.* **2012**, *6*, 189.

[30] S. Anantawaraskul, J. B. P. Soares, P. Wood-Adams, *Macromol. Theory Simul.* **2003**, *12*, 229.

[31] A. Alshaiban, J. B. P. Soares, *Macromol. React. Eng.* **2014**, *8*, 723.

[32] A. Albeladi, J. B. P. Soares, S. Mehdiabadi, *Macromol. Chem. Eng.* **2018**, *13*, 1800059.

[33] J. B. P. Soares, A. E. Hamielec, *Macromol. Theory Simul.* **1996**, *5*, 547.

[34] J. B. P. Soares, A. E. Hamielec, *Macromol. Theory. Simul.* **1997**, *6*, 591.

[35] J. B. P. Soares, *Macromol. Mater. Eng.* **2004**, *289*, 70.

[36] L. C. Simon, J. B. P. Soares, *Macromol. Theory Simul.* **2002**, *11*, 222.

[37] J. B. P. Soares, *Macromol. Theory Simul.* **2002**, *11*, 184.

[38] M. Nele, J. B. P. Soares, J. C. Pinto, *Macromol. Theory Simul.* **2003**, *12*, 582.

[39] D. J. Read, J. B. P. Soares, *Macromolecules* **2003**, *36*, 10037.

[40] L. C. Simon, J. B. P. Soares, *Ind. Eng. Chem. Res.* **2005**, *44*, 2461.

[41] T. F. McKenna, J. B. P. Soares, L. C. Simon, *Macromol. Mater. Eng.* **2005**, *290*, 507.

[42] T. F. McKenna, J. B. P. Soares, *Chem. Eng. Sci.* **2001**, *56*, 3931.

[43] J. B. P. Soares, T. F. McKenna, C. P. Cheng, in *Polymer Reaction Engineering*, J.M. Asua (editor), Blackwell Publishing, Oxford, UK, 2007, 29-117.

[44] A. L. T. Brandão, J. B. P. Soares, J. C. Pinto, A. L. Alberton, *Macromol. React. Eng.* **2015**, *9*, 141.

[45] S. Saadat, J. B. P. Soares, P. J. DesLauriers, J. S. Fodor, *Macromol. React. Eng.* **2019**, 1900032.

[46] A. Caldera, J. B. P. Soares, P. J. DesLauriers, J. S. Fodor, J. Catal. **2019**, *375*, 140.

[47] S. Mehdiabadi, J. B. P. Soares, J. Brinen, *Macromol. React. Eng.* **2017**, *11*, 1600044.

[48] K. Chen, S. Mehdiabadi, B. Liu, J. B. P. Soares, *Macromol. React. Eng.* **2016**, *10*, 551-556.

[49] S. Mehdiabadi, J. B. P. Soares, *Macromolecules* **2016**, *49*, 2448.

[50] A. Alshaiban, J. B. P. Soares, *Macromol. React. Eng.* **2014**, *8*, 723.

[51] S. Mehdiabadi, J. B. P. Soares, *Macromol. Chem. Phys.* **2013**, *214*, 246.

[52] S. Mehdiabadi, J. B. P Soares, J. Brinen, D. Bilbao, *Macromolecules* **2013**, *46*, 1312.

[53] S. Mehdiabadi, J. B. P. Soares, *Macromolecules* **2012**, *45*, 1777.

[54] A. Alshaiban, J. B. P. Soares, *Macromol. React. Eng.* **2012**, *6-7*, 265.

[55] V. Touloupidis, A. Albretch, J. B. P. Soares, *Macromol. React. Eng.* **2018**, *12*, 1700056.

[56] Y. V. Kissin, L. A. Rishina, *J. Polym. Sci., Part A: Polym. Chem.* **2002**, *40*, 1353.

[57] Y. V. Kissin, L. A. Rishina, E. I. Vizen, *J. Polym. Sci., Part A: Polym. Chem.* **2002**, *40*, 1899.

[58] Y. V. Kissin, R. I. Mink, T. E. Nowlin, A. J. Brandolini, *Top. Catal.* **2002**, *7*, 69.

[59] Y. V. Kissin, *J. Mol. Catal.* **1989**, *56*, 220.

[60] T. Garoff, S. Johansson, K. Pesonen, P. Waldvogel, D. Lindgren, *Eur. Polym. J.* **2002**, *38*, 121.

[61] V. Busico, R. Cipullo, A. Mizuno, *Makromol. Chem. Rapid Commun.* **1992**, *13*, 15.

[62] T. Tsutsui, N. Kashiwa, A. Mizuno, *Makromol. Chem. Rapid Commun.* **1990**, *11*, 565.

[63] J. C. Chadwick, A. Miedema, O. Sudmeijer, *Macromol. Chem. Phys.* **1994**, *195*, 167.

[64] J. B. P. Soares, A. E. Hamielec, *Polymer* **1996**, *37*, 4607.

[65] J. B. P. Soares, A. E. Hamielec, *Polymer* **1996**, *37*, 4599.

[66] D. M. Sarzotti, D. J. Marshman, W. E. Ripmeester, J. B. P. Soares, *J. Polym. Sci.: Part A: Polym. Chem.* **2007**, *45*, 1677.

[67] F. C. Franceschini, T. T. R. Tavares, P. P. Greco, G. B. Galland, J. H. Z. dos Santos, J. B. P. Soares, *J. Appl. Polym. Sci.* **2005**, *95*, 1050.

[68] D. Beigzadeh, J. B. P. Soares, T. A. Duever, *J. Polym. Sci.: Part A: Polym. Chem.* **2004**, *42*, 3055.

[69] S. Mehdiabadi, J. B. P. Soares, J. Brinen, *Macromolecules* **2018**, *51*, 7061.

[70] A. Alshaiban, J. B. P. Soares, *Macromol. Symp.* **2012**, *312*, 72.

[71] A. Alshaiban, J. B. P. Soares, *Macromol. React. Eng.* **2012**, *6*, 265.

[72] A. Alshaiban, J. B. P. Soares, *Macromol. React. Eng.* **2011**, *5*, 96.

[73] A. Alizadeh, V. Touloupidis, J. B. P. Soares, *Macromol. Chem. Eng.* **2021**, 2100006.

[74] I. C. Sanchez, R. H. Lacombe, *J. Phys. Chem.* **1976**, *80*, 2352.

[75] I. C. Sanchez, R. H. Lacombe, *Macromolecules* **1978**, *11*, 1145.

[76] P. A. Mueller, J. R. Richards, J. P. Congalidis, *Macromol. React. Eng.* **2011**, *5*, 261.

[77] N. B. Ishola, F. N. Andrade, F. Machado, F. L. McKenna, *Macromol. React. Eng.* **2020**, *14*, 2000021.

[78] L. M. Robeson, T. G. Smith, *J. Appl. Polym. Sci.* **1968**, *12*, 2083.

[79] N. N. Li, R. B. Long, *AlChE J.* **1969**, *15*, 73.

[80] J.-S. Yoon, C.-Y. Chung, I.-H. Lee, *Eur. Polym. J.* **1994**, *30*, 1209.

[81] S. K. Nath, B. J. Banaszak, J. J. de Pablo, *Macromolecules* **2001**, *34*, 7841.

[82] W. Yao, X. Hu, Y. Yang, *J. Appl. Polym. Sci.* **2007**, *103*, 1737.

[83] W. Yao, X. Hu, Y. Yang, *J. Appl. Polym. Sci.* **2007**, *104*, 3654.

[84] A. Novak, M. Bobak, J. Kosek, B. J. Banaszak, D. Lo, T. Widya, W. Harmon Ray, J. J. de Pablo, *J. Appl. Polym. Sci.* **2006**, *100*, 1124.

[85] B. J. Banaszak, D. Lo, T. Widya, W. H. Ray, J. J. de Pablo, A. Novak, J. Kosek, *Macromolecules* **2004**, 37, *9139*.

[86] P. Paricaud, A. Galindo, G. Jackson, *Ind. Eng. Chem. Res.* **2004**, *43*, 6871.

[87] A. J. Haslam, N. von Solms, C. S. Adjiman, A. Galindo, G. Jackson, P. Paricaud, M. L. Michelsen, G. M. Kontogeorgis, *Fluid Phase Equilib.* **2006**, *243*, 74.

[88] M. A. Bashir, M. Al-haj Ali, V. Kanellopoulos, J. Seppälä, *Fluid Phase Equilib.* **2013**, *358*, 83.

[89] M. A. Bashir, V. Monteil, V. Kanellopoulos, M. A.-H. Ali, T. McKenna, *Macromol. Chem. Phys.* **2015**, *216*, 2129.

[90] M. A. Bashir, M. A.-h. Ali, V. Kanellopoulos, J. Seppälä, *Fluid Phase Equilib.* **2015**, *388*, 107.

[91] J. Sun, H. Wang, M. Chen, J. Ye, B. Jiang, J. Wang, Y. Yang, C. Ren, *J. Appl. Polym. Sci.* **2017**, *134*.

[92] A. J. Cancelas, M. A. Plata, M. A. Bashir, M. Bartke, V. Monteil, T. F. L. McKenna, *Macromol. Chem. Phys.* **2018**, *219*, 1700565.

[93] J. A. Moebus, B. R. Greenhalgh, *Macromol. React. Eng.* **2018**, *12*, 1700072.

[94] Y. Zhou, A. Alizadeh, B. Liu, J. B. P. Soares, *Macromol. React. Eng.* **2020**, 200043.

[95] J. B. P. Soares, A. E. Hamielec, *Polym. React. Eng.* **1995**, *3*, 261.

[96] B. Liu, B. Liu, J. B. P. Soares, *Macromol. React. Eng.* **2018**, 1800054.

[97] B. Liu, J. Romero, B. Liu, J. B. P. Soares, *Macromol. React. Eng.* **2018**, 1800051.

[98] J. Romero, J. B. P. Soares, *Macromol. React. Eng.* **2018**, *12*, 1800002.

[99] J. Romero, J. B. P. Soares, *Macromol. React. Eng.* **2018**, *12*, 1700031.

[100] R. Hutchinson, C. Chen, W. Ray, *J. Appl. Polym. Sci.* **1992**, *44*, 1389.

[101] J. A. Debling, W. H. Ray, *Ind. Eng. Chem. Res.* **1995**, *34*, 3466.

[102] E. Hoel, C. Cozewith, G. Byrne, *AIChE J.* **1994**, *40*, 1669.

[103] R. Galvan, M. Tirrell, *Chem. Eng. Sci.* **1986**, *41*, 2385.

[104] N. Wakao, J. Smith, *Ind. Eng. Chem. Fund.* **1964**, *3*, 123.

[105] V. Kanellopoulos, G. Dompazis, B. Gustafsson, C. Kiparissides, *Ind. Eng. Chem. Res.* **2004**, *43*, 5166.

[106] V. Kanellopoulos, B. Gustafsson, C. Kiparissides, *Macromol. React. Eng.* **2008**, *2*, 240.

[107] A. Alizadeh, F. Sharif, M. Ebrahimi, T. F. L. McKenna, *Ind. Eng. Chem. Res.* **2018**, *57*, 6097.

[108] M. A. Bashir, V. Monteil, C. Boisson, T. F. L. McKenna, *AIChE J.* **2017**, *63*, 4476.

[109] T. F. L. McKenna, M. A. Bashir, in *Multimodal Polymers with Supported Catalysts - Design and Production*, Springer Verlag, 2018 (DOI 978-3-030-03476-4).

[110] T. F. L. McKenna, A. Di Martino, G. Weickert, J. B. P. Soares, *Macromol. Reac. Eng.* **2010** *4*, 40.

[111] A. Alizadeh, T. F. L. McKenna, *Macromol. React. Eng.* **2018**, *12*, 1700027.

[112] P. Kittilsen, H. Svendsen, T. F. McKenna, *AIChE J.* **2003**, *49*, 1495.

[113] P. Kittilsen, T. F. McKenna, H. Svendsen, H. A. Jakobsen, S. Fredrisken, *Chem. Eng. Sci.* **2001**, *56*, 302.

[114] Z. Grof, J. Kosek, M. Marek, *Ind. Eng. Chem. Res.* **2005**, *44*, 2389.

[115] Z. Grof, J. Kosek, M. Marek, *AIChE J.* **2005**, *51*, 2048.

[116] A. Di Martino, G. Weickert, F. Sidoroff, T. F. L. McKenna, *Macromol. React. Eng.* **2007**, *1*, 338.

[117] J. B. P. Soares, A. E. Hamielec, *Polym. React. Eng.* **1996**, *4*, 153.

[118] K. D. Hungenberg, M. Wulkov, *Modeling and Simulation in Polymer Reaction Engineering,* Wiley-VCH, Weinheim, Germany, 2018.

[119] T. F. McKenna, D. Cokljat, R. Spitz, *AIChE J* **1999**, *45*, 2392.

[120] T. F. McKenna, D. Cokljat, R. Spitz, D. Schweich, *Catalysis Today* **1999**, *48*, 101.

[121] C. Martin, T. F. McKenna, *Chem. Eng. J.* **2002**, *87*, 89.

[122] G. Dompazis, V. Kanellopoulos, and C. Kiparissides, *Ind. Eng. Chem. Res.* **2006**, *45*, 3800.

[123] G. Hendrickson, *Chem. Eng. Sci.* **2006**, *61*, 1041

[124] H. Hatzantonis, A. Goulas, C. Kiparissides, *Chem. Eng. Sci.* **1998**, *53*, 3251.

[125] R. F. Alves, T. Casalini, G. Storti, T. F. L. McKenna, *Macromol. Reac. Eng.* **2021**, *15*, 2000059.

[126] J. R. Llinas, J. L. Selo, Method for reducing sheeting and agglomerates during olefine polymerization, US Patent 7,812,103 (2010), INEOS Europe Ltd Ranz.

[127] W. E. Ranz, W. R. Marshall, *Chem. Eng. Prog.* **1952**, *48*, 141.

[128] E. Eriksson, T. F. McKenna, *Ind. Eng. Chem. Res.* **2004**, *43*, 7251.

[129] E. J. G. Eriksson, G. Weickert, T. F. L. McKenna, *Macromol. Reac. Eng.* **2010**, *4*, 95.

[130] E. J. G. Eriksson, *Investigation of heat transfer and kinetic mechanisms in olefin polymerisation*, Ph.D. Thesis, University Claude Bernard Lyon 1, no. 41-2005 (2005).

[131] R. Alves, M. A. Bashir, T. F. L. McKenna, *Ind. Eng. Chem. Res.* **2017**, *56*, 13582.

[132] R. F. Alves, T. F. L. McKenna, *Chem Eng J.* **2020**, *383*, 123114

[133] A. Gobin, H. Neau, O. Simonin, J. R. Llinas, V. Reiling, J. L. Sélo, *Int. J. Num. Meth.* **2003**, *43*, 1199.

[134] P. Fede, O. Simonin, A. Ingram, *Chem. Eng. Sci.* **2016**, *142*, 215.

[135] A. Ozel, A. Sarthou, Z. Zeren, P. Fede, O. Simonin, I. Ghouila, J. L. Chamayou, *Numerical Simulation of Liquid Injection into a Dense Fluidized Bed*, Proceedings of the 8th International Conference on Multiphase Flow, ICMF 2013, Jeju (Korea), paper n° 991, 2013.

[136] Z. Zeren, A. Ozel, A. Sarthou, P. Fede, H. Neau, O. Simonin, J. L. Chamayou, I. Ghouila, , *3D Numerical Simulation of Catalyst Injection*, Proceeding of the 8th International Conference on Multiphase Flow, ICMF 2013, Jeju (Korea), paper n° 331, 2013.

[137] H. Neau, M. Pigou, P. Fede, R. Ansart, C. Baudry, N. Mérigoux, J. Laviéville, Y. Fournier, N. Renon, O. Simonin, *Powder. Tech.* **2020**, *366*, 906.

[138] V. Verma, N. G. Deen, J. T. Padding, J.A.M. Kuipers, *Chem. Eng. Sci.* **2013**, *102*, 227.

[139] V. Verma, N. G. Deen, J. T. Padding, J. A. M. Kuipers, *Ind. Eng. Chem. Res.* **2014**, *53*, 17487.

[140] V. Verma, N. G. Deen, J. T. Padding, J. A. M. Kuipers, *AIChE J.* **2015**, *61*, 1492.

[141] M. Banaei, J. Jegers, M. van Sint Annaland, J. A. M. Kuipers, N. G. Deen, *Ind. Eng. Chem. Res.* **2017**, *56*, 8729.

[142] M. Van Sint Annaland, G. A. Bokkers, M. J. V. Goldschmidt, O. O. Olaofe, M. A. van der Hoef, J. A. M. Kuipers, *Chem. Eng. Sci.* **2009**, *64*, 4222.

[143] M. Van Sint Annaland, G. A. Bokkers, M. J. V. Goldschmidt, O. O. Olaofe, M. A. van der Hoef, J. A. M. Kuipers, *Chem. Eng. Sci.* **2009**, *64*, 4237.

[144] O. O. Olaofe, A. V. Patil, N. G. Deen, M. A. van der Hoef, J. A. M. Kuipers, *Chem. Eng. Sci.* **2014**, *108*, 258.

[145] J. B. P. Soares, V. Touloupidis, in *Multimodal Polymers with Supported Catalysts: Design and Production*, A. R. Albunia, F. Prades, D. Jeremic (editors), Springer, Cham, Switzerland, 2019, 115.

[146] J. B. P. Soares, A. E. Hamielec, *Macromol. Theory Simul.* **1995**, *4*, 1085.

[147] J. J. Zacca, J. A. Debling, W. H. Ray, *Chem. Eng. Sci.* **1996**, *21*, 4859.

[148] J. A. Debling, J. J. Zacca, W. H. Ray, *Chem. Eng. Sci.* **1997**, *52*, 1969.

[149] J. J. Zacca, J. A. Debling, W. H. Ray, *Chem. Eng. Sci.* **1997**, *52*, 1941.

[150] D. Y. Khang, H. H. Lee, *Chem. Eng. Sci.* **1997**, *52*, 421.

[151] H. Hatzantonis, A. Goulas, C. Kiparissides, *Chem. Eng. Sci.* **1998**, *53*, 3251.

[152] H. Hatzantonis, C. Kiparissides, *Comp. Chem. Eng.* **1998**, *22*, S127.

[153] A. Prasetya, L. Liu, J. Lister, F. Watanabe, K. Mitsutani, G. H. Ko, *Chem. Eng. Sci.* **1999**, *54*, 3263.

[154] M. Covezzi, G. Mei, *Chem. Eng. Sci.* **2001**, *56*, 4059.

[155] K. Zoellner, K.-H. Reichert, *Chem. Eng. Sci.* **2001**, *56*, 4099.

[156] H. Yiannoulakis, A. Yiagopoulos, C. Kiparissides, *Chem. Eng. Sci.* **2001**, *56*, 917.
[157] A. Yiagopoulos, H. Yiannoulakis, V. Dimos, C. Kiparissidis, *Chem. Eng. Sci.* **2001**, *56*, 3979.
[158] J. J. Zacca, J.A. Debling, *Chem. Eng. Sci.* **2001**, *56*, 4029.
[159] A. G. Mattos Neto, J. C. Pinto, *Chem. Eng. Sci*. **2001**, *56*, 4043.
[160] J. Y. Kim, K. Y. Choi, *Chem. Eng. Sci.* **2001**, *56*, 4069.
[161] Y. M. Harshe, R. P. Utikar, V. V. Ranade, *Chem. Eng. Sci.* **2001**, *56*, 5145.
[162] C. J. Dittrich, S. M. P. Mutsers, *Chem. Eng. Sci.* **2007**, *62*, 5777.
[163] Z. H. Luo, P. L. Su, X. Z. You, D. P. Shi, J. C. Wu, *Chem. Eng. J.* **2009**, *146*, 466.

- A new way to categorize mathematical models for olefin polymerization reactors
- Seven interconnected modeling levels: catalysis, polymerization kinetics, thermodynamic equilibrium, particle transport phenomena, particle interactions, reactor fluid dynamics, and reactor residence time distribution.
- Integrated overview of the modeling process, from the active site scale to macroscopic reactor phenomena.